CFD analysis of thermal dispersion in a structured pebble bed

HJ Vermaak

orcid.org/0000-0002-3988-0004

Dissertation accepted in fulfilment of the requirements for the degree *Master of Engineering in Nuclear Engineering* at the North-West University

Supervisor: Prof CG du Toit

Graduation ceremony: July 2019

Student number: 22753109

ABSTRACT

Heat transfer mechanisms in packed beds are not entirely understood, which gave rise to thermal dispersion correlations that contain considerable amounts of empiricism. The empiricism resulted from incorporating a limited number of heat transfer mechanisms, along with characterising porous structures with insufficient complexity. Therefore, these correlations have limited applicability and occasionally, uncertain validity. The High Pressure Test Unit (HPTU) was subsequently constructed to conduct a comprehensive set of separate effects tests for the purpose of validating existing thermohydraulic correlations. These tests included the Braiding Effects Test Section (BETS) experiments which investigated the increased thermal dispersion in packed beds that results from the effects of the porous structure on the flow. The BETS experimental temperature data required validation. Computational fluid dynamics (CFD) has been proven to accurately predict the thermal hydraulic phenomena associated with fluid flow in packed beds and can consequently also be used to analyse thermal dispersion in a packed bed (Cheng *et al.*, 1999; Wen and Ding, 2006; Hassan, 2008; Rousseau and Van Staden, 2008; Van Antwerpen, 2009; Kgame, 2010; Preller, 2011; Van der Merwe, 2014).

This study subsequently presents an explicit numerical analysis of thermal dispersion in a structured pebble bed using the CFD package STAR-CCM+®. This work is an extension of the preliminary work conducted by Preller (2011) wherein a single case of the BETS experiments was simulated, which corresponded to a Reynolds number of 3000. Furthermore, symmetry boundary conditions were imposed on the walls to reduce the cross-sectional area to 25% of its original size since this particular BETS packing configuration consisted of 3898 mono-sized spheres. The initial simulation was subsequently verified. Nevertheless, in addition to instabilities, it was observed that the symmetry planes affect the simulated temperature profiles to a certain degree. The full cross-sectional area was consequently simulated, which is also preferred in the analysis of radial thermal dispersion. The resulting meshes consisted of nearly 40 million volumetric cells, followed by several simulation challenges along with highly oscillatory flows and large temperature gradients.

A suitable and universal simulation methodology was therefore developed based on a Reynolds number of 3000 by conducting comprehensive sets of analyses on, among others, mesh quality, mesh independency, turbulence models, temperature extraction methods, wall treatment, along with stability and convergence criteria. It was determined that the use of large eddy simulation (LES) along with mesh refinement in the packed region of the bed remained the most suitable

approach. The resulting simulation methodology has been verified to accurately predict the radial temperature profile in a packed bed and displayed a considerable improvement over initial approaches in the agreement with experimental temperature data. The methodology was subsequently used to validate an extended range of BETS experiments with Reynolds numbers of up to 40000. In all cases, good agreement between the numerically simulated and experimentally measured temperatures has been achieved, which simultaneously verified the methodology for the entire set of Reynolds numbers and validated the temperature data from the selected BETS experiments. It can therefore be concluded that CFD can be used to provide an accurate analysis of thermal dispersion in a structured pebble bed.

Keywords: Computational fluid dynamics (CFD); Large eddy simulation (LES); Packed bed; STAR-CCM+®; Thermal dispersion.

ACKNOWLEDGEMENTS

I express my sincere gratitude towards God in the Name of the Lord Jesus Christ for His abundant grace throughout my life, for the knowledge, wisdom and perseverance to conduct this study, for without Him this would not have been possible. *Soli Deo Gloria*.

I would like to genuinely thank my supervisor, Prof. Jat du Toit, for his detailed guidance, patience and substantial support throughout this study, as well as the opportunity to be part of the SARChI Research Chair in Nuclear Engineering. It has truly been a privilege. In the same breath, I would like to thank Me. Francina Jacobs and all my friends from the chair for their noteworthy encouragement and support throughout this study.

I am also grateful for the CFD support from Mr. Louis le Grange, as well as Mr. Christiaan de Wet and Mr. Wian van der Merwe from Aerotherm. In addition, I would like to thank Mr. Martin Dreyer for his support on matters regarding the HPC.

I would like to further express my gratitude towards two exceptional men, namely Mr. Harm Stavast and Pr. Mike Fluech, for all their support,

Lastly, I would like to express my heartfelt appreciation towards my family and all my friends. I am forever grateful for my parents, my brother, my sister and their families for who they are and everything that they have done.

NATIONAL RESEARCH FOUNDATION DISCLAIMER

This work is based on the research supported by the South African Research Chairs Initiative of the Department of Science and Technology and National Research Foundation of South Africa (Grant number 61059). Any opinion, finding and conclusion or recommendation expressed in this material is that of the author and the NRF does not accept any liability in this regard.

TABLE OF CONTENTS

LIST OF TABLES

LIST OF FIGURES

NOMENCLATURE

Abbreviation or Acronym	Meaning
BCC	Body-centred cubic
BETS	Braiding Effects Test Section
CAD	Computer aided design
CCP	Cubic close-packing
CFD	Computational fluid dynamics
CFL	Courant-Friedrichs-Lewy
CHT	Computational Heat Transfer
DDES	Delayed detached eddy simulation
DEM	Discrete element modelling
DES	Detached eddy simulation
DNS	Direct numerical simulation
EOS	Equation of state
FCC	Face-centred cubic
HPC	High performance computer
HPTU	High Pressure Test Unit
HTGR	High-temperature gas-cooled reactor
HTR	High temperature reactor
HTTF	Heat transfer test facility
HTTU	High Temperature Test Unit
ICAPP	International Congress on Advances in Nuclear Power Plants
IDDES	Improved delayed detached eddy simulation
LES	Large eddy simulation
Ltd.	Limited
MFA	Mass flow-averaged
MSE	Mean squared error
mSRK	Modified Soave-Redlich-Kwong
NRF	National Research Foundation
PBMR	Pebble bed modular reactor
PLM	Product Lifecycle Management
PR	Peng-Robinson
Pty.	Proprietary company
q-DNS	Quasi-Direct Numerical Simulation
RANS	Reynolds-averaged Navier-Stokes
RSM	Reynolds stress model

SARChI	South African Research Chairs Initiative
SC	Simple cubic
SGS	Subgrid scale
SOC	State owned company
SRK	Soave-Redlich-Kwong
SST	Shear-stress-transport
TRISO	Tristructural-isotropic
uRANS	Unsteady Reynolds-averaged Navier-Stokes
URF	Under-relaxation factor
VDI	Verein Deutscher Ingenieure
WALE	Wall-adapting local eddy-viscosity
WMLES	Wall-modelled large eddy simulation

Latin symbols	**Description**	**SI unit**
$A_{braiding\ gas}$	Inner cross-sectional area of the braiding gas inlet pipe	m
$A_{cold\ gas}$	Total cross-sectional inlet flow area of the cold gas	m
B	Base cell size	m
C	Courant number	-
C_{ij}	Cross-stresses	Pa
C_s	Smagorinsky constant	-
d	Particle diameter (Figure 3-5, Figure 3-16)	m
d_p	Pebble diameter	m
D	Internal pipe or cylinder diameter	m
$D1$	BETS packing height	m
$D2$	BETS packing width	m
$D3$	BETS packing length	m
$D_{braiding}$	Inner diameter of braiding gas inlet pipe	m
$D_{outer\ braiding}$	Outer diameter of braiding gas inlet pipe	m
E	Total specific energy	J/kg
f	Mass flow ratio of the cold gas to the total gas flow	-
$G(x_i, x_i', \Delta)$	LES filter function	
h	Heat transfer coefficient	W/m^2·K
k	Turbulent kinetic energy	J/kg
k_e	Effective thermal conductivity	W/m·K
k_f	Thermal conductivity of the fluid	W/m·K
K	Constant related to the aspect ratio (α) (Equation 3.5)	-

L	Packed bed length	m
L_{ij}	Leonard stresses	Pa
$\dot{m}_{braiding\ gas}$	Braiding gas mass flow rate	kg/s
$\dot{m}_{cold\ gas}$	Total cold gas mass flow rate	kg/s
$\dot{m}_{total}$	Total mass flow rate	kg/s
n	Flow behaviour index	-
N	Coordination or kissing number	-
Nu	Nusselt number	-
P	Static pressure	Pa
Pe	Péclet number	-
Pr	Prandtl number	-
Q	Heat flux (Figure 3-3)	W
r	Radial coordinate (Figure 3-5)	m
R	Tube radius (Figure 3-5)	m
Re	Reynolds number	-
$Re_{braiding\ gas}$	Braiding gas inlet Reynolds number	-
$Re_{cold\ gas}$	Cold gas inlet Reynolds number	-
Re_m	Modified Reynolds number	-
Re_p	Particle Reynolds number	-
Re_{total}	Total mass flow-averaged or superficial Reynolds number	-
R_{ij}	LES Reynolds stresses	Pa
S_E	Energy source	W/m^3
t	Time	s
T	Reynolds averaging time interval	s
$\bar{T}_i$	Mass flow-averaged inlet temperature	K
T_0	Initialisation temperature	K
u	Fluid velocity	m/s
u	Fluid velocity in the x-direction (Figure 2-1)	m/s
u_∞	Freestream or bulk velocity	m/s
u^+	Dimensionless velocity	-
u_0	Superficial fluid velocity	m/s
$\bar{u}_x$	Time-averaged streamwise velocity	m/s
u_τ	Friction velocity	m/s
v	Fluid velocity in the y-direction (Figure 2-1)	m/s
v_0	Superficial inlet velocity (Figure 3-5)	m/s
V_s	Volume occupied by solid particles	m^3
V_t	Total internal packed bed volume	m^3

V_v	Total voidage volume	m^3
w_z	Axial velocity (Figure 3-5)	m/s
x	Cartesian coordinate in x-direction	m
x	Characteristic length (Figure 2-1)	m
x_c	Critical length (Figure 2-1)	m
y	Cartesian coordinate in y-direction	m
y	Normal wall distance (Equation 2.18)	m
y^+	Dimensionless wall distance	-
z	Cartesian coordinate in z-direction	m
z	Normalised wall distance (Figure 3-5)	-
Z	Compressibility factor	-

Greek symbols	**Description**	**SI unit**
α	Aspect ratio	-
γ	Heat transfer efficiency	m/s·K
$\dot{\gamma}$	Rate of shear strain or deformation	s^{-1}
Γ	Diffusivity of $\phi(x_i, t)$	
Γ_t	Turbulent eddy diffusivity	Pa·s
δ	Boundary layer thickness	m
Δ	LES filter cut-off width	m
ΔP	Pressure drop over packed bed	Pa
Δt	Time step size	s
Δx	Cell size (Equation 4.1)	m
Δ_x	Volume cell width	m
Δ_y	Volume cell length	m
Δ_z	Volume cell height	m
ε	Turbulent dissipation rate	J/kg·s
ε	Porosity (Figure 3-5)	-
$\overline{\varepsilon}$	Average porosity	-
ε_b	Bulk porosity	-
η	Kolmogorov length scale	m
θ	Cell skewness angle	°
κ	Consistency index	$N \cdot s^n/m^2$
λ	Second or bulk viscosity	Pa·s
μ	Dynamic viscosity	Pa·s
$\mu_{braiding\ gas}$	Dynamic viscosity of the braiding gas	Pa·s

$\mu_{cold\ gas}$	Dynamic viscosity of the cold gas	Pa·s
μ_t	Turbulent eddy viscosity	Pa·s
ν	Kinematic viscosity	m^2/s
ρ	Fluid density	kg/m^3
σ	Total normal stress	Pa
σ_t	Turbulent Prandtl or Schmidt number	-
τ	Shear or tangential stress	Pa
τ_{ij}^s	Subgrid scale Reynolds stresses	Pa
τ_w	Wall or surface shear stress	$N{\cdot}s/m^2$
τ_y	Yield stress	Pa
φ	Angle related to ϕ_c (Figure 3-3)	°
ϕ_c	Contact angle (Figure 3-3)	°
$\phi(x_i, t)$	Any scalar that is a function of space and time	
$\bar{\phi}(x_i)$	Time average of $\phi(x_i, t)$ (Equation 2.19)	
$\phi'(x_i, t)$	Fluctuation around $\bar{\phi}(x_i)$ (Equation 2.19)	
$\bar{\phi}(x_i, t)$	Spatially filtered $\phi(x_i, t)$ (Equation 2.26)	
$\phi'(x_i, t)$	Sub-filtered or subgrid $\phi(x_i, t)$ (Equation 2.26)	
ψ	Friction factor	-
ω	Specific dissipation rate	s^{-1}

Vector or tensor	Description	SI unit
$\boldsymbol{a}$	Face area or face normal vector	m
$\boldsymbol{b}$	Vector sum of all body forces	N/kg
$\boldsymbol{ds}$	Centroid connecting vector	m
$\boldsymbol{I}$	Unit tensor	-
$\boldsymbol{q''}$	Heat flux vector	W/m^2
$\boldsymbol{u}$	Velocity vector	m/s
$\boldsymbol{u_0}$	Initialisation velocity vector	m/s
$\boldsymbol{\tau}$	Cauchy stress tensor	Pa

General subscripts	Description
i, j	Indices corresponding to Cartesian components or coordinates
$ii\ or\ ij$	Tensor index notation (Section 2.2.2)
$x, y\ or\ z$	Cartesian components in corresponding directions

Mathematical operators	Description
$\boldsymbol{\nabla}$	Del operator
$\bullet$	Dot or scalar product
δ_{ij}	Kronecker delta
$[\,]^T$	Transpose operator

CHAPTER 1: INTRODUCTION

1.1 Background

Packed beds are utilised in many industrial processes such as thermal energy storage, separation units and heterogeneous catalytic reactors (Wen and Ding, 2006; Caulkin *et al*., 2007; Incropera *et al*., 2013). The thermal-hydraulic behaviour of packed beds has been an important research topic for years (Achenbach, 1995; Rousseau and Van Staden, 2008). Increasing energy demands with associated inherent safety requirements resulted in the development of the pebble bed modular reactor (PBMR) (Hassan, 2008; Van Antwerpen, 2009; Latifi *et al*., 2016).

The PBMR concept forms part of Generation IV nuclear technology and is based on high-temperature gas-cooled reactor (HTGR) concepts. The PBMR has an annular core with an inner and outer diameter of 2.0 and 3.7 m, respectively. The outer layer or reflector is fabricated from graphite. In addition, the core has an effective height of 11 m and contains over 450000 fuel spheres. The 60 mm fuel spheres contain numerous tristructural-isotropic (TRISO) coated particles, which are surrounded by a graphite matrix. The TRISO coatings surround the fissile fuel kernels. The coatings, as well as the graphite allows the reactor to reach very high burnup values, while retaining volatile fission products. The PBMR concept is considered inherently safe owing to the low core power density and the large amount of graphite present within the core (Hassan, 2008; Van Antwerpen, 2009; Latifi *et al*., 2016).

The PBMR development required more comprehensive thermal-fluid data on packed beds than that which was available in open literature. Consequently, PMBR SOC (Ltd.) appointed M-Tech Industrial (Pty.) Ltd. in association with North-West University, South Africa, to develop the Heat Transfer Test Facility (HTTF). The HTTF consisted of two units, the High Temperature Test Unit (HTTU) and the High Pressure Test Unit (HPTU). The HTTU and HPTU were associated with thorough sets of integrated and separate effects tests, respectively (Rousseau and Van Staden, 2008; Du Toit *et al*., 2012a).

This study presents an explicit computational fluid dynamics (CFD) investigation on the Braiding Effect Test Section (BETS) separate effects tests, which were performed in the HPTU. The braiding effect ascribes to the enhanced thermal dispersion or thermal diffusion that results from the influence of the porous structure on the flow through packed beds. Consequently, the purpose

of the BETS experiments was to evaluate the braiding effect within packed beds (Kgame, 2010; Preller, 2011; Du Toit *et al*., 2012b; Du Toit *et al*., 2014). The BETS geometries represented rectangular, structured, A-B-C body-centred cubic (BCC) packings. This was accomplished by attaching uniform acrylic spheres to strings, without bringing the spheres into contact and by maintaining a constant axial spacing for a given porosity. The spheres in the near-wall region were specially manufactured to sustain the bulk porosity of the bed, thereby also reducing wall effects and wall channelling. The axial spacings were varied to achieve pseudo-homogeneous porosities of 0.36, 0.39 and 0.45 (Rousseau and Van Staden, 2008; Kgame, 2010; Preller, 2011). This study only focussed on the experiments with a porosity of 0.36 (termed BETS 0.36). Braiding or hot nitrogen gas was introduced directly below the spheres and allowed to mix with flow from 16 cold nitrogen gas streams, thereby supplying a constant block-shaped velocity profile to the bed (Rousseau and Van Staden, 2008). Four experimental runs were conducted for each particle or superficial Reynolds number, ranging from 1000 to 40000. The Reynolds numbers were varied indirectly by adjusting the system pressure between 1 and 38 bar(a). In addition, two radial temperature profiles were measured using thermocouples situated one third from the bottom and top of the packing, respectively (Kgame, 2010). This study was restricted to the bottom layer thermocouples.

Previously, Kgame (2010) conducted a thorough uncertainty analysis on several variables associated with the BETS experiments and HPTU setup. This was followed by developing a complete set of normalised temperature data over the four experimental runs that were conducted for each Reynolds number and pseudo-homogeneous porosity. Afterwards, the normalised temperature profiles were subjected to polynomial regression to evaluate the fluid effective thermal conductivity using the CFD code, Flo++ with a specific data search technique. In a subsequent, preliminary study, Preller (2011) simulated a single case of the BETS experiments, with a superficial Reynolds number of 3000 and a porosity of 0.36. In contrast to Kgame (2011), Preller (2011) utilised STAR-CCM+® and only specified the inlet conditions. Subsequently, the simulated temperature profiles were extracted and compared with the normalised BETS experimental temperature data. Good agreement between the simulated and experimental temperature profiles was achieved. Nonetheless, the simulated temperature profiles moderately overpredicted the central radial temperatures in the packing. These differences were partially caused by the large temperature gradients within the radial centre of the bed (Preller, 2011; Du Toit *et al*., 2012b).

1.2 Research problem statement

Heat transfer mechanisms in packed beds are not fully understood (Wen and Ding, 2006; Rousseau and Van Staden, 2008). Research on thermal dispersion gave rise to correlations with considerable amounts of empiricism. This resulted from incorporating a limited number of heat transfer mechanisms, as well as characterising the porous structure with insufficient complexity (Cheng *et al.*, 1999; Van Antwerpen, 2009). Consequently, these correlations have limited applicability and occasionally, uncertain validity.

The High Pressure Test Unit formed part of the Heat Transfer Test Facility, which was developed for PBMR SOC (Ltd.). The High Pressure Test Unit was constructed to conduct a comprehensive set of separate effects tests for the purpose of validating existing thermohydraulic correlations (Rousseau and Van Staden, 2008). The separate effect tests included the Braiding Effect Test Section experiments which investigated the increased thermal dispersion due to the effects of the porous structure on the flow (Kgame, 2010). The Braiding Effect Test Section experimental temperature data requires evaluation. Computational fluid dynamics has been proven to accurately model the flow physics involved with fluid flow through packed beds and can consequently be used to model thermal dispersion in a packed bed (Hassan, 2008; Preller, 2011; Van der Merwe, 2014).

1.3 Research aim

It is required to evaluate the thermal dispersion results of the Braiding Effect Test Section separate effects tests numerically.

1.4 Research objectives

1. Construct structured pebble beds, representative of the Braiding Effect Test Sections, by importing centroid coordinate data into SolidWorks® using a linear pattern macro.

2. Verify the CFD results obtained by Preller (2011) by using STAR-CCM+® with similar computer aided design (CAD) models, symmetry assumptions and simulation settings, accompanied by a distinctive and preliminary simulation methodology.

3. Conduct residual analyses to determine the optimal simulation settings that will minimise the residuals of the continuity, momentum and energy equations.

4. Investigate the effect of different symmetry assumptions or periodic boundary conditions on the simulated temperature profiles.

5. Develop a suitable simulation methodology based on the results of mesh analyses and mesh independency studies, integrated turbulence model assessments, temperature extraction methods, as well as wall treatment considerations, along with other associated tests.

6. Develop appropriate stability conditions and convergence criteria.

7. Numerically evaluate the normalised temperature profiles of selected Braiding Effect Test Section experiments by employing the developed simulation methodology using STAR-CCM+®.

1.5 Research overview

This study is an extension of the preliminary work done by Preller (2011). Consequently, Reynolds numbers up to 40000 were simulated to numerically evaluate the normalised BETS temperature profiles presented in Kgame (2010). Previous studies (Kgame, 2010; Preller, 2011) used symmetry assumptions in simulating the BETS experiments to decrease the amount of computational resources required. The incorporation of symmetry or periodic boundary conditions in the numerical modelling of packed beds is a common practice (Nijemeisland and Dixon, 2004; Hassan, 2008; Yang *et al*., 2010; Shams *et al.*, 2012). STAR-CCM+® was used to evaluate the effect of several different symmetry and periodic boundary conditions on the simulated temperature profiles. It was concluded, that the results (Kgame, 2010; Preller, 2011) were affected to some extent. Consequently, a full model without the abovementioned boundary conditions was simulated. This resulted in large meshes with nearly 40 million cells. The large number of cells resulted in several simulation difficulties in part due to the highly oscillatory nature of the flow and the occurrence of high temperature gradients.

Remediation was done by conducting comprehensive analyses on mesh quality, residuals and temperature profiles. Subsequently, the results were used to develop a suitable simulation methodology to overcome simulation difficulties. The methodology resulted in good agreement between the numerically simulated and experimentally measured temperature profiles. In addition, the predicted central radial temperatures are closer to the experimentally measured values compared to the corresponding values obtained by Preller (2011). This improvement is

partially attributed to using a locally refined mesh with thin prism layers in the packed region, along with the large eddy simulation (LES) model accompanied by the Smagorinsky subgrid scale (SGS) model.

1.6 Limitations and assumptions of this study

This study is limited to heat transfer by means of thermal dispersion or enhanced thermal diffusion. Heat transfer through and from the spheres were not investigated in the BETS separate effects tests. Consequently, all the walls, including the spheres are assumed to be adiabatic surfaces. Near-wall effects and wall channelling are also not considered due to the structured nature of the bed.

1.7 Chapter outline

Chapter 2: Theoretical background of CFD

This chapter provides a thorough overview of the underlying laws and principles pertaining to CFD.

Chapter 3: Literature overview

Following the laws and principles pertaining to CFD, this chapter represents an overview on packed beds with their structural and thermohydraulic characterisation.

Chapter 4: Simulation methodology

This chapter features a literature verification study, symmetry investigation, as well as a comprehensive simulation methodology development.

Chapter 5: CFD validation of selected BETS experiments

Following the methodology development in the previous chapter, this chapter aimed at validating the experimental data of a selected set of BETS experiments.

Chapter 6: Conclusions and recommendations

Finally, this chapter concludes the dissertation and provides recommendations for future work.

CHAPTER 2: THEORETICAL BACKGROUND OF CFD

2.1 Introduction

This chapter pertains to the underlying laws and principles upon which computational fluid dynamics (CFD) analysis is based. An overview will be given of the relevant fluid mechanics, followed by the specific incorporation thereof in the numerical analysis of turbulent flows.

2.2 Fluid mechanics

Fluids are mostly continuous substances and classified either as liquids or gases, or as a mixture of both. Fluids are highly prone to deformation when subjected to external surface or body forces, which induce fluid flow. Surface forces are pressure and viscous forces, whereas body forces include gravitational, rotational and electromagnetic forces, among others (Ferziger and Perić, 2002; Versteeg and Malalasekera, 2007).

2.2.1 Conservation equations

Fluid flow is governed by three fundamental laws of physics when excluding electromagnetic, nuclear and relativistic phenomena. These fundamental laws comprise of the law of mass conservation, Newton's second law of motion and the first law of thermodynamics. The application of the governing laws results in the conservation equations of fluid flow, known as the continuity, momentum and energy equations, respectively (Versteeg and Malalasekera, 2007; Welty *et al*., 2008).

Consider a fluid as a continuum and neglect microscopic or inter-atomic length scales. Then, by using the Eulerian approach, the three-dimensional, Cartesian, differential, vector form of the continuity equation for an infinitesimal control volume is given by (Chung, 2002; Ferziger and Perić, 2002; Versteeg and Malalasekera, 2007):

$$\frac{\partial \rho}{\partial t} + \boldsymbol{\nabla} \bullet \rho \boldsymbol{u} = 0 \tag{2.1}$$

where ρ is the fluid density (kg/m^3), t is time (s) and $\boldsymbol{u}$ is the velocity vector, $\boldsymbol{u} = u_x\boldsymbol{i} + u_y\boldsymbol{j} + u_z\boldsymbol{k}$ (m/s).

The previous considerations can also be applied to Newton's second law of motion to develop the conservation equation for linear momentum (Ferziger and Perić, 2002; Welty *et al*., 2008; Munson *et al*., 2009):

$$\frac{\partial(\rho\boldsymbol{u})}{\partial t} + \boldsymbol{\nabla}\bullet\rho\boldsymbol{u}\boldsymbol{u} = \boldsymbol{\nabla}\bullet\boldsymbol{\tau} + \rho\boldsymbol{b} \tag{2.2}$$

Equation 2.2 is known as the Cauchy or the conservative form of the momentum equation and is also applicable to inertial control volumes, unlike the non-conservative form which is given by:

$$\rho\left[\frac{\partial\boldsymbol{u}}{\partial t} + \boldsymbol{u}\bullet\boldsymbol{\nabla}\boldsymbol{u}\right] = \rho\frac{D\boldsymbol{u}}{Dt} = \boldsymbol{\nabla}\bullet\boldsymbol{\tau} + \rho\boldsymbol{b} \tag{2.3}$$

where $D\boldsymbol{u}/Dt$ is the substantial derivative of the velocity vector or the total acceleration (m/s^2), which includes the local and convective acceleration. In addition, $\boldsymbol{\tau}$ is the Cauchy second-order stress tensor (Pa or N/m^2), which will be discussed in greater detail in Section 2.2.2, and $\boldsymbol{b}$ is the vector sum of all body forces (N/kg or m/s^2). Equation 2.2 and Equation 2.3 are valid for any continuum in both mobile and stationary states.

Similarly, the first law of thermodynamics can be used to derive the energy conservation equation (Versteeg and Malalasekera, 2007; Siemens PLM Software, 2017):

$$\rho\left[\frac{\partial E}{\partial t} + \boldsymbol{\nabla}\bullet E\boldsymbol{u}\right] = \rho\frac{DE}{Dt} = \boldsymbol{\nabla}\bullet(\boldsymbol{\tau}\bullet\boldsymbol{u}) - \boldsymbol{\nabla}\bullet\boldsymbol{q}" + \rho\boldsymbol{b}\bullet\boldsymbol{u} + S_E \tag{2.4}$$

where E is the total specific energy (J/kg), $\boldsymbol{q}"$ is the three-dimensional heat flux vector, $\boldsymbol{q}" = q"_x\boldsymbol{i} + q"_y\boldsymbol{j} + q"_z\boldsymbol{k}$ (W/m^2) and S_E is an energy source (W/m^3).

Equations (2.1) to (2.4) are known as the conservation equations of fluid flow, which are used in modelling continuum mechanics. Nevertheless, supplementary information regarding the stress

tensor ($\boldsymbol{\tau}$) is required prior to their specific application (Munson *et al*., 2009; Siemens PLM Software, 2017).

2.2.2 Viscous stresses

In laminar flow, shear stress results from the microscopic actions of molecules, whereas in turbulent flow shear stress results from macroscopic fluctuations (Welty *et al*., 2008). A discussion on these flow regimes will follow in Section 2.2.4.

The relationship between shear stress and the shear rate of a fluid can be broadly described by the Herschel-Bulkley model (Rhodes, 2008):

$$\tau = \kappa \dot{\gamma}^n + \tau_y \tag{2.5}$$

where τ is the shear or tangential stress (Pa), κ is the consistency index (N·s^n/m^2), $\dot{\gamma}$ is the rate of shear strain or deformation (s^{-1}), n is the dimensionless flow behaviour index and τ_y is the yield stress (Pa). However, by limiting our case to Newtonian fluids, κ equals the Newtonian or dynamic viscosity, μ (Pa·s), the shear stress-shear rate relationship becomes linear ($n = 1$) and τ_y can be neglected. Dynamic viscosity is a fluid property which expresses a fluid's ability to resist the rate of shear strain or deformation when subjected to shear forces (Welty *et al*., 2008).

Subsequently, for Newtonian fluids Equation 2.5 becomes (Ferziger and Perić, 2002; Versteeg and Malalasekera, 2007; Welty *et al*., 2008; Schlichting and Gersten, 2017):

$$\tau_{ij} = \tau_{ji} = 2\mu\dot{\gamma}_{ij} \tag{2.6}$$

where

$$\dot{\gamma}_{ij} = \frac{1}{2}\left(\frac{\partial u_i}{\partial x_j} + \frac{\partial u_j}{\partial x_i}\right) \tag{2.7}$$

The combination of Equation 2.6 and Equation 2.7 results in Stokes' viscosity relations for shear stress in laminar flow. For the single index notation, the indices (i, j) correspond to any of the

Cartesian components ($x, y\ or\ z$). In the case of the Cartesian coordinates, let (x_x, x_y, x_z) correspond to (x, y, z), respectively. In the double index notation, the first index denotes the directional axis normal to the acting shear stress, whereas the second index indicates the directional axis along which the stress is acting. If the indices in Equation 2.7 differ, as in this case, then it is known as a linear shearing deformation component, otherwise if they are identical it is known as a linear elongating deformation component. The former corresponds to shear stresses, whereas the latter is associated with normal stresses.

Normal stresses are the combined result of pressure and viscous forces. The viscous contribution to normal stress is derived based on Hooke's law for an elastic solid. The total normal stress is given by (Versteeg and Malalasekera, 2007; Welty *et al.*, 2008; Schlichting and Gersten, 2017):

$$\sigma_{ii} = -P + 2\mu\dot{\gamma}_{ii} + \lambda(\boldsymbol{\nabla}\bullet\boldsymbol{u}) \tag{2.8}$$

where P is static pressure (Pa) and λ is the so-called second or bulk viscosity (Pa·s), which relates stresses to volumetric deformation. A good approximation is generally achieved when using Stokes' assumption of $\lambda = -\frac{2}{3}\mu$.

Finally, by considering Equation 2.6 to Equation 2.8, the stress tensor ($\boldsymbol{\tau}$) or molecular rate of momentum transport is given by (Ferziger and Perić, 2002; Pozrikidis, 2011):

$$\boldsymbol{\tau} = -\left[P + \frac{2}{3}\mu(\boldsymbol{\nabla}\bullet\boldsymbol{u})\right]\boldsymbol{I} + 2\mu\dot{\boldsymbol{\gamma}} \tag{2.9}$$

where $\boldsymbol{I}$ is the unit tensor and $\dot{\boldsymbol{\gamma}}$ is the rate of deformation tensor (s^{-1}), which is equated by:

$$\dot{\boldsymbol{\gamma}} = \frac{1}{2}[\boldsymbol{\nabla}\mathbf{u} + (\boldsymbol{\nabla}\mathbf{u})^T] \tag{2.10}$$

Substituting Equation 2.10 into Equation 2.9 results in the following:

$$\boldsymbol{\tau} = \begin{bmatrix} \sigma_{xx} & \tau_{xy} & \tau_{xz} \\ \tau_{yx} & \sigma_{yy} & \tau_{yz} \\ \tau_{zx} & \tau_{zy} & \sigma_{zz} \end{bmatrix} \tag{2.11}$$

The diagonal elements are normal stresses, whereas the remaining elements are shear stresses. This equation can now be inserted into the conservation equations of momentum and energy, Equation 2.2 or Equation 2.3, and Equation 2.4, respectively, for the specific modelling of Newtonian fluids.

2.2.3 Navier-Stokes equations

The previous section derived the stress tensor ($\boldsymbol{\tau}$) for a Newtonian fluid. Equation 2.11 can subsequently be substituted into momentum conservation equation (Equation 2.3) to arrive at the non-conservative form of the well-known Navier-Stokes equation (Versteeg and Malalasekera, 2007; Welty *et al.*, 2008):

$$\rho\frac{D\boldsymbol{u}}{Dt} = -\boldsymbol{\nabla}P - \boldsymbol{\nabla}\left(\frac{2}{3}\mu\boldsymbol{\nabla}\bullet\boldsymbol{u}\right) + \boldsymbol{\nabla}\bullet(\mu\boldsymbol{\nabla}\mathbf{u}) + \boldsymbol{\nabla}\bullet(\mu\boldsymbol{\nabla}\bullet\mathbf{u}) + \rho\boldsymbol{b} \tag{2.12}$$

This equation is the differential characterisation of Newton's second law of motion for any Newtonian fluid. The Navier-Stokes equation is reduced considerably when considering incompressible flows ($\boldsymbol{\nabla}\bullet\mathbf{u} = \mathbf{0}$) with constant viscosity (Welty *et al.*, 2008; Munson *et al.*, 2009):

$$\rho\frac{D\boldsymbol{u}}{Dt} = -\boldsymbol{\nabla}P + \mu\boldsymbol{\nabla}^2\mathbf{u} + \rho\boldsymbol{b} \tag{2.13}$$

In addition, another simplification of the Navier-Stokes equation involves assuming or by approximating inviscid flow ($\mu = 0$), whereby Equation 2.12 is reduced to Euler's motion equation:

$$\rho\frac{D\boldsymbol{u}}{Dt} = -\boldsymbol{\nabla}P + \rho\boldsymbol{b} \tag{2.14}$$

Euler's motion equation can typically be applied in flow regimes where the inertial forces dominate over the viscous forces. Other forms and applications of the Navier-Stokes equations and their accompanying continuity and energy conservation equations are commonly discussed in literature (Chung, 2002; Pozrikidis, 2011; Schlichting and Gersten, 2017).

2.2.4 Flow regimes and boundary layer concepts

The topic on flow regimes has been mentioned briefly in the previous sections. Viscous flows display two distinct flow regimes. The first is an ordered flow type called laminar flow wherein adjacent fluid layers slide easily over each other. Any mixing between the layers is limited to the molecular level. Secondly, we have the turbulent flow regime wherein fluid parcels are interchanged between layers. This results in flow with a fluctuating nature. Turbulence can subsequently be quantified by the well-known Reynolds number which represents the ratio of the inertial to the viscous forces. The dimensionless Reynolds number (Re) for flow in circular pipes is given by (Welty *et al*., 2008, Incropera *et al*., 2013):

$$Re = \frac{\rho u D}{\mu} = \frac{uD}{\nu} \tag{2.15}$$

where u is the fluid velocity (m/s), D is the pipe diameter (m) and ν is the kinematic viscosity of the fluid (m^2/s), $\nu = \frac{\mu}{\rho}$. Pipe flow has a critical Reynolds number of 2300, meaning this is generally where the transition from laminar to turbulent flow commences.

The concept of a velocity boundary layer can now be formulated. Figure 2-1 represents a flat plate in the x,z-plane subjected to a fluid with an initially uniform velocity profile with magnitude u_∞. This results in a variation in velocity in the x,y-plane which will subsequently be considered. The velocity components in the figure, u and v, correspond to u_x and u_y, respectively. The coexistence of both laminar and turbulent flow conditions is a common phenomenon in boundary layer development. The streamwise fluid motion is retarded in the near-wall region ($y \approx 0$) with boundary layer growth in the x-direction. Subsequently, the local shear stress at the surface changes as the boundary layer thickness (δ) is increased in the y-direction (Incropera *et al*., 2013).

Laminar flow is observed until the characteristic length (x) reaches a critical value (x_c). Increasing distance from the leading edge results in a transitional region where conversion from laminar to turbulent flow originates, followed by the fully turbulent boundary layer. In the latter part of the boundary layer large fluid parcels are in motion, which exhibit extremely irregular flow behaviour. A large amount of mixing occurs within the boundary layer, wherein the fluid parcels with high velocity are moved towards the wall region, whereas the less mobile fluid parcels are transferred deeper into the free stream. Streamwise vortices greatly contribute towards the mixing process.

These vortices or streaks are formed near the surface and display rapid growth and decay rates (Incropera *et al*., 2013).

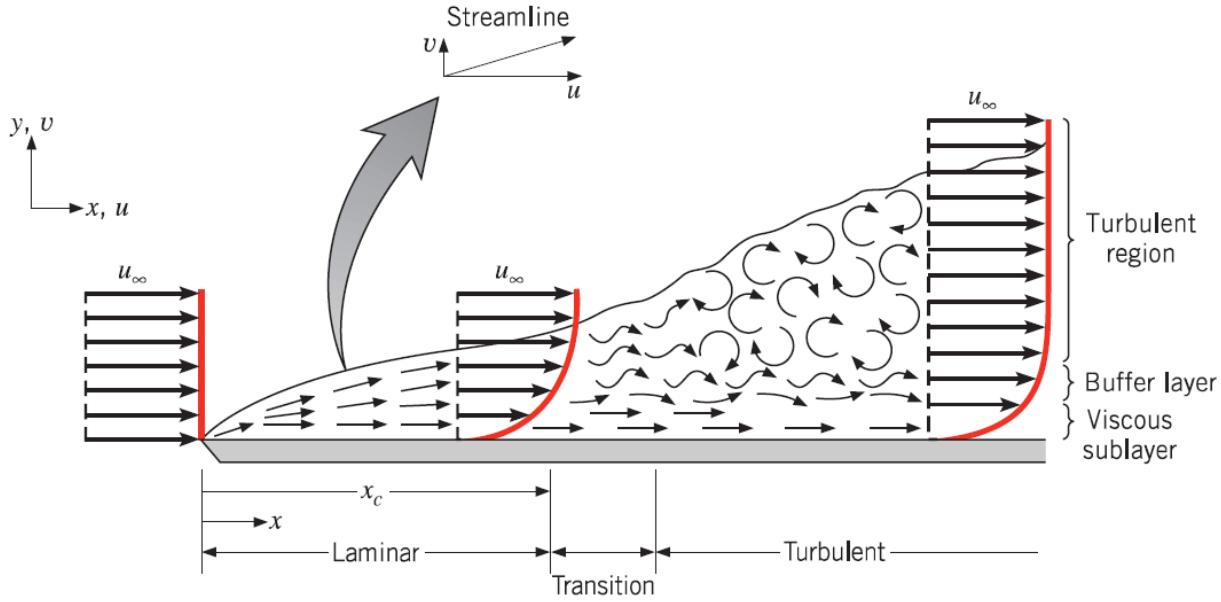

Figure 2-1: Velocity boundary layer development over a flat plat (Incropera *et al*., 2013)

As the velocity boundary layer is developed, the fully turbulent boundary layer forms three distinct regions. The first is a viscous sublayer wherein fluid motion is dominated by diffusion, resulting in a virtually linear velocity profile. An adjoining buffer layer is formed on top of the viscous sublayer. This second region displays fluid transport in which the contributions of diffusion and turbulent mixing are similar. The buffer layer is followed by a turbulent region wherein fluid motion is controlled by means of turbulent mixing. The velocity profile in the turbulent boundary layer is quickly flattened by mixing in both the buffer layer and the turbulent region. This results in large velocity gradients occurring within the viscous sublayer. Consequently, the local surface shear stress increases as the laminar boundary layer is transitioned into the turbulent boundary layer with increasing characteristic length (Incropera *et al*., 2013).

The abovementioned can be extended to arrive at the well-known law of the wall in which near-wall turbulent flows are characterised by empirical relationships. The streamwise velocity in near-wall flow has been observed to vary in a logarithmic manner with increasing distance from the surface in the normal, y-direction (increasing y/δ). This behaviour is common in both internal and

external flows. Additional near surface observations conclude that the effects of inertial forces, pressure gradients and distant eddies on flow statistics are insignificant. In contrast, two main mechanisms that do influence the near wall flow statistics are the momentum transfer rate to the surface and the molecular momentum diffusion. The momentum transfer rate is equal to the local shear stress (Wilcox, 2006).

Following the law of the wall description, the friction velocity (u_τ) is given by (Davidson, 2004; Wilcox, 2006):

$$u_\tau = \sqrt{\frac{\tau_w}{\rho}} \tag{2.16}$$

where τ_w is the wall or surface shear stress (N·s/m^2). The surface shear stress can be used instead of the local shear stress since the latter fluctuates insignificantly in the normal direction. The friction velocity is used to define both the dimensionless velocity (u^+) and wall distance (y^+) as follow (Wilcox, 2006; Welty *et al.*, 2008):

$$u^+ = \frac{\bar{u}_x}{u_\tau} \tag{2.17}$$

and

$$y^+ = \frac{u_\tau y}{\nu} \tag{2.18}$$

firstly where $\bar{u}_x$ is the time-averaged streamwise velocity (m/s) and secondly where y is the normal wall distance (m). The y^+ values will subsequently increase with increasing turbulence. Furthermore, in the turbulent boundary layer, these dimensionless parameters mostly correlate in a logarithmic manner as depicted by the typical velocity distribution in Figure 2-2.

Three distinct layers can be identified from Figure 2-2, which correspond to those in the turbulent boundary layer of Figure 2-1. The correlations applicable to each layer in the inner region of the turbulent boundary are shown. Although the viscous sublayer or laminar layer ends at approximately $y^+ = 5$, it is not uncommon to extend the linear relationship to $y^+ = 11$, where after

the buffer layer provides a more suitable, logarithmic correlation. Consequently, the region $11 < y^+ \leq 500$ is referred to as the log layer or log-law of the wall. Furthermore, the log layer breaks down at $y^+ > 500$, resulting in a velocity-defect layer or Clauser defect law, which is situated in the outer region of the turbulent boundary layer (Davidson, 2004; Wilcox, 2006; Siemens PLM Software, 2017).

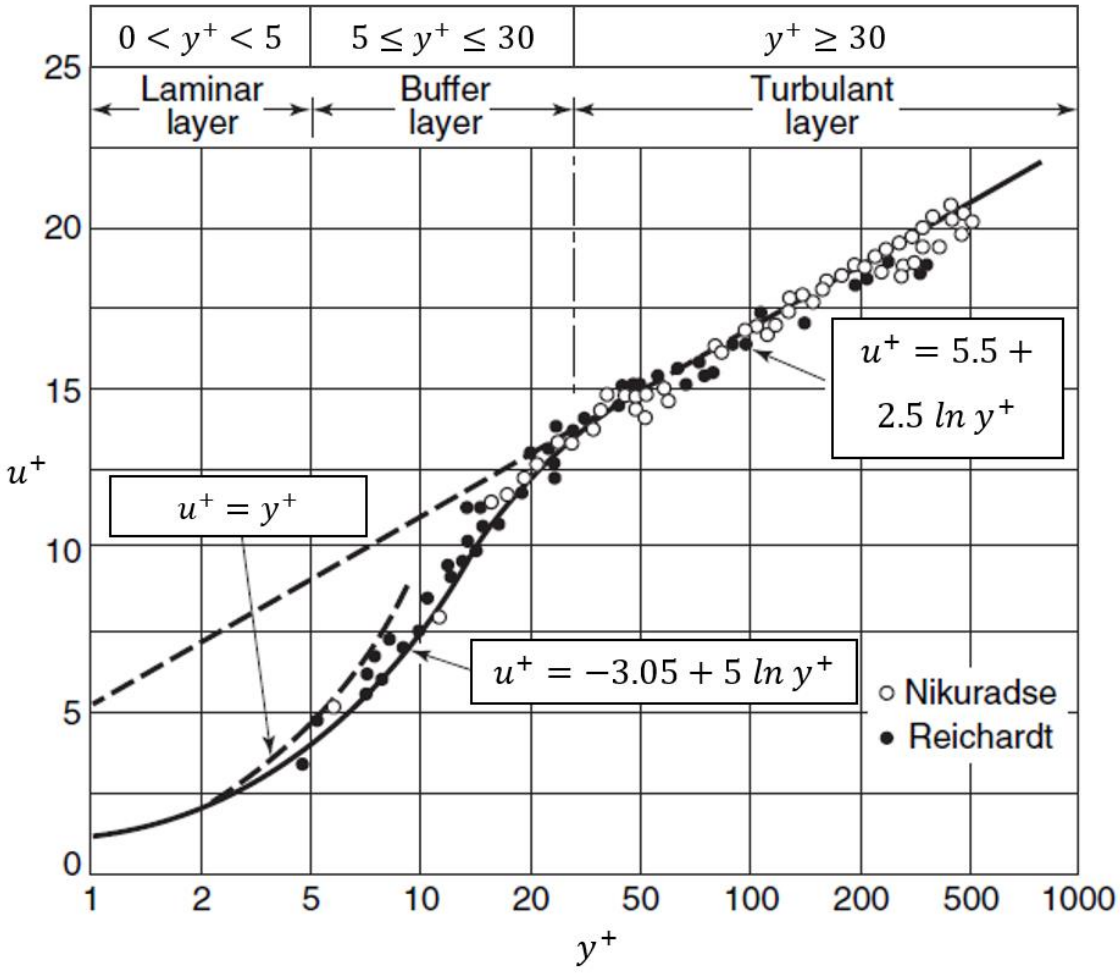

Figure 2-2: Turbulent boundary layer velocity distribution (Adapted from Welty *et al*., 2008)

Additional boundary layer concepts such as the thermal boundary layer and concentration boundary layer can be found in Incropera *et al.* (2013). The prediction of near-wall flow statistics is vital in the numerical modelling of turbulence and forms the basis for wall treatment models (Siemens PLM Software, 2017).

2.3 Numerical analysis of turbulent flow

Turbulent flows display unsteady behaviour wherein the instantaneous flow field rapidly fluctuates in all directions. In addition, turbulence is associated with a high amount of vorticity. Turbulent diffusion is the process by which the mixing rate of conserved quantities at different concentrations is increased by means of turbulence. However, this process is countered by means of dissipation where the fluid's kinetic energy is reduced by means of viscous forces. Dissipation is consequently an irreversible process which converts the fluid's kinetic energy into internal energy. Although turbulence contains coherent structures, many flow properties still fluctuate in a random manner with a wide range of time and length scales. CFD has become an attractive tool to numerically model and analyse turbulent flows (Ferziger and Perić, 2002).

2.3.1 Reynolds-averaged Navier-Stokes models

2.3.1.1 Reynolds averaging

Turbulent flows contain a great deal of fluctuations as mentioned earlier. These fluctuations can be averaged out numerically by means of the Reynolds averaging processes. The application of this process to the Navier-Stokes equation (Equation 2.12) results in the well-known Reynolds-averaged Navier-Stokes (RANS) equations.

The Reynolds averaging process will now be outlined. Consider a statistically steady flow, then by using the same index notation as in Section 2.2.2, any scalar variable can be represented by the summation of its time-averaged value and the fluctuation around that value (Ferziger and Perić, 2002):

$$\phi(x_i, t) = \bar{\phi}(x_i) + \phi'(x_i, t) \tag{2.19}$$

with the time-averaged value computed as:

$$\bar{\phi}(x_i) = \lim_{T\to\infty} \frac{1}{T} \int_0^T \phi(x_i, t)\, dt \tag{2.20}$$

where $\phi(x_i, t)$ is any scalar that is a function of space and time, $\bar{\phi}(x_i)$ is the time-average of that scalar and $\phi'(x_i, t)$ is the fluctuation around that averaged value. Additionally, T is the time interval

over which the scalar is averaged. In the event of unsteady flow, ensemble averaging should be used.

The conservation equations (Equation 2.1, Equation 2.4 and Equation 2.12) can be time-averaged by using Equation 2.20 to arrive at the following universal equation conservation equation (Ferziger and Perić, 2002):

$$\frac{\partial(\rho\bar{\phi})}{\partial t}+\frac{\partial}{\partial x_j}\left(\rho\bar{u}_j\bar{\phi}+\rho\overline{u'_j\phi'}\right)=\frac{\partial}{\partial x_j}\left(\Gamma\frac{\partial\bar{\phi}}{\partial x_j}\right) \tag{2.21}$$

where Γ is the diffusivity for the chosen scalar function ϕ. Substitution of ϕ with the velocity components for example, will result in the RANS equations. Additional terms arise as a result of the averaging process, namely Reynolds stresses ($\rho\overline{u'_\iota u'_\jmath}$) and turbulent scalar flux ($\rho\overline{u'_\iota\phi'}$). Consequently, the conservation equations are not closed and therefore approximations are required to obtain a closed set of equations. These approximations are termed turbulence models which will be discussed in subsequent sections.

2.3.1.2 Eddy viscosity and diffusivity

Prior to discussing turbulence models, it is useful to give an overview on eddy viscosity and diffusivity. It is assumed that turbulent effects are characterised by increasing viscosity. Subsequently, similar to Equation 2.9, the Boussinesq approximation deems the Reynolds stresses proportional to deformation rates as follows (Ferziger and Perić, 2002; Versteeg and Malalasekera, 2007):

$$\tau_{ij}=-\rho\overline{u'_\iota u'_\jmath}=\mu_t\left(\frac{\partial\bar{u}_i}{\partial x_j}+\frac{\partial\bar{u}_j}{\partial x_i}\right)-\frac{2}{3}\rho\delta_{ij}k \tag{2.22}$$

where μ_t is the turbulent eddy viscosity (Pa·s), δ_{ij} is the Kronecker delta ($\delta_{ij}=0$ if $i\neq j$ and $\delta_{ij}=1$ if $i=j$) and k is the turbulent kinetic energy (J/kg) defined as:

$$k=\frac{1}{2}\overline{u'_\iota{}^2}=\frac{1}{2}\left(\overline{u'_x{}^2}+\overline{u'_y{}^2}+\overline{u'_z{}^2}\right) \tag{2.23}$$

Equation 2.22 is also known as the eddy viscosity model for Reynolds stress. In addition, the turbulent scalar flux is represented by the eddy-diffusion model for scalars:

$$-\rho\overline{u'_\iota\phi'} = \Gamma_t \frac{\partial\bar{\phi}}{\partial x_i} \tag{2.24}$$

where Γ_t is the turbulent or eddy diffusivity. Lastly, the turbulent Prandtl or Schmidt number (σ_t) is defined as:

$$\sigma_t = \frac{\mu_t}{\Gamma_t} \tag{2.25}$$

2.3.1.3 Eddy viscosity models

As mentioned earlier, additional terms arise in the conservation equations as a result of the Reynolds averaging process. In the case of the momentum transport equation, these are known as Reynolds stresses. The resulting Reynolds stress tensor is similar to Equation 2.11. In general, RANS turbulence models use two approaches to model this stress tensor. The first being eddy viscosity models and the second being Reynolds stress transport models (Siemens PLM Software, 2017). This section will be devoted to the former approach.

Eddy viscosity models assume an analogy between turbulence and the molecular gradient-diffusion process. The Reynolds stresses are subsequently quantified in terms of mean flow properties by means of the eddy viscosity. Hence, these models are commonly based on the Boussinesq approximation (Equation 2.22) which assumes an isotropic eddy viscosity along with a linear relationship between the Reynolds stresses and deformation rates. Nevertheless, the application of some models has been extended to non-linear relationships (Siemens PLM Software, 2017). Turbulence models are commonly grouped by the number of additional transport equations that they require to obtain a closed set of equations. Table 2.1 provides a summary of common eddy viscosity models, excluding their variants. In many cases, the models become more accurate and universal as the number of accompanying transport equations are increased at the expense of computational resources (Versteeg and Malalasekera, 2007).

Table 2.1: Common eddy viscosity models

Additional transport equations	Eddy viscosity model
Zero	Mixing length model
One	Spalart-Allmaras model
Two	k-ε models
	k-ω models

We will restrict our attention to the more complex, two-equation models. The first of these models under consideration is the k-ε models wherein transport equations are set up for both the turbulent kinetic energy, k, as well as the turbulent dissipation rate, ε. This forms a closed set of equations whereby the eddy viscosity can be determined. This model has several variants, six of them are incorporated into STAR-CCM+® (Siemens PLM Software, 2017). The following assessment of the Standard k-ε model is given by Versteeg and Malalasekera (2007): It is the least complex turbulence model requiring only initial and, or boundary conditions. It is a well-grounded model and the most broadly validated. It is capable of accurately describing many industry related flows. However, the model breaks down and experiences reduced performance when considering certain unrestricted flows, flows around curvatures, swirling flows, rational flows and fluid flows that require the anisotropy of turbulence to be accounted for.

Secondly, the k-ω models are considered. These models are also equipped with two additional transport equations to evaluate the eddy viscosity. The one equation models the kinetic energy, k, whereas the other models the specific dissipation rate, ω (s^{-1}). This specific dissipation rate is expressed per unit turbulent kinetic energy, making it directly proportional to ε/k. The Standard and shear-stress transport (SST) k-ω models have been implemented into STAR-CCM+® (Siemens PLM Software, 2017). According to Wilcox (2006), the k-ω model has several advantages over the k-ε model and has consequently exceeded its usage. The k-ω model provides improved accuracy for boundary layers, both under favourable or adverse pressure gradients. Furthermore, the model allows simple integration throughout the boundary layer, including the viscous sublayer region, while excluding the need for any specific viscous corrections. Nevertheless, including these corrections results in accurate characterisation of subtle turbulent kinetic energy phenomena in the near wall region and provides reasonable results when modelling transitional flow within the boundary layer. Additionally, the model can accurately describe spreading rates for shear free flows and properties associated with separated flows. However, owing to the Boussinesq approximation, the model also fails to predict secondary fluid motion in noncircular ducts. Siemens PLM Software (2017) states that another disadvantage is

the sensitivity of boundary layer computations to the free stream specific dissipation rates. This makes the model extremely vulnerable to inlet boundary conditions when modelling internal fluid flows.

2.3.1.4 Reynolds stress model

The Boussinesq approximation excludes the anisotropy of turbulence and has a few other drawbacks as discussed briefly in the previous section. This leads us to the second approach of RANS turbulence modelling which utilises the Reynolds stress model (RSM) and its variants. The RSM turbulence model is also known as the second-moment closure model. This model enables the direct computation of all components within the Reynolds stress tensor by solving their governing transport equations. This results in a total of seven additional transport equations to be solved (six independent Reynolds stresses). Complex relations between the Reynolds stresses and strain or deformation rates can subsequently be modelled. This model also has the potential of producing more accurate flow predictions than eddy viscosity models. This potential can be attributed to Reynolds stress modelling, which allows the inherent incorporation of the effects of flow phenomena such as that of anisotropic turbulence, flows around curvatures, rotational flows and flows which exhibit high strain rates. However, the model is more complex and computationally expensive than eddy viscosity models (Ferziger and Perić, 2002; Versteeg and Malalasekera, 2007; Siemens PLM Software, 2017).

The RSM model uses the exact Reynolds stress transport equation. The equation is derived by Reynolds-averaging the resulting product of the instantaneous Navier-Stokes equations when multiplied with a fluctuating property. The resulting equation still requires three terms to be modelled. These terms include the turbulent diffusion, the dissipation rate, as well as the pressure-strain term. The latter term is considered to be the most challenging to model. STAR-CCM+® follows one of two modelling approaches in this matter: a linear pressure strain model or a quadratic pressure strain model (Ferziger and Perić, 2002; Versteeg and Malalasekera, 2007; Siemens PLM Software, 2017). The reader is referred to the sourced literature for more detail.

Versteeg and Malalasekera (2007) provides the following assessment of the RSM model: It is the most universal among classical turbulence models. Like the k-ε turbulence models, it also requires merely initial and, or boundary conditions to be specified. It generally provides an accurate prediction for all mean flow properties and Reynolds stresses. Unfortunately, it is much more

computationally expensive than other RANS turbulence models and its performance is restricted in situations where the modelled representation of turbulent dissipation rate breaks down, such as unconfined recirculating flows.

2.3.2 Scale-resolving simulations

Several behavioural differences have been observed between small and large eddies. Small eddies tend to exhibit near universal, isotropic flow behaviour, especially in high Reynolds number flows. In contrast, large eddies display more anisotropic flow behaviour and they participate in energy exchanges with mean flow. In addition, the large scales contain much more energy and they offer enhanced transport efficiency of conserved properties owing to their size, as well as strength. Consequently, the flow behaviour of large eddies is influenced by factors such as the flow domain, boundary conditions, as well as body forces. RANS turbulence models follow a collective approach, wherein all eddies are governed by a single model although behaviour differences are common. The collective treatment of eddies consequently sacrifices the universality and robustness of turbulence models. The collective eddy treatment and some of its consequences are avoided when using scale-resolving approaches such as large eddy simulation (LES). LES is an inherently transient technique which uses a spatial filter function to separate large eddies from small ones at the filter cut-off width, Δ (m). A time-dependent solution is computed for the large eddies, hence the larger turbulent length scales are resolved, whereas the smaller eddies are modelled by a subgrid scale (SGS) model (Ferziger and Perić, 2002; Versteeg and Malalasekera, 2007).

2.3.2.1 Large eddy simulation

The equations for LES are developed by utilising spatial filtering instead of time-averaging as in the case of RANS. Any instantaneous flow variable (ϕ) can be decomposed into a spatially filtered value ($\bar{\phi}$) and a sub-filtered or subgrid value (ϕ') (Versteeg and Malalasekera, 2007; Hassan, 2008; Siemens PLM Software, 2017):

$$\phi(x_i, t) = \bar{\phi}(x_i, t) + \phi'(x_i, t) \tag{2.26}$$

where the filtered value is associated with larger, resolved scales and the subgrid value with the smaller, unresolved scales. The spatial filtering is accomplished by means of volume averaging

over a specific filtering function $G(x_i, x_i', \Delta)$ (Versteeg and Malalasekera, 2007; Hassan, 2008; Siemens PLM Software, 2017):

$$\bar{\phi}(x_i, t) = \iiint_{-\infty}^{\infty} G(x_i, x_i', \Delta)\ \phi(x_i', t)\ dx_1' dx_2' dx_3' \tag{2.27}$$

The box or top-hat filter kernel is preferred when using the finite volume method for CFD. Other common filter functions are the Gaussian and spectral cut-off filters. The filter cut-off width, Δ, is usually characterised by (Ferziger and Perić, 2002; Versteeg and Malalasekera, 2007; Siemens PLM Software, 2017):

$$\Delta = \sqrt[3]{\Delta_x \Delta_y \Delta_z} \tag{2.28}$$

where Δ_x, Δ_y and Δ_z represents the width, length and height of a volume cell, respectively. The cut-off value is therefore in the same order magnitude as the mesh size. The mesh size is therefore clearly integrated into the LES filtering function. The mesh or grid resolution should consequently be large or fine enough for the length scales to accurately represent most flow features. The combined effect of fine mesh requirements and the inherently transient nature of LES makes this technique exceptionally expensive in terms of computational resources. It is possible for LES to approach direct numerical simulation (DNS), in which all scales are resolved, when the grid resolution becomes large enough. However, LES is less computationally expensive than DNS. Additionally, owing to SGS modelling, the smallest cell sizes can exceed the Kolmogorov length scales (η) and larger time steps can be used in the LES technique than that which must be applied in DNS. This allows LES to be applied in cases where the use of DNS is not feasible, for instance high Reynolds number flows and complex geometries (Ferziger and Perić, 2002; Hassan, 2008).

In the case of incompressible flow, the Navier-Stokes equation (Equation 2.12) can be filtered or space-averaged to arrive at the following equation (Ferziger and Perić, 2002; Hassan, 2008):

$$\frac{\partial(\rho \bar{u}_i)}{\partial t} + \frac{\partial\left(\rho \overline{u_i u_j}\right)}{\partial x_j} = -\frac{\partial \bar{P}}{\partial x_i} + \frac{\partial}{\partial x_j}\left[\mu\left(\frac{\partial \bar{u}_i}{\partial x_j} + \frac{\partial \bar{u}_j}{\partial x_i}\right)\right] \tag{2.29}$$

where the overbar indicates a space-filtered variable in each case. The computation of the $\overline{u_i u_j}$ term is a challenging task. The term is consequently decomposed and incorporated into the SGS Reynolds stress (τ_{ij}^{s}) approximation (Ferziger and Perić, 2002; Versteeg and Malalasekera, 2007; Hassan, 2008):

$$\tau_{ij}^{s} = \rho\left(\overline{u_i u_j} - \bar{u}_i \bar{u}_j\right) = \rho\left[\left(\overline{\bar{u}_i \bar{u}_j} - \bar{u}_i \bar{u}_j\right) + \overline{\bar{u}_i u_j{}'} + \overline{u_i{}' \bar{u}_j} + \overline{u_i{}' u_j{}'}\right] = L_{ij} + C_{ij} + R_{ij} \qquad (2.30)$$

where L_{ij} represents the Leonard stresses, C_{ij} the cross-stresses and R_{ij} the LES Reynolds stresses. Both Leonard stresses and cross-stress are associated with significant amounts of energy removal from resolved scales. The cross-stresses arise from interactions between the SGS and resolved eddies. Lastly, the LES Reynolds stresses result from convective momentum transfer that is caused by SGS eddy interactions. It is important to note that although Equation 2.30 is a common representation of the SGS Reynolds stress, other models or approximations have also been proposed depending on the SGS model. SGS models attempt to model SGS Reynolds stresses along with the SGS viscosity. The three SGS models that are currently implemented into STAR-CCM+® include the Smagorinsky model, the Dynamic Smagorinsky model, as well as the Wall-Adapting Local Eddy-Viscosity (WALE) model (Siemens PLM Software, 2017).

It was further noted that LES requires approximately double the amount of computational resources that RSM requires. Consequently, LES is not as widely validated and used as frequently as RANS turbulence models. However, the increased computational cost of LES yields information regarding resolved fluctuations in addition to characterising the mean flow. The resolved fluctuations provide considerably more detail on the flow field than typical RANS turbulence models. LES is also capable of accurately predicting highly complex flows with instabilities. In some instances, the qualitative detail on flow fields depicted by LES is comparable to that presented by physical experiments (Ferziger and Perić, 2002; Versteeg and Malalasekera, 2007).

2.3.2.2 Detached eddy simulation

The application of LES in CFD simulations is limited due to computational constraints. In contrast, RANS turbulence models are less expensive, nevertheless their accuracy is insufficient in certain cases. A hybrid RANS-LES approach such as detached eddy simulation (DES) provides a compromise between simulation accuracy and computational cost. DES therefore attempts to

combine the advantages of unsteady-RANS (uRANS) and LES (Siemens PLM Software, 2017; Holgate *et al*., 2018).

In general, DES utilises RANS turbulence models to model boundary layers and regions with irrotational flow. STAR-CCM+® incorporates the Spalart-Allmaras, the elliptic blending k-ε and the SST k-ω RANS turbulence models into DES. This is followed by integrating LES into unsteady, separated regions. Available DES model variants include delayed DES (DDES) and improved DDES (IDDES). The former induces a delay to prevent premature conversion of RANS to LES in attached boundaries or spatially refined regions, while the latter extends DDES to include wall-modelled LES (WMLES) capabilities to resolve difficulties in distinguishing between modelled and resolved log-law of the wall regions (Siemens PLM Software, 2017; Holgate *et al*., 2018).

It is estimated that for internal flows at high Reynolds numbers the computational cost of LES relative to uRANS is 10^4-10^5:1, while the ratio for DES to uRANS is 10^3:1. The results are remarkable and provide potential for decreasing computational cost without sacrificing too much accuracy. Nevertheless, DES cannot be considered as an all-inclusive turbulence modelling approach. Disadvantages in global domain applications include log-layer discrepancies, mesh induced separation, delays in forming instabilities, while local or zonal approaches occasionally require flow field knowledge prior to simulation attempts, along with the potential of additional difficulties arising at RANS-LES interfaces (Siemens PLM Software, 2017; Holgate *et al*., 2018).

2.3.3 Direct numerical simulation

Direct numerical simulation (DNS) is a transient simulation method which resolves all turbulent scales within the computational domain. DNS requires excessively high resolution meshes with sufficiently small time steps to capture the flow detail of the smallest eddies and fastest fluctuations. The computational domain should preferably represent the size of the actual physical domain or otherwise it should be large enough to capture the largest eddy. Additionally, the simulation should be able to completely resolve the kinetic energy dissipation. Therefore, it is recommended that the base cell size should not exceed that of the Kolmogorov length scales. Furthermore, it is recommended that the number of mesh elements should be in the order of $Re^{9/4}$. However, it is argued that dissipation principally takes place at larger length scales in the order of 5η to 15η. Hence, the bulk dissipation can be sufficiently characterised with smaller resolution meshes. DNS is the most accurate method in the numerical analysis of turbulent flow

and undoubtedly the most computationally expensive. The accuracy of DNS allows it to be used for benchmark studies, as a substitute to or validation for certain physical experiments and to provide detailed insight into various flow phenomena (Ferziger and Perić, 2002; Versteeg and Malalasekera, 2007).

The numerical analysis of turbulent flows can be summarised by means of the hierarchy in Figure 2-3.

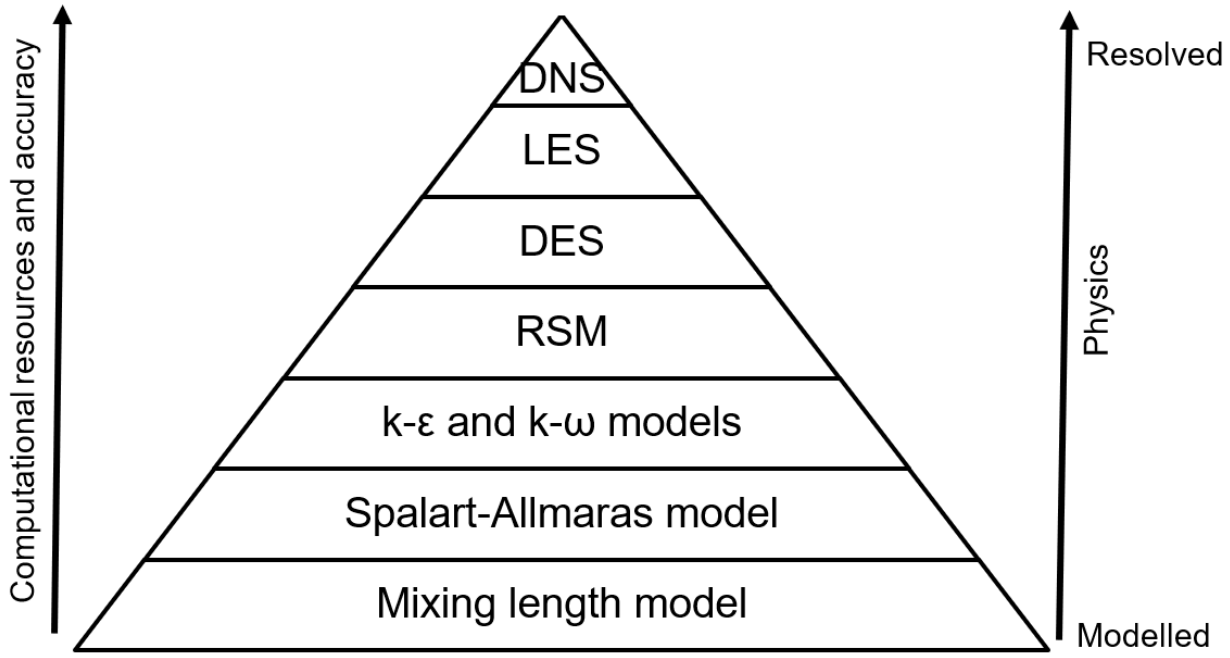

Figure 2-3: Hierarchy for the numerical analysis of turbulent flows (Adapted from Sagaut and Deck, 2009; Shams *et al*., 2014)

2.3.4 Wall treatment models

The concept of a turbulent boundary layer has been discussed in Section 2.2.4. Walls initiate vorticity which consequently demands an accurate representation of flow phenomena in the boundary layer. Figure 2-2 illustrates the regions associated with each sublayer. Three main types of wall treatment models are implemented into STAR-CCM+®, which include the low-y^+, high-y^+ and all-y^+ wall treatment models (Siemens PLM Software, 2017).

Firstly, low-y$^+$ wall treatment aims at resolving the viscous sublayer. Computational requirements make this approach mostly suitable for flows at low Reynolds numbers. Additionally, sufficient mesh resolution is required for near-wall cell centroids to have y^+ values of approximately one, and in some cases, up to five. In contrast, high-y$^+$ wall treatment utilises wall functions to model near-wall effects. This wall treatment option requires less computational resources and is suitable for near-wall cell centroids with y^+ values exceeding 30. Lastly, the all-y$^+$ wall treatment option uses a hybrid approach wherein the appropriate wall treatment method, low-y$^+$ or high-y$^+$, is selected depending on the mesh resolution. This hybrid approach is recommended when near-wall cell centroids are in the buffer layer: $1 < y^+ < 30$ (Siemens PLM Software, 2017).

2.4 Summary

This chapter first investigated the theory associated with the relevant fluid mechanics such as the conservation equations of fluid flow, the Navier-Stokes equations, as well as flow regimes and the concept of velocity boundary layers.

Secondly, the Reynolds averaging process along with popular turbulence models and scale-resolving simulations were discussed, which was concluded with a hierarchy of the numerical approaches to analyse turbulent flow. Lastly, a brief overview was given on the core wall treatment options that are available in STAR-CCM+®.

CHAPTER 3: LITERATURE OVERVIEW

3.1 Introduction

This chapter will provide a literature overview on packed beds that includes their structural characterisation and thermohydraulic behaviour. The role of numerical modelling in the analysis of fluid flow and heat transfer through packed beds will be highlighted through reviews. Lastly, the experimental configuration of the Braiding Effect Test Section (BETS) experiments will be discussed along with related CFD studies.

3.2 Packed beds

The industrial applications of packed beds include, among others, thermal energy storage, separation units and heterogeneous catalytic reactors (Wen and Ding, 2006; Caulkin *et al*., 2007; Incropera *et al*., 2013). The widespread application of packed beds is attributed to their high surface area to volume ratios (Caulkin *et al*., 2007). A considerable amount of research has been done on the thermal-hydraulic behaviour of packed beds in the last few decades (Achenbach, 1995; Rousseau and Van Staden, 2008). The accurate characterisation of thermal-hydraulic behaviour in packed beds is essential for their optimal and safe design, as well as operation (Logtenberg and Dixon, 1998; Nijemeisland and Dixon, 2004).

Flow and heat transfer related measurements in packed beds are challenging and may also disrupt the flow field. CFD analysis can prove useful in overcoming the limitations of measuring instruments and subsequently give an accurate and detailed representation of the flow field and heat transfer in packed beds (Logtenberg and Dixon, 1998; Dixon and Nijemeisland, 2001).

The exploration of heat transfer mechanisms in packed beds and more specifically, the evaluation of the effective thermal conductivity, can be greatly facilitated by the incorporation of the packing structure (Cheng *et al.*, 1999). Voidage or porosity variations in packed beds can greatly affect heat and mass transfer parameters, since the associated parameters are all influenced by the packing structure (Caulkin *et al*., 2007). In the case of structured packings, it can also be concluded that the effects from the packing formation, as well as particle shape have a significant influence on the thermal-hydraulic behaviour (Yang *et al*., 2010). Consequently, structural characterisation is crucial in the analysis of packed bed performance.

3.2.1 Structural characterisation

It was emphasized that the packing structure is important in the investigation of thermal-hydraulic behaviour in packed beds. We will restrict our attention to packings which contain mono-sized, spherical particles. The structure is usually characterised by means of porosity, while less common methods of characterisation include the coordination number and the contact angles formed between adjacent spherical particles (Du Toit *et al*., 2009). Additionally, ordered or structured packings are commonly organised into well-known lattice packing types (Yang *et al*., 2010; Preller, 2011; Li *et al*., 2012; Li *et al*., 2017). Although beyond discussion, packings can also be represented by Voronoi or Delaunay tessellations (Cheng *et al.*, 1999, Wu *et al*., 2017).

Packing structures are usually characterised by porosity alone (Du Toit *et al*., 2009). The bulk porosity (ε_b) of a packed bed is defined as follows (Achenbach, 1999; Fogler, 2014; Van der Merwe, 2014):

$$\varepsilon_b = \frac{V_v}{V_t} = 1 - \frac{V_s}{V_t} \tag{3.1}$$

where V_v is the void volume (m^3), V_s is the volume occupied by the solid particles (m^3) and V_t is the total internal volume of the packed bed (m^3). Porosity is known to fluctuate both radially and axially (Du Toit *et al*., 2009). We shall only consider the radial variation in porosity. A typical representation of the radial porosity distribution in the near wall region of a randomly packed bed is given in Figure 3-1. The distribution is based on the distance from the wall, measured in spherical or pebble diameters (d_p).

Packing structures are disrupted by walls, consequently resulting in large fluctuations in the radial porosity. The oscillatory behaviour of the radial porosity typically appears to dampen out at five spherical diameters as the bulk region of the bed is approached (Du Toit *et al*., 2009, Van Antwerpen, 2009). Figure 3-2 distinguishes between the wall and bulk regions of a randomly packed bed based on the distance from the wall.

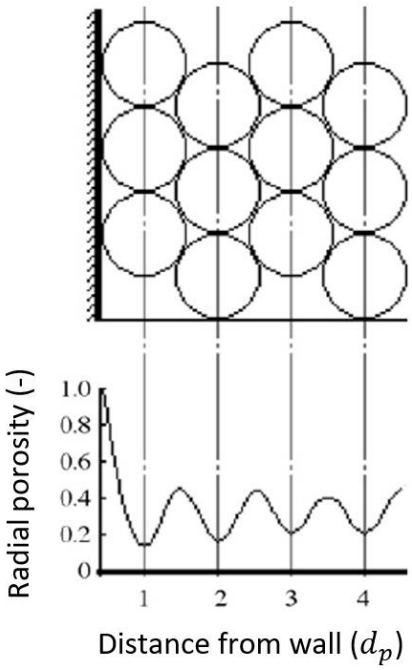

Figure 3-1: Near wall radial porosity distribution (Adapted from Caulkin *et al*., 2007)

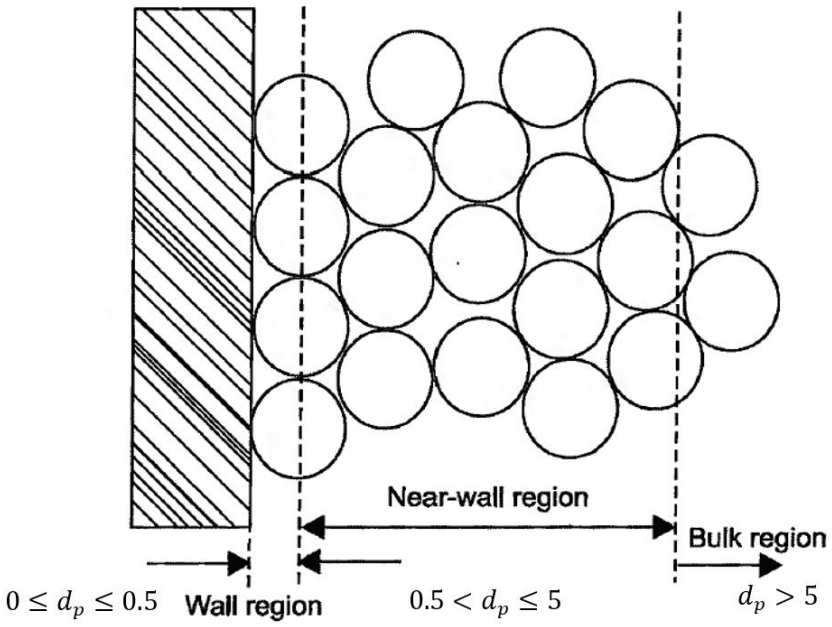

Figure 3-2: Regions within a randomly packed bed (Adapted from Van Antwerpen, 2009)

Furthermore, in the case of randomly packed cylindrical beds, the aspect ratio (α) is used to describe the diameter ratio between the cylinder (D) and the mono-sized spheres (d_p). The aspect

ratio is an important structural characterisation parameter and has a direct relation to both the porosity and global packing structure (Van der Merwe, 2014).

The coordination or kissing number is another useful parameter in the structural characterisation of packed beds. The coordination number (N) is defined as the number of contacting spheres situated around a specific sphere. Additionally, the number is seen as a microscopic characterisation parameter, whereas porosity is associated with the macroscopic level. The importance of coordination numbers in packed beds arises in the analysis of permeability, thermal conduction, reactions between adjacent solid particles, as well as tensile strength (Du Toit *et al*., 2009; Cheng *et al*., 2013).

Following the coordination number, the contact angle also serves as a structural characterisation parameter and is used specifically in the evaluation of effective thermal conductivity. Subsequently, with reference to Figure 3-3, the contact angle (ϕ_c) between two contacting spheres refers to the angle between the centroid connecting line and the line perpendicular to the direction of the heat flux (Q). The contact angle can be correlated to the thermal resistance between two contacting spheres. Subsequently, a contact angle of 0° or less indicates that sphere B has no influence on the overall heat transfer between spheres A and B, whereas the maximum amount of influence occurs at an angle of 90°. Lastly, the sum of the two angles, φ and ϕ_c, always equate to 90° (Du Toit *et al*., 2009).

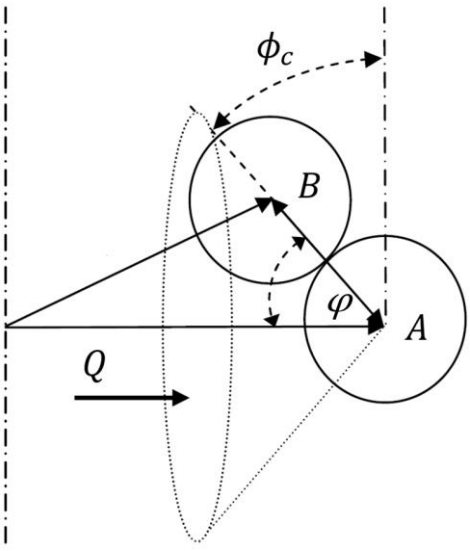

Figure 3-3: Contact angle between two spheres (Adapted from Du Toit *et al*., 2009)

Structured packings can be organised to correspond to the well-known crystal lattice structures. The basic lattice structures that were used by Yang *et al*. (2010), Li *et al*. (2012) and Li *et al*. (2017) in their CFD simulations are represented by Figure 3-4.

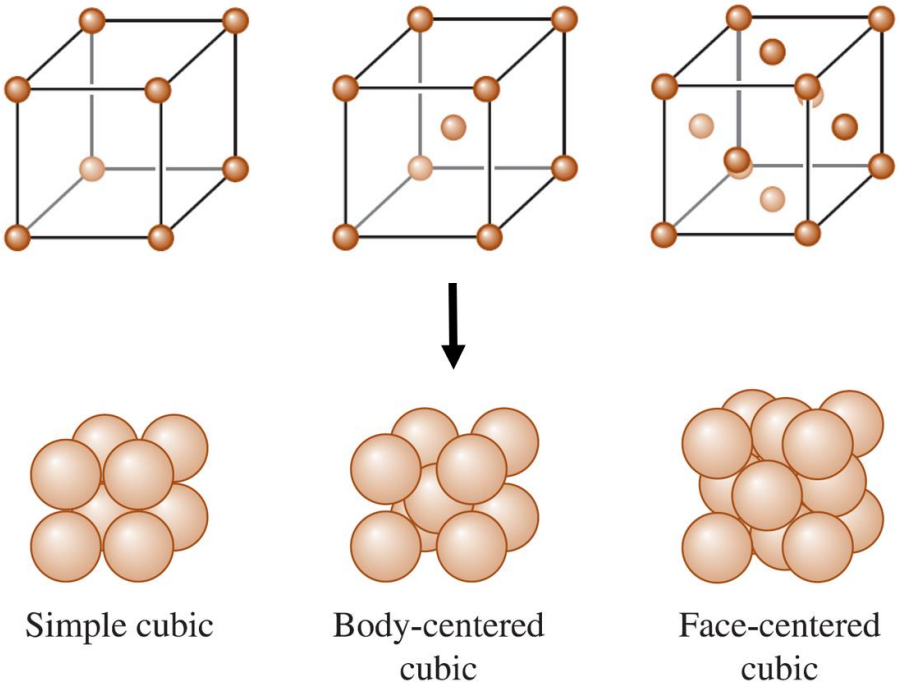

Figure 3-4: Cubic lattice structures (Adapted from Askeland and Fulay, 2009)

The simple cubic (SC), body-centred cubic (BCC) and face-centred cubic (FCC) lattice structures generally have bulk porosities of 0.48, 0.32 and 0.26, respectively. In this case (Figure 3-4), the FCC presents a cubic close-packing (CCP) and has the densest packing structure between the three cubic lattice structures. Additionally, the SC, BCC and FCC lattice structures have coordination numbers of 6, 8 and 12, respectively (Preller, 2011).

Structured packings are however not limited to the common crystal lattice arrangements. For instance, Duan *et al*. (2014) simulated two structured packings containing six spheres per layer. In their first model, each successive layer of spheres was placed directly on top of the former layer, while in their second model each successive layer was placed in the interstitial voids formed by the former layer, which resulted in two repeating layers.

3.2.2 Thermal-hydraulic behaviour

3.2.2.1 Fluid flow

The flow or more specifically the velocity distribution through a packed bed is principally influenced by the packing structure, including the length of the bed, as well as the Reynolds number (Reyneke, 2009; Preller, 2011).

As stated earlier, porosity is a macroscopic packed bed structural characterisation parameter which is commonly used in the absence of other structural related parameters. The velocity profile is therefore frequently correlated with the radial porosity distribution. Eppinger *et al*. (2011) investigated the influence of the radial porosity distribution on the velocity profile in packed beds at different particle Reynolds numbers (Re_p), as well as at different aspect ratios ($\alpha = D/d_p$). From the results (Figure 3-5), it is evident that the velocity profiles almost replicate the oscillatory behaviour of the radial porosity in all cases due to the remarkable structural influence of the wall. Nevertheless, the velocity and porosity distributions are expected to become more damped and therefore flat for aspect ratios larger than 10 (Delgado, 2006).

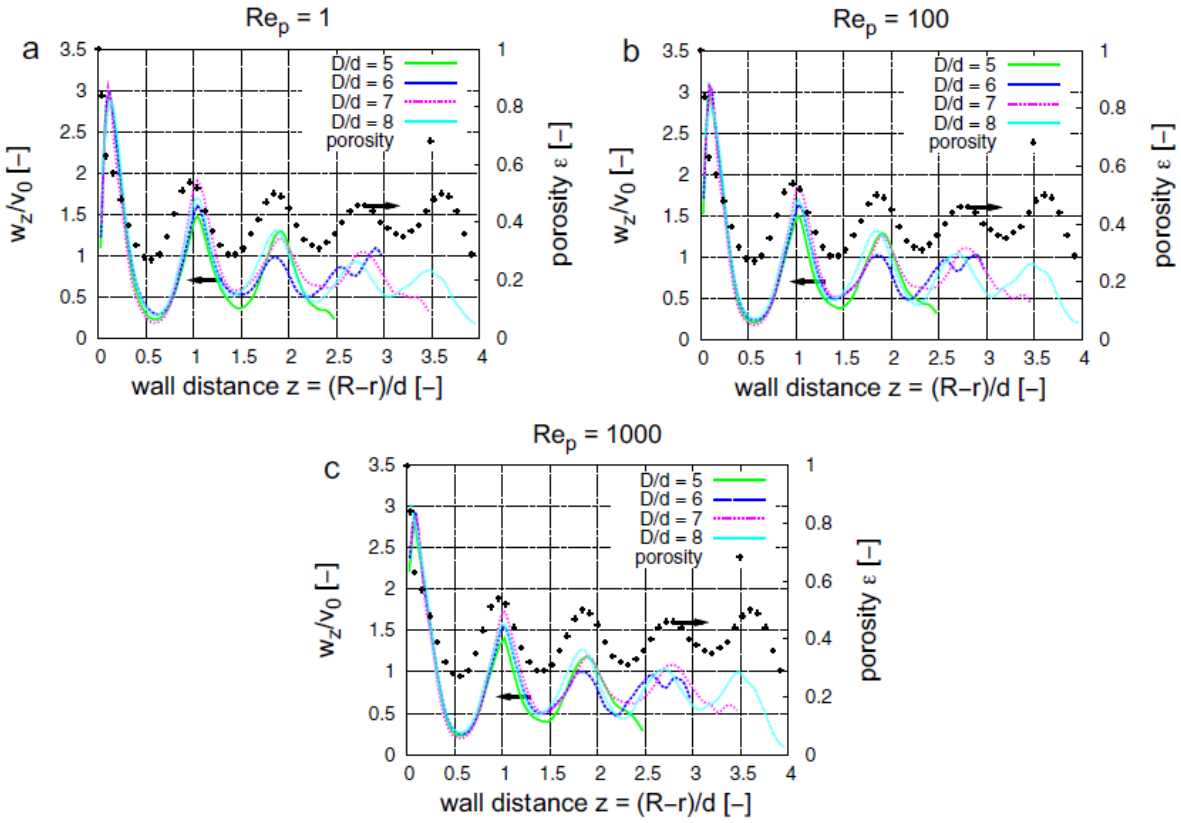

Figure 3-5: Comparison between the velocity and radial porosity distribution for different particle Reynolds numbers and aspect ratios (Eppinger *et al*., 2011)

The velocity in the wall region approaches a maximum value due to the enhanced permeability near the wall where the porosity virtually reaches unity. The high porosity results from the structural influence of the wall. This enhanced permeability near the wall of a packed is known as wall channelling (Reyneke, 2009).

The simulations by Eppinger *et al.* (2011) were conducted at different particle Reynolds numbers (Figure 3-5). These types of Reynolds numbers are commonly used in the analysis of fluid flows through packed beds. The particle Reynolds number (Re_p) for equally sized spheres is defined as (Eppinger *et al*., 2011; Fogler, 2014):

$$Re_p = \frac{\rho u_0 d_p}{\mu} = \frac{u_0 d_p}{\nu} \tag{3.2}$$

where u_0 the superficial fluid velocity (m/s) which is obtained by dividing the volumetric flow rate by the total cross-sectional area (solids and voids) of the packed bed. Eppinger *et al*. (2011) considered a Re_p of 1, 100 and 1000 to correspond to laminar, transitional and turbulent flow, respectively. However, the correspondence between flow regimes and particle Reynolds numbers in packed beds has been found to differ. In the review by Hlushkou and Tallarek (2006), it was noted that flows below a Re_p of 2 correspond to Darcy's law, which precedes the onset of laminar flow, while transitional flow generally commences between a Re_p of 90 to 150. Furthermore, turbulent flows have been encountered as early as at a Re_p of 300.

The influence of the packed bed length (L) on the velocity distribution has been found to be negligible for L to d_p ratios larger than 9 (Reyneke, 2009; Preller, 2011). Additionally, in CFD applications the length of the domain preceding and following the packed region is usually extended to reduce the influence of inlet and outlet boundary conditions on the flow field (Reyneke, 2009; Yang *et al*., 2010; Eppinger *et al*., 2011; Preller, 2011; Theron, 2011; Shams *et al*., 2014; Van der Merwe 2014). For instance, Eppinger *et al*. (2011) extruded the inlet and outlet lengths by $3d_p$ and $10d_p$, respectively. Lastly, when modelling longitudinal dispersion, the length of the packed bed is typically chosen to sufficiently represent a semi-infinite packed bed by ensuring that the L/D ratio is greater than 20 (Delgado, 2006).

3.2.2.2 Pressure drop

The performance of a packed bed is greatly influenced by the pressure drop over the bed. The pressure drop is usually modelled by extending the Darcy-Weisbach equation for pressure drop in pipe flows to the application of packed beds (Du Toit and Rousseau, 2014):

$$\Delta P = \psi \left(\frac{L}{d_p}\right)\left(\frac{1-\overline{\varepsilon}}{\overline{\varepsilon}^3}\right)\left(\frac{\rho {u_0}^2}{2}\right) \tag{3.3}$$

where ΔP is the pressure drop over the packed bed (Pa), ψ is the friction factor (-) and $\overline{\varepsilon}$ is the average porosity of the bed (-). The friction factor is usually correlated to the modified Reynolds number (Re_m), which is equal to $Re_p/(1-\overline{\varepsilon})$. The relationship between the friction factor and the modified Reynolds number for various packed beds is illustrated in Figure 3-6.

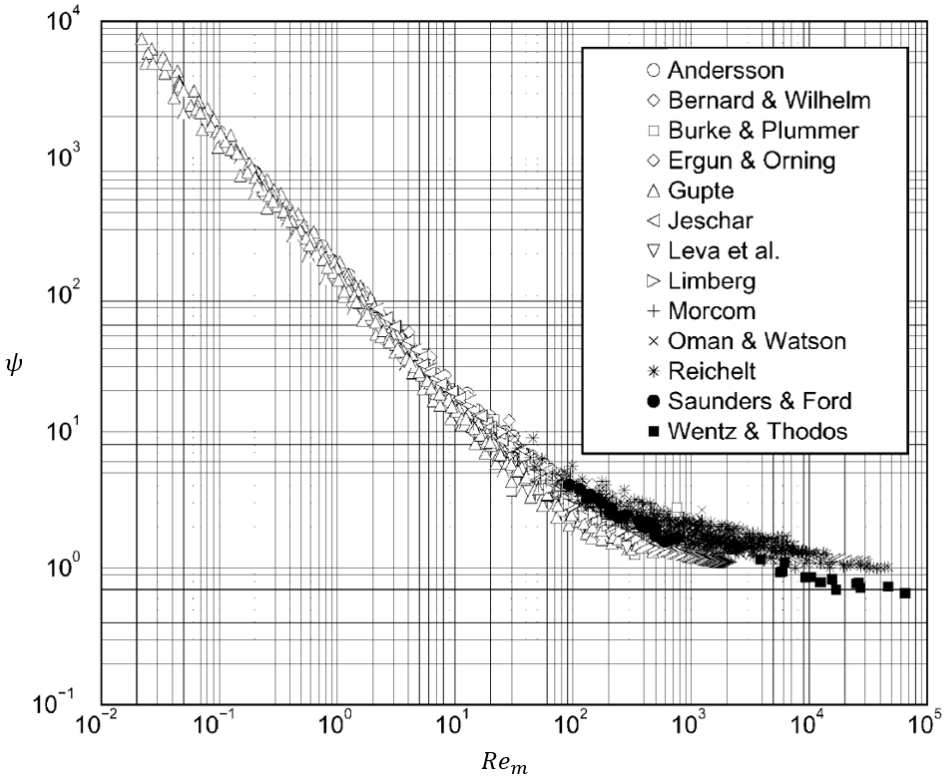

Figure 3-6: Comparison between the friction factor and modified Reynolds number of packed beds (Adapted from Eisfeld and Schnitzlein, 2001)

The pressure drop over a packed bed is influenced by both the wall friction and the increased porosity in the near wall region. Their influences are contrasting, since the wall friction increases

the pressure drop, while the high porosity decreases it. The dominance of each effect is dependent on the flow regime, with the influence of wall friction being significant in lower Reynolds number flow regimes and the effect of porosity being dominant in the higher Reynolds number regimes (Kang, 2010). Additionally, Du Toit and Rousseau (2014) observed that inertial effects become dominant at a Re_m greater than 300. Consequently, the average porosity becomes insufficient in solely characterising the porous structure. It was also determined that structured packed beds have considerably lower friction factors than randomly packed beds.

3.2.2.3 Heat transfer

In addition to pressure drop, heat transfer in packed beds is also essential to determining their performance (Wen and Ding, 2006). Heat transfer in packed beds is mainly characterised by forced convection and effective thermal conductivity (Achenbach, 1995; Demirel *et al*., 2000).

The forced convection in a packed bed is influenced by many parameters, including Re, Pr (Prandtl number), $\overline{\varepsilon}$, α and L/D. Other influential phenomena include local flow conditions, thermal radiation, thermal conduction between solids, natural convection, as well as surface roughness. The Nusselt number (Nu) is commonly used to describe these phenomena. Nu is generally correlated to Re_p and Pr (Achenbach, 1995; Demirel *et* al., 2000; Wen and Ding, 2006; Yang *et al*., 2010). Nu is a dimensionless heat transfer parameter which describes the ratio of convection to thermal conduction, while Pr is defined as the ratio of the momentum to the thermal diffusivities (Incropera *et al*., 2013).

The effective thermal conductivity is an important heat transfer parameter that can be used to model temperature distributions within a packed bed. We will restrict our attention to the effective radial thermal conductivity (k_e), which can be modelled as (Bauer and Schlünder, 1978a):

$$\frac{k_e}{k_f} = \left(\frac{k_e}{k_f}\right)_{\substack{conduction,\\ radiation}} + \left(\frac{k_e}{k_f}\right)_{convection} \tag{3.4}$$

where k_f is the thermal conductivity of the gas (W/m·K). The first term is related to thermal conduction and radiation processes, while the second term is associated with the convective lateral mixing or the radial thermal dispersion of the flow. Additional information regarding the

former term can be found in Bauer and Schlünder (1978b). The latter term is influenced by several parameters, such as $\overline{\varepsilon}$, α, Re_p and Pr. Furthermore, the convection term is related to the Péclet number (Pe) as follow (Bauer and Schlünder, 1978a; Achenbach, 1995):

$$\left(\frac{k_e}{k_f}\right)_{convection} = \frac{Pe}{K} \tag{3.5}$$

where K is a constant which can be determined from the aspect ratio (α) of the packed bed. Subsequently, Pe ascribes to the ratio of the rate of advection to that of thermal conduction, resulting in $Pe = Re_p Pr$ (Achenbach, 1995; Incropera *et al*., 2013). Lastly, the convection term is commonly correlated to Re_p (Demirel *et al*., 2000; Wen and Ding, 2006).

3.2.3 Numerical modelling of packed beds

3.2.3.1 Implicit modelling

Packed beds can be modelled numerically by using either an implicit or explicit approach. Implicit modelling refers to pseudo-homogeneous or empirical methods in which the packing is treated as a homogeneous porous structure, thereby neglecting the pore structure. Consequently, this method cannot provide detailed information on interstitial flow behaviour and numerical accuracy is dependent on experimental data (Nijemeisland and Dixon, 2004; Theron, 2011; Wu *et al*., 2018).

Nevertheless, empirical methods are still used extensively in the numerical analysis of packed beds. There exist various correlations which separately quantify the axial and radial porosity distributions. The average coordination number can subsequently be correlated to the porosity (Van Antwerpen, 2009; Du Toit *et al*., 2009). Additionally, much work has been done on correlating the friction factors with the average porosity and particle or modified Reynolds number (Figure 3-6). The friction factor correlations are usually either of the Carman or Ergun form, although other forms do exist (Eisfeld and Schnitzlein, 2001; Kang, 2010). The friction factor can subsequently be used to determine the pressure drop over packed beds with the aid of equations such as the modified Darcy-Weisbach equation (Equation 3.3) (Du Toit and Rousseau, 2014). With regards to heat transfer, several correlations have been formed to describe the effective wall heat transfer coefficient or Nusselt number, typically in terms of the particle Reynolds number and

Prandtl number. Similarly, relationships have also been derived to describe the effective radial thermal conductivity (Wen and Ding, 2006; Wu *et al*., 2017).

3.2.3.2 Explicit modelling

Interstitial fluid flow or explicit modelling methods incorporate the exact packing structure, resulting in each pebble being modelled separately. CFD analysis can provide an accurate and detailed representation of the thermal-hydraulic packed bed behaviour without disrupting the flow field. CFD simulations can replicate experimental data and provide additional data and detail not acquirable by any other means (Logtenberg and Dixon, 1998; Dixon and Nijemeisland, 2001; Nijemeisland and Dixon, 2004; Theron, 2011; Shams *et al*., 2014; Wu *et al*., 2018). A brief overview will be given on the thermal-hydraulic behaviour of packed beds by reviewing a few selected CFD studies.

Dixon and Nijemeisland (2001) simulated low Reynolds number flow ($Re_p = 180$) in a cylindrical randomly packed bed with an aspect ratio of 4. The authors noted that the number of pebbles increased considerably with an increasing aspect ratio. Consequently, translational periodic boundary conditions were imposed on the inlet and outlet of the flow domain to reduce the mesh size. These boundary conditions were justified due to an axially repeating packing structure. Although, the flow was laminar and isothermal, it still exhibited a tortuous nature, along with wall channelling and reverse flow as displayed in Figure 3-7. The first contour is associated with velocity vectors and displays velocity magnitude (m/s), while the second relates to interstitial streamlines with axial velocity (m/s).

In a subsequent study, Nijemeisland and Dixon (2004) used the same bed ($\alpha = 4$) with a refined grid to simulate fluid flow and wall heat transfer at a Re_p of 1000. The authors have experienced that the number of control volumes or volumetric cells increased exponentially for an increasing aspect ratio, while increasing linearly with increasing bed length. It was estimated the mesh required to simulate the full packed bed geometry with sufficient accuracy and detail would contain 600 million cells. Consequently, similar to the previous study, axially imposed translational periodic boundary conditions were required. The implementation of the periodic boundaries resulted in a bed with six axial layers, 72 pebbles and a mesh that contained 47 million cells. This was followed by using a fine graded or regionally refined mesh for an additional reduction to 6 million cells. A coarser graded mesh was developed which contained 1.97 million cells. A final

reduction was made on the fine graded mesh by simulating only a third of the cross-sectional area (120°). This was done by imposing symmetry boundary conditions on each of segment's walls, which resulted in a mesh that contained 0.76 million cells.

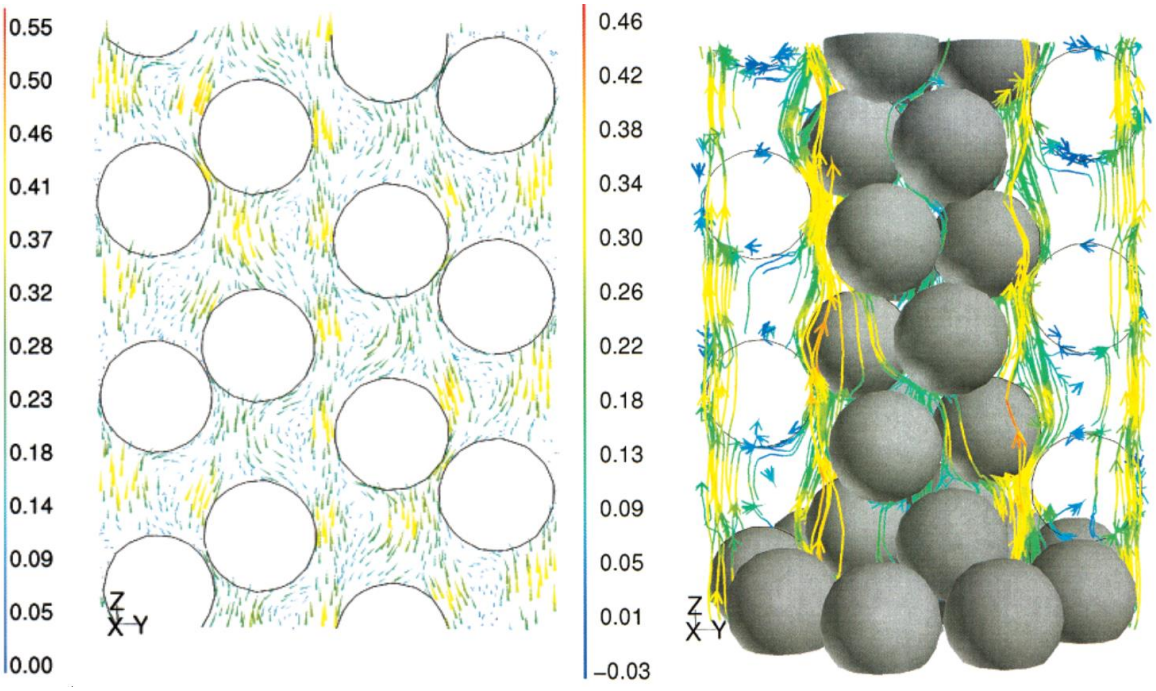

Figure 3-7: Contour plots of velocity vectors and streamlines (Adapted from Dixon and Nijemeisland, 2001)

The performance of the full cross-sectional model was subsequently compared with that of the segmented model. The same flow results were obtained for both models. The authors reasoned that segmented models are good representations of the full cross-sectional model when investigating near wall phenomena. In addition, conceptual analysis concluded that the local heat transfer rates do not correlate well with local flow fields, nonetheless they are more related to large-scale flow patterns.

Shams *et al.* (2014) conducted a detailed CFD study in STAR-CCM+® on a rectangular randomly packed bed with 30 pebbles and an average porosity of 0.4. Periodic boundary conditions were imposed on all four walls. Furthermore, the estimated particle Reynolds number, based on the maximum predicted velocity, was nearly 9750. The mesh consisted of polyhedral and prismatic layer cells, resulting in a total number of 18 million cells. The mesh resolution had to be sufficiently high to provide highly resolved LES simulations. However, the extended outlet domain contained

a coarser grid to reduce the probability of reverse flow. The y^+ values on the pebbles were below 0.3 and 0.5 for the low and high wall shear stress regions, respectively. The WALE SGS model was used in all simulations. The results obtained from the highly resolved LES simulations were in good agreement with a reference quasi-DNS (q-DNS) simulation. The dimensionless temperature distributions over pebbles in the bulk region are displayed in Figure 3-8. The first and second iso-contours represent the instantaneous and time-averaged temperature distributions, respectively. Large temperature gradients are displayed over each pebble and hot-spots appear in low velocity regions. The latter was found to be unsteady due to the rapid variation of the flow in all directions.

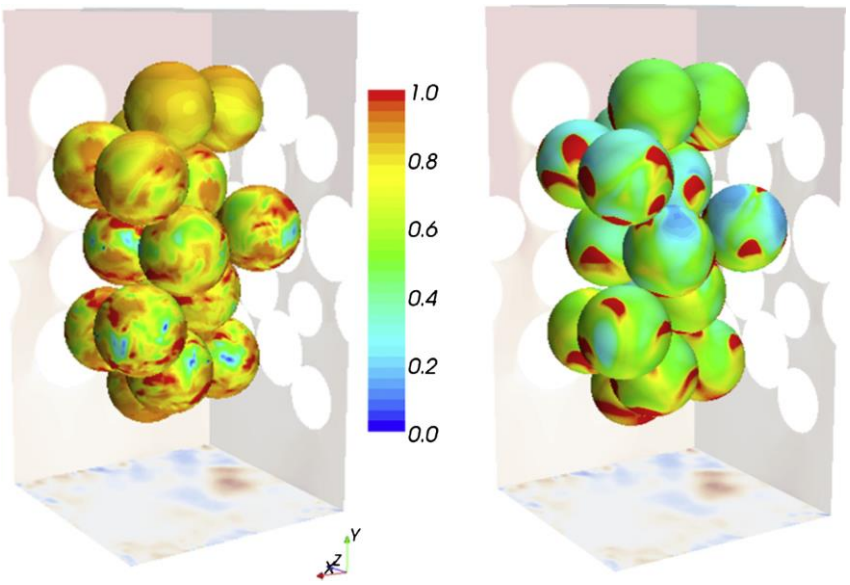

Figure 3-8: Iso-contours of dimensionless pebble temperature distributions (Shams *et al*., 2014)

Hassan (2008) simulated a rectangular BCC structured packed bed at a Reynolds number of 800 000, based on the effective diameter of the bed. The packing contained 24 pebbles and symmetry boundary conditions were imposed on all the walls, while translational periodic conditions were specified at the inlet. The geometry was meshed with tetrahedral volume cells with a minimum to maximum cell size ratio of 1/6, which resulted in a mesh that contained approximately 330 000 cells. RANS models are generally unsuitable for simulating flow through multiple alternating contiguous concave and convex curvatures. Centrifugal forces supress turbulence on convex surfaces, whereas turbulence is intensified on concave surfaces. Additionally, boundary layers are greatly affected by pressure gradients in these flow types. Consequently, LES was used with the Smagorinsky SGS model. The Smagorinsky constant (C_s)

was increased from 0.1 to 0.18, which was previously determined to be more suitable for cross flow. Separated and oscillatory flows were identified in the gaps between the pebbles. These phenomena were accompanied by large velocity gradients. Furthermore, large opposing vorticity spin pairs were detected in several gaps between the pebbles (Figure 3-9). Positive vorticity denotes anticlockwise flow spins, while negative vorticity is indicative of clockwise spins. Additional observations included rapid creation and destruction of eddies between pebbles and that the number and size of vortices increase with increasing pore size and velocity.

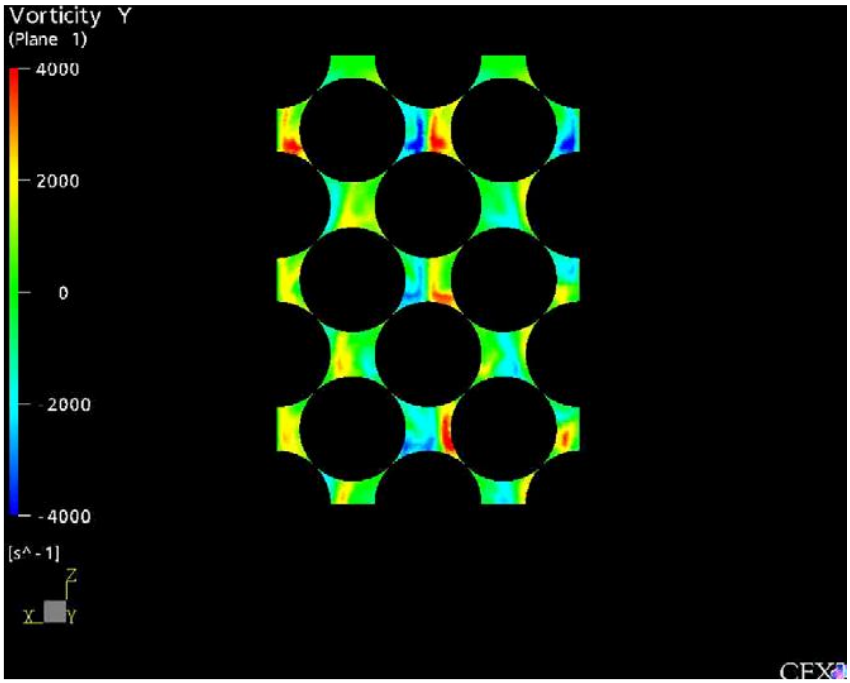

Figure 3-9: Vorticity contour plot (Hassan, 2008)

Yang *et al*. (2010) investigated forced convective heat transfer in SC, BCC and FCC structured packings due to their potentially reduced pressure drops and improved overall heat transfer over randomly packed beds. The physical model was composed of more than 1000 particles that were stacked in channels (SC configuration). In order to reduce the computational requirements, only one representative channel was selected by imposing symmetry boundary conditions on all four walls surrounding the axial direction. The packing configurations were altered to arrive at the representative channels shown in Figure 3-10.

The porosity for the SC, BCC and FCC packings was 0.49, 0.34 and 0.28, respectively. This is similar to the usual bulk porosities for these packings (Section 3.2.1). These geometries were

meshed with tetrahedral volume cells. The SC, BCC and FCC beds were respectively meshed with 0.63, 1.26 and 2.31 million cells.

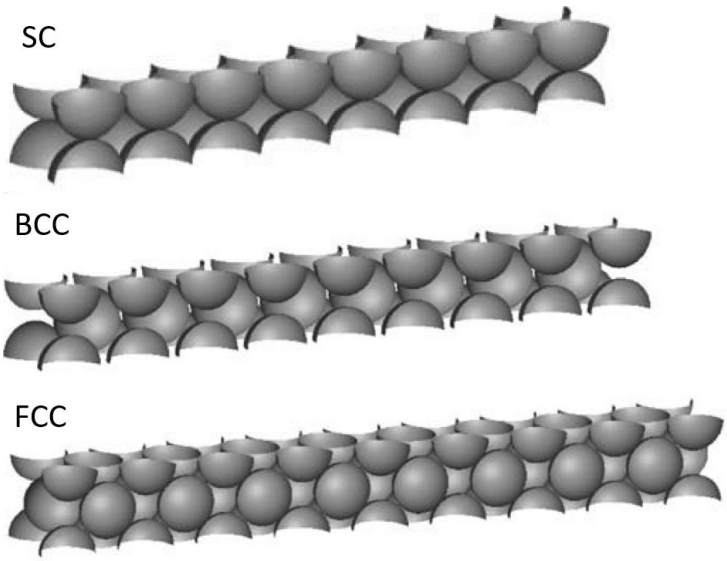

Figure 3-10: Structured packed channels (Adapted from Yang *et al*., 2010)

The pressure drop (ΔP), heat transfer coefficient (h) and overall heat transfer efficiency (γ) of these beds were subsequently compared, with $\gamma = h/\Delta P$. ΔP was found to increase with increasing Re_m, with the largest ΔP corresponding to the FCC packing and the smallest ΔP corresponding to the SC packing over all Re_m. The authors attributed the results to the higher fluid velocities that occurred in the FCC packing under the same Re_m, further owing to the smaller vortices within in the flow field, as well as reduced vortex formation. In addition, the reduction in vortex phenomena resulted from the high structural density or low porosity of the FCC packing. Furthermore, changes in Re_m resulted in friction factor (ψ) variations similar to that depicted in Figure 3-6. For $Re_m < 30$, ψ was the largest for the FCC packing and smallest for the BCC packing, while the ψ curves of the different packings started to deviate when $Re_m > 30$. Furthermore, for $30 < Re_m \leq 500$, ψ was the largest for the SC packing, while it remained the smallest for the BCC packing. Nevertheless, for $Re_m > 500$, ψ continued to be the largest for the SC packing, whereas the smallest ψ corresponded to the FCC packing. The ψ curves approached constant values at $Re_m > 3000$. The Ergun friction factor correlation was used to produce ΔP and ψ results that implicitly represented the behaviour of three randomly packed beds. Each implicitly modelled, random packed bed featured unique structural characteristics that corresponded to that of the individual structured packings. Therefore, in other words, a randomly packed bed was implicitly generated for each structured packed bed. The authors subsequently determined that

the random packings exhibited much larger ΔP and ψ values in comparison to structured packings, which resulted from the larger tortuosities of the random packed beds. Tortuosity ascribes to the ratio between the actual distance that a fluid packet travels and the shortest distance it would have travelled if there were no obstructions (Fogler, 2014).

The Nu ($h \propto Nu$) and γ of the sphere to fluid was subsequently evaluated for each packed channel. In a comparison between the structured packings, it was determined that the FCC packing had the largest Nu, whereas the SC packing had the smallest Nu over the entire range of Re_m. The large Nu of the FCC packing was caused by its high packing density that resulted in an increased amount of surface area available for heat transfer. Similar to the manner in which the Ergun friction factor correlation was used to predict ΔP and ψ results for the randomly packed beds, the Wakao correlation was used to implicitly predict Nu results for the previously configured randomly packed beds. The randomly packed beds subsequently displayed larger Nu values over all Re_m in comparison to the structured packed beds. In additional investigations, γ was found to decrease with increasing Re_m. In a comparison between the structured packings, the SC packing had the largest γ, while the FCC packing had the lowest γ over all Re_m, owing to the large ΔP of the FCC packing. This was followed by implicitly generating γ values for the randomly packed beds by using both the Ergun and Wakao correlations. The randomly packed bed, which structural characteristics pertained to the SC packing, displayed increased γ values over the entire range of Re_m when compared with the structured SC packing. However, in the case of the BCC and FCC packings, both corresponding randomly packed beds showed decreased γ values for $Re_m > 100$ in comparison to the structured packed beds.

Symmetry or periodic boundary conditions are usually imposed on the domain to obtain a simplified representation of the physical geometry for the sake of reducing the required computational resources. It is very uncommon to find literature wherein full CFD simulations were conducted to investigate the large-scale flow and heat transfer phenomena in packed beds. Wu *et al*. (2017) coupled CFD with a discrete element method (DEM) to investigate the heat transfer in large packed beds. This was facilitated by Voronoi tessellations and low resolution structured meshes which could accommodate packings with up to 27 000 spheres. The numerical results were in good agreement with those obtained by means of purely empirical codes.

3.3 Braiding Effect Test Section

It is reasoned that heat transfer mechanisms in packed beds are not fully understood and that research on thermal dispersion gave rise to correlations with considerable amounts of empiricism. The empiricism resulted from only incorporating a limited number of heat transfer mechanisms and from including insufficient complexity in structural characterisations. Consequently, these correlations have limited applicability and on occasion, uncertain validity (Cheng *et al.*, 1999; Wen and Ding, 2006; Rousseau and Van Staden, 2008; Van Antwerpen, 2009).

The High Pressure Test Unit (HPTU), which formed part of the Heat Transfer Test Facility (HTTF), was subsequently constructed to conduct a series of separate effects tests in order to validate existing thermohydraulic correlations. A detailed description of the HPTU plant layout can be found in Rousseau and Van Staden (2008). These separate effects tests included the BETS experiments which investigated the increased radial thermal dispersion or enhanced lateral mixing. The enhanced mixing or thermal diffusion effects are produced by the influence of the porous structure on the flow through packed beds, a phenomenon known as the braiding effect (Rousseau and Van Staden, 2008; Kgame, 2010).

Previous studies have attempted to quantify the increased thermal dispersion that was observed in the BETS experiments by numerically simulating the radial temperature profiles (Preller, 2011; Du Toit *et al*., 2012b) and by evaluating the fluid effective radial thermal conductivity (Kgame, 2010; Preller, 2011; Du Toit *et al*., 2012a; Du Toit *et al*., 2014).

3.3.1 Experimental configuration

The BETS experiments were conducted with rectangular, diagonally packed, A-B-C BCC structured packings. These packings were formed by attaching uniformly sized, clear and translucent acrylic spheres to cables, without allowing any contact between the spheres. The flow resistance initiated by the cables was considered to be insignificant with respect to that of the pebbles since the flow was directed parallel to the cables. Additionally, the spheres displayed extremely low emissivity and thermal conductivity to substantially reduce the amount of heat transfer through the spheres and between their surfaces. The first three axial layers of spheres were repeated 10 times, which resulted in 30 axial layers of spheres (Figure 3-11). The axial distance between these layers could be altered to obtain three different pseudo-homogeneous

porosities of 0.36, 0.39 and 0.45. We will restrict our attention to the lowest porosity, hereinafter referred to as BETS 0.36. In addition to utilising structured packings, the effect of porosity was further isolated by specifically manufacturing pebbles in the wall regions to maintain the desired homogeneous porosity throughout the test section. This considerably reduced the rapid increase in porosity in the near wall region (Figure 3-1) and presumably eliminated wall channelling (Rousseau and Van Staden, 2008; Kgame, 2010).

In order to investigate the braiding effect, braiding (hot nitrogen) gas was introduced just below the first layer of spheres through an inlet pipe in the centre of the annulus (Figure 3-12). The braiding gas was joined by the combined, fully developed flow from 16 cold nitrogen gas streams, which flowed through the annulus, with four lateral inlets located in each side of the packing containment at the equal axial distances. A constant block-shaped velocity profile was therefore distributed to the packing configuration (Rousseau and Van Staden, 2008; Kgame, 2010). A summary of the dimensions referred to in Figure 3-11 and Figure 3-12 (b) is given in Table 3.1.

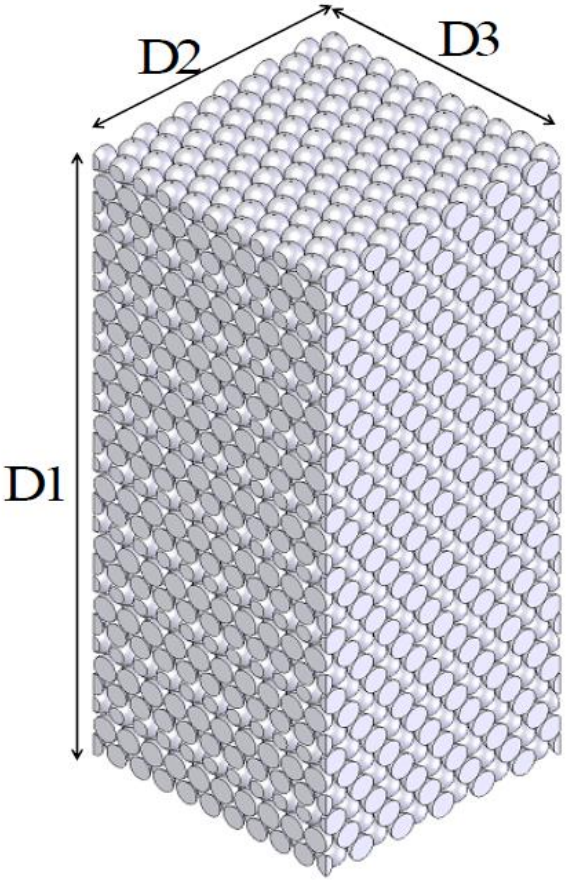

Figure 3-11: BETS 0.36 BCC packing configuration (Kgame, 2010)

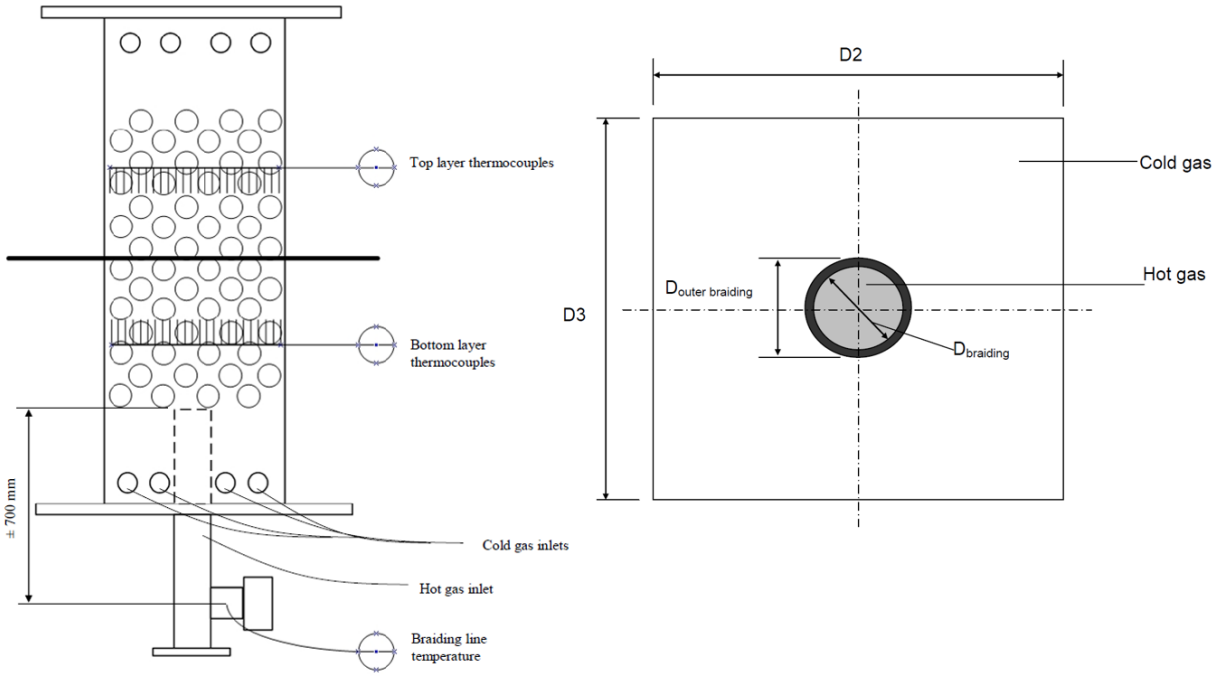

Figure 3-12: (a) BETS schematic; (b) Cross-sectional inlet geometry (Adapted from Kgame, 2010)

Table 3.1: BETS 0.36 structural dimensions (Kgame, 2010; Du Toit and Rousseau, 2014)

Dimension	Value
Pebbles (-)	3 898
Pebble diameter, d_p (mm)	28.58
Porosity including spacers (-)	0.352
Porosity excluding spacers (-)	0.369
D1 (mm)	741.1
D2 (mm)	300.0
D3 (mm)	300.0
$D_{braiding}$ (mm)	77.0
$D_{outer\ braiding}$ (mm)	79.58

The BETS 0.36 separate effects tests were conducted for a series of Reynolds numbers, ranging from 1000 to 40000. The desired Reynolds numbers were indirectly achieved by manipulating the system pressure between 1 and 38 bar(a). Furthermore, four test runs were conducted for each selected Reynolds number to ensure repeatability. Inlet measurements included the system pressure, along with the temperature and mass flow rate of both the cold and braiding gas. The

mass flow rates were recalculated as superficial velocities. In addition, all values were subjected to an uncertainty analysis (Kgame, 2010). The cold gas, braiding gas and finally the total Reynolds numbers at the inlet conditions were defined as follow (Kgame, 2008):

$$Re_{cold\ gas} = d_p \left(\frac{\dot{m}}{A\mu}\right)_{cold\ gas} \tag{3.6}$$

$$Re_{braiding\ gas} = d_p \left(\frac{\dot{m}}{A\mu}\right)_{braiding\ gas} \tag{3.7}$$

$$Re_{total} = f Re_{cold\ gas} + (1-f) Re_{braiding\ gas}, \qquad f = \frac{\dot{m}_{cold\ gas}}{\dot{m}_{total}} \tag{3.8}$$

where $\dot{m}_{cold\ gas}$ is the total cold gas mass flow rate (kg/s), $A_{cold\ gas}$ is the total cross-sectional flow area of the cold gas or annulus (m^2) and $\mu_{cold\ gas}$ is the dynamic viscosity of the cold gas (Pa·s). Similarly, $\dot{m}_{braiding\ gas}$ is the mass flow rate of the braiding gas (kg/s), $A_{braiding\ gas}$ is the cross-sectional area of the braiding gas inlet pipe and $\mu_{braiding\ gas}$ is the dynamic viscosity of the braiding gas (Pa·s). Furthermore, f is the mass flow ratio of the cold gas to the total gas flow (-) and $\dot{m}_{total}$ is the total mass flow rate of all gas streams (kg/s). Re_{total} represents the total mass flow-averaged particle or superficial Reynolds number which was used to evaluate all experimental Reynolds numbers at the corresponding inlet conditions.

The radial temperature profiles were measured by using two sets of thermocouples (Figure 3-12 (a)). These sets were located at approximately one third from the bottom and top at $z = 247\ mm$ and $z = 497\ mm$, respectively, with the origin of the z-coordinate located directly below the first layer of spheres. Each set of thermocouples were positioned between the spheres (Figure 3-13) and contained a total of 19 thermocouples situated on both sides of the centre y-line (Figure 3-14) (Kgame, 2010). It should be noted that the tips of the top layer thermocouples were almost adjacent to the spheres, whereas the bottom layer thermocouple tips were adjacent to the cables and located in the centre of larger gaps. The reader is referred to the Kgame (2010) for information regarding the transverse or radial coordinates of the thermocouples, as well as the experimentally measured braiding and normalised temperature profiles. In addition, Kgame (2010) provides a thorough uncertainty analysis on several variables related to the BETS separate effects tests and the HPTU plant.

Figure 3-13: Top layer thermocouple arrangements (Kgame, 2008)

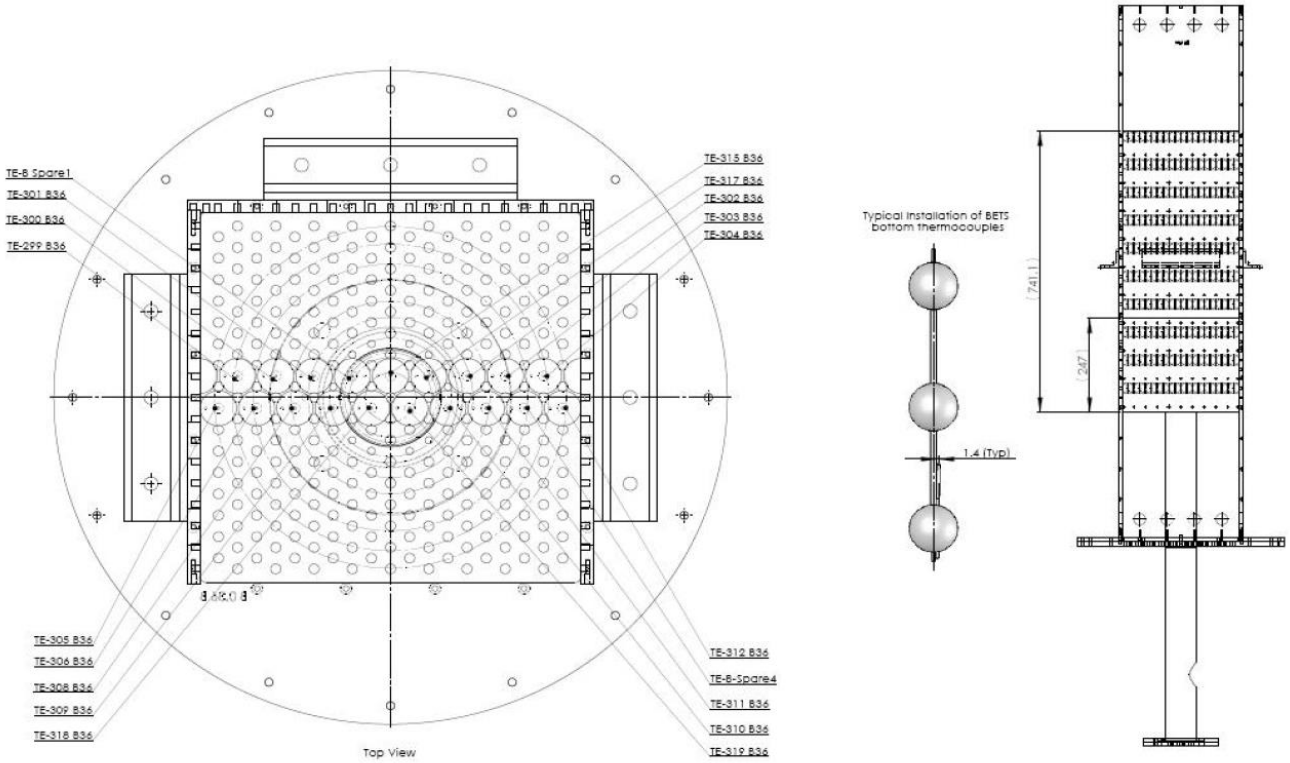

Figure 3-14: Bottom layer thermocouple configurations (Kgame, 2010)

3.3.2 Previous CFD simulations

Kgame (2010) evaluated the fluid effective radial thermal conductivity for each BETS experiment by implementing a search algorithm into the CFD code Flo++®. It was initially determined that braiding temperature profiles are independent of the domain volume as a result of their symmetrical nature. This was accomplished by using a guessed effective thermal conductivity to obtain radial temperature profiles for several models. These models included domains which consisted either of the full cross-sectional area or a half, a quarter or an eighth thereof. The simulated temperature profiles were practically identical for each case.

Following the volume independency study, only an eighth of the cross-sectional area of the original domain was simulated. The resulting domain was meshed with coarse structured grids, being either of the Cartesian or cylindrical type (Figure 3-15). Each grid contained 5 cells in the azimuthal direction, 18 cells in the radial direction and 91 cells in the axial direction (Kgame, 2010).

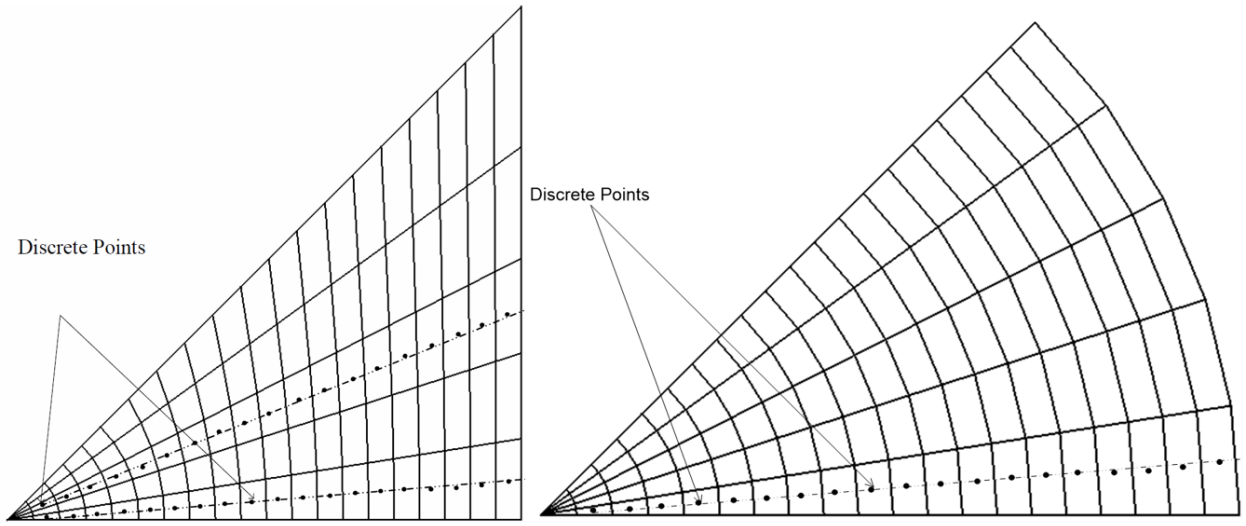

Figure 3-15: Structured CFD grid representations (a) Cartesian; (b) Cylindrical (Adapted from Kgame, 2010)

The search algorithm in the CFD code required both the inlet conditions and experimentally measured temperature profiles as input. The braiding temperature profiles were subsequently subjected to polynomial regression. An initial value of the fluid effective thermal conductivity was supplied to the algorithm, where after corresponding radial temperature profiles were generated.

These simulated temperature profiles were compared to the regressed experimental temperature data to consequently obtain a new constant value for the thermal conductivity. This iterative process was continued until the desired amount of convergence has been achieved (Kgame, 2010).

Preller (2011) conducted a subsequent, preliminary study in which a single case of the BETS 0.36 experiments ($Re_{total} = 3000$) was simulated by using STAR-CCM+®. The computational domain was firstly reduced by only considering the first 15 layers of spheres and secondly by imposing symmetry boundary conditions on three vertical planes (Figure 3-16). Consequently, the simulation was restricted to the bottom layer temperature profiles and only 25% of the original cross-sectional area was simulated. These reductions resulted in a symmetry model with 386 spheres (Du Toit *et al*., 2012b). No cables or spacers were simulated.

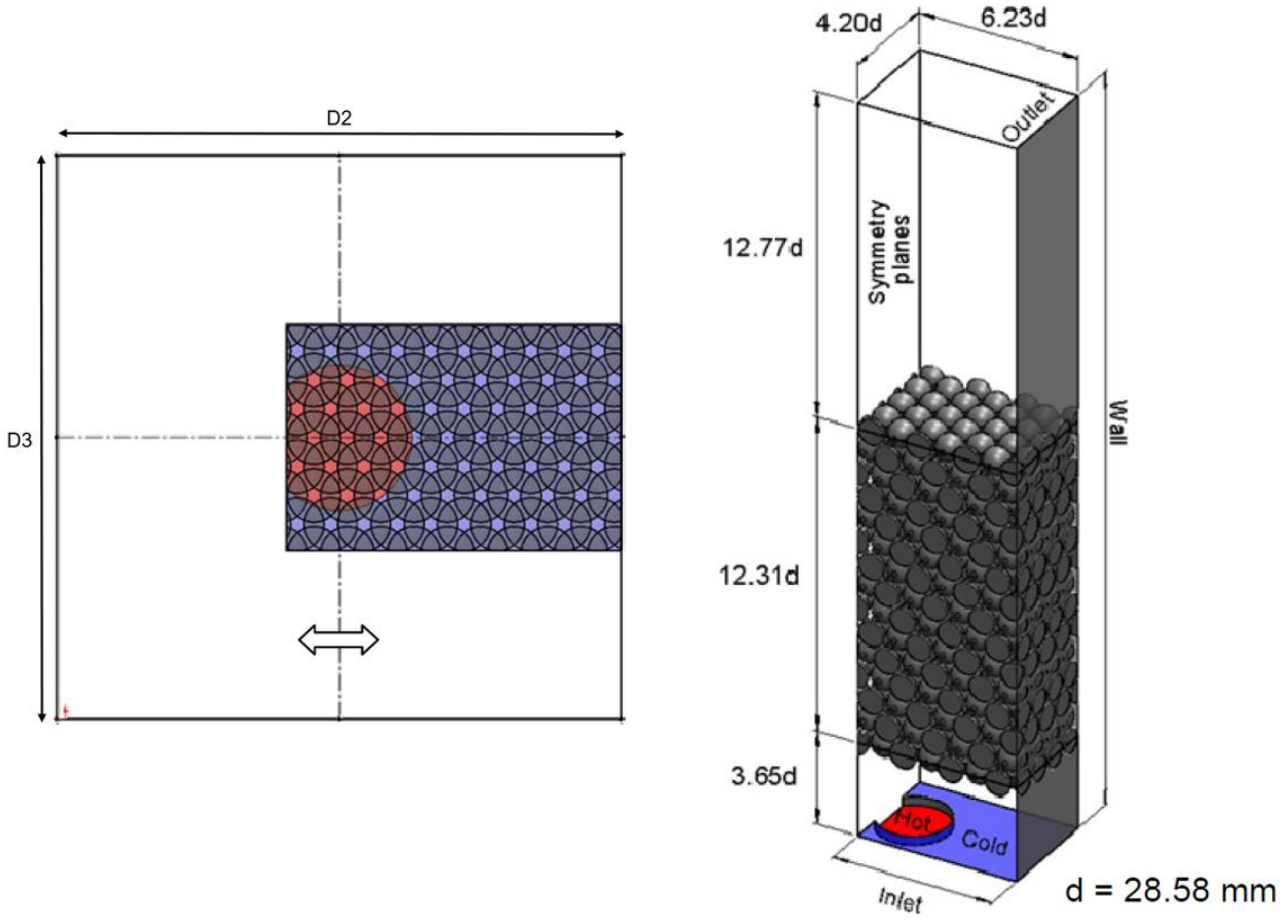

Figure 3-16: Preller symmetry model (a) Top view of cross-sectional area; (b) Geometrical description and dimensions (Adapted from Preller, 2011)

The symmetry model was meshed with polyhedral volume cells without prism layers. This resulted in a volume mesh that contained approximately 9.2 million cells. The turbulence was modelled by using LES with the WALE SGS model, which resulted in good agreement between the simulated and experimentally measured bottom layer temperature profile. Nevertheless, large temperature gradients were observed in the simulation near the radial centre of the packed bed, with temperature differences of up to 10°C in the gaps where the thermocouples were positioned. Furthermore, the simulation residuals displayed transient behaviour along with instabilities (Preller, 2011). This study attempted to resolve the abovementioned simulation difficulties and is subsequently an extension of the preliminary work done by Preller (2011).

3.4 Summary

This chapter examined the structural characterisation and thermohydraulic behaviour of packed beds. Furthermore, the differences between implicit and explicit numerical modelling has been discussed and a short review was given on the latter. In addition, random packings have been compared to structured packings. The chapter was concluded by reviewing the experimental setup of the BETS separate effects tests and associated CFD studies. The groundwork for this study has been discussed and therefore Preller's (2011) work can now be extended.

CHAPTER 4: SIMULATION METHODOLOGY

4.1 Introduction

This chapter will firstly verify the simulation work conducted by Preller (2011), followed by a symmetry evaluation study. Thereafter, a suitable, efficient and universal simulation methodology will be developed for validating a range of BETS experiments by considering various aspects of CFD.

4.2 Literature verification

This work is an extension of the BETS 0.36 simulations conducted by Preller (2011). Preller (2011) investigated a single case of the BETS 0.36 experiments at a Re_{total} of 3000. Accordingly, it was required to verify the simulation setup and the corresponding simulated temperature profiles.

Firstly, a representative structured pebble bed was created in SolidWorks® by importing the actual BETS 0.36 centroid coordinate data with a linear pattern macro. The computer aided design (CAD) model was identical to the symmetry model in Figure 3-16, apart from the extrusion of the braiding gas inlet pipe into the domain. This inlet pipe and its wall thickness (Figure 3-12 (b)) was excluded by Preller (2011). The exact length of the pipe is unknown (Figure 3-12 (a), Figure 3-14). Consequently, a pipe length of $3.6d_p$ was assumed since the braiding gas was introduced just below the first layer of spheres (Rousseau and Van Staden, 2008; Kgame, 2010). The wall thickness of the pipe was excluded by Preller (2011) by only using its outlet diameter in the symmetry model, thereby increasing the cross-sectional area of the hot inlet by 6.8%.

The simulation was subsequently set up in STAR-CCM+® with settings that corresponded to Preller (2011). These settings included initial and boundary conditions, as well as the general mesh and physics continua. Similar to Preller's (2011) simulation, transient behaviour and instabilities were displayed through the residuals, which was subsequently studied in more detail.

4.2.1 Residual analysis

Residual analyses were conducted to determine the optimal simulations settings and techniques that would reduce and stabilise the residuals of the continuity, momentum and energy equations. The search was narrowed down by temporally excluding the effects of mesh settings on the residuals.

LES is an inherently transient technique that requires the specification of appropriate time steps. It is good practice to initiate simulations with a large time step, followed by a gradual decrease until a sufficiently small time step is reached. An outline of the time step reduction method that was used by Preller (2011) is given in Du Toit *et al*. (2012b). However, the rate at and extend to which the time steps were reduced appeared too rapid and too large. Consequently, a new method was developed.

The simulation was started with the steady-state Realizable k-ε turbulence model to develop the flow field. The residuals displayed repetitive transient behaviour throughout the simulation. After 2500 iterations, the k-ε turbulence model was substituted with LES accompanied by the WALE SGS model. The time step was gradually decreased from 1.0 s to 1.0 ms, which resulted in a considerable reduction in the residual instabilities. Nonetheless, the size of the residuals was still unsatisfactory and therefore additional processing was done by individually reducing the under-relaxation factors (URFs) of several solvers at a constant time step of 1.0 ms. These solvers included the velocity and pressure solver for segregated flow, as well as the fluid's segregated energy solver; the segregated flow solver was chosen over the coupled flow solver to comply with Preller (2011). The residuals were notably lowered by reducing the velocity solver's URF. The z-momentum was particularly influenced with a residual reduction of over two orders in magnitude. The z-momentum corresponded to the principal and axial direction of the flow and was therefore the most sensitive to the velocity solver's URF. In contrast, the URFs of the other solvers appeared be ineffective in lowering and stabilising the residuals at the specified time step. The final residuals of both studies are compared in Table 4.1.

The results show a remarkable reduction in the residuals. The larger x, y-momentum residuals reflect the continuous lateral mixing in the x, y-planes. Nonetheless, ideal simulation practices have been determined for reducing residuals and for improving the overall simulation stability.

Table 4.1: Residual comparison

Study	Final residuals				
	Continuity	x-momentum	y-momentum	z-momentum	Energy
Preller (2011)	6.9e-03	3.2e-01	3.3e-01	1.1e-01	7.3e-02
This study	1.6e-04	9.3e-03	2.4e-03	1.8e-04	5.6e-05

4.2.2 Results and discussion

The resulting radial temperature profile from the residual analysis is compared with that of Preller (2011) and with the experimentally measured BETS temperatures in Figure 4-1. Unfortunately, only the radial coordinates of the thermocouples are available in Kgame (2010). Consequently, the simulation coordinates were firstly converted from Cartesian to radial, which was followed by converting all coordinates on both sides of the centre x-line (Figure 3-14 and Figure 3-16 (a)), to absolute or positive values to correspond with the original representation of Preller's (2011) results.

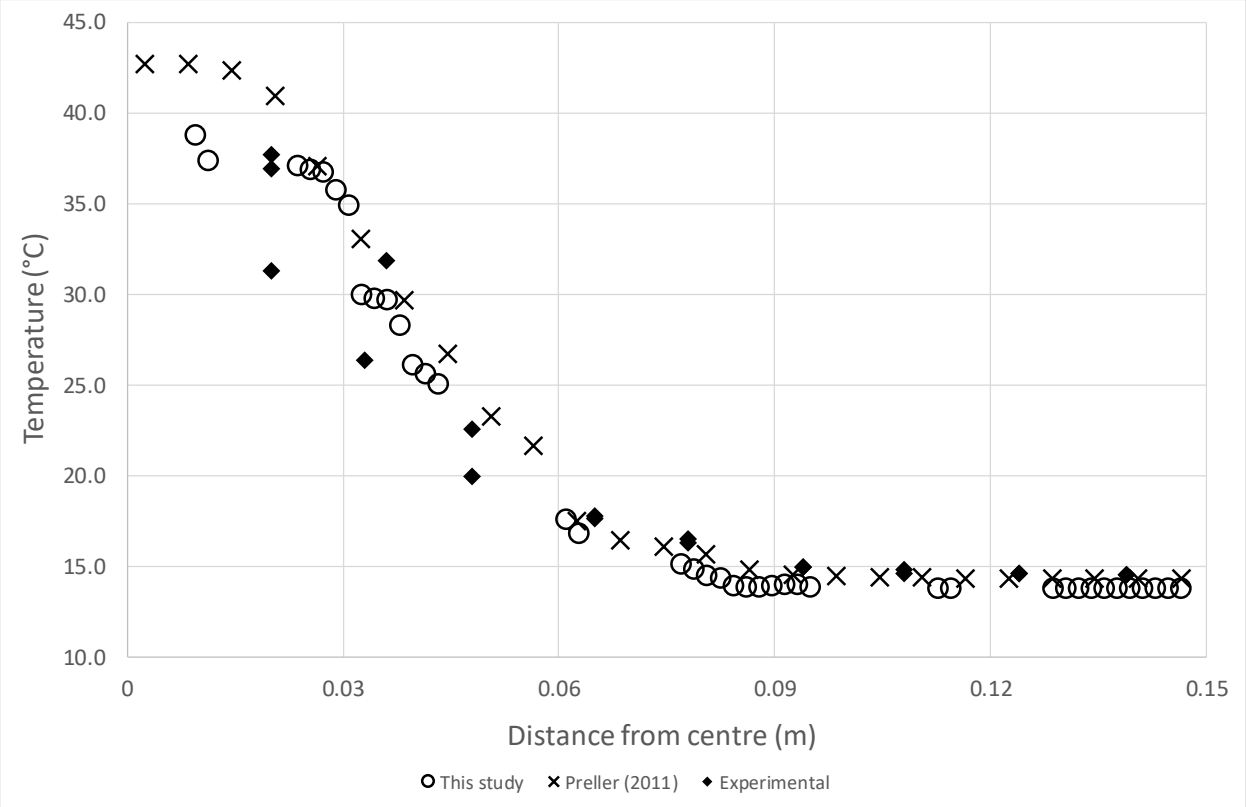

Figure 4-1: Preller (2011) verification

This verification study utilised a line probe at $z = 247\ mm$ on the centre y-line to extract simulated temperatures, whereas Preller (2011) used plane sections for data extraction. The former method is associated with vertex or interpolated data, whereas the latter is related to cell centroid data and is consequently dependent on the mesh resolution. Furthermore, the radial gaps that occurred in the extracted line probe data are caused by interfering spheres. The plane section extraction method acquires a large set of data which consequently demands an excessive amount of post-processing in spreadsheets, whereas the line probe data can be used directly after converting the coordinates from Cartesian to radial since the data does not require sorting.

The simulated temperature profiles of both studies are in good agreement with the experimentally measured temperature data. The results from this study show a moderately improved agreement with experimental temperatures over that of Preller (2011). The effect of the braiding gas inlet pipe was investigated in preliminary simulations. A small increase in the overall temperature profile and a larger amount of scattered data was observed when excluding the braiding gas inlet pipe. The increased temperatures are also noticeable from Preller's (2011) simulated temperature profiles. The phenomenon probably results mainly from early mixing between the hot and cold nitrogen gas streams. In addition to the increased temperatures, the initial study also displayed decreased stability, especially in the flow field development stage. These instabilities are also portrayed by the residuals. Nevertheless, Preller's (2011) work has been verified to be capable of numerically validating the BETS 0.36 experimental data.

4.3 Symmetry evaluations

4.3.1 Introduction

The flow in the BETS experiments and simulations was not completely symmetrical. This, for instance, is evident from the scattered experimental temperature profiles near the cross-sectional centre of the bed in Figure 4-1. Consequently, the temperature profile deviates moderately from a typical bell curve plot. Therefore, it was required to investigate the effect of different symmetry and periodic boundary conditions on the temperature profile. The bottom view perspectives representing the cross-sectional areas of the different models are displayed in Figure 4-2.

In each case, the symmetry boundaries are represented by the red lines, whereas the blue line indicates the coupling that was used between purely rotational periodic boundaries. The mesh

settings corresponded to that of Preller (2011), which followed the subsequent assumption of mesh independency. Furthermore, unless stated otherwise, the simulations were conducted at steady-state with the Elliptic Blending RSM turbulence model instead of LES.

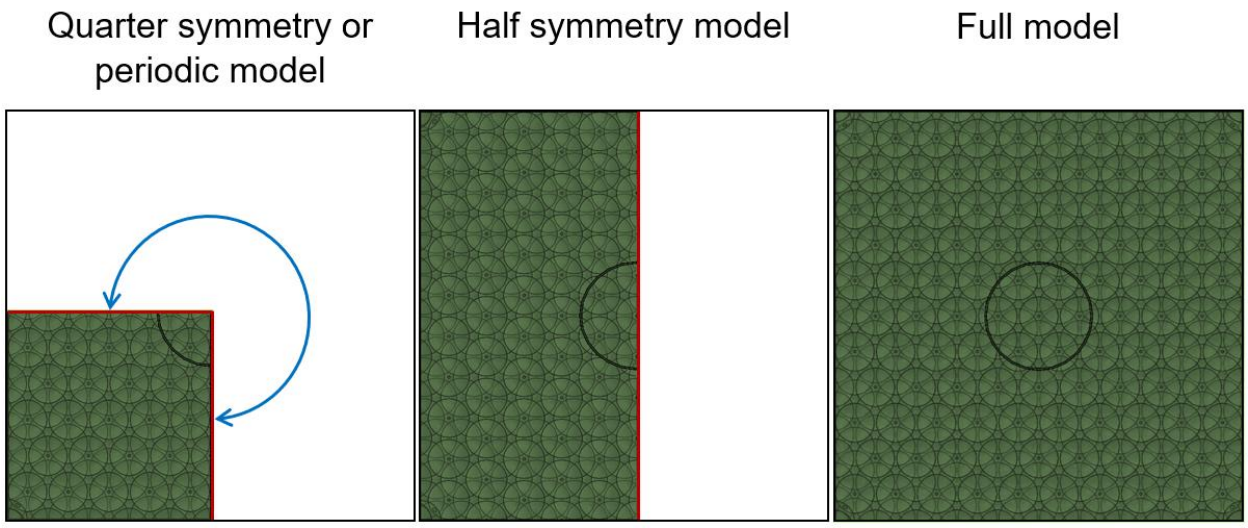

Figure 4-2: Bottom view perspectives representing the cross-sectional areas of different symmetry evaluation models (a) Quarter models; (b) Half model; (c) Full model

4.3.2 Quarter models

4.3.2.1 Symmetry boundary conditions

According to Siemens PLM Software (2017), there is no shear stress or heat flux at a symmetry boundary. Furthermore, velocities, pressures and temperatures on symmetry plane faces are computed by means of reconstruction gradients from plane adjacent cells. Velocity vectors are consequently forced to move parallel to the plane in the axial direction which can result in increased axial velocities and the possibility of affecting local temperatures.

The influence of symmetry boundary conditions on the temperature profile was investigated by using two symmetry planes to create a quarter symmetry model (Figure 4-2 (a)). Similar to that of Preller (2011), this model represented 25% of the original cross-sectional area, whereas the length of the outlet domain was reduced from $12.77d_p$ (Figure 3-16 (b)) to $10d_p$.

The $10d_p$ outlet domain length was subsequently used for all symmetry evaluation models with the intension of lowering the cell count in larger models. The number of cells was consequently reduced from 9.2 million (Preller, 2011) to 8.8 million. Furthermore, in both quarter models, the radial temperature profiles were extracted just below the centre y-line (Figure 3-14).

4.3.2.2 Periodic boundary conditions

An internal interface was set up between the two planes or boundaries in Figure 4-2 (a). The topology was chosen to be periodic. The periodicity refers to the geometrical transformation applied to the vertices of the slave boundary with the purpose of coinciding with that of the master boundary. The periodicity was set to purely rotational about the z-axis. The interface coupling is indicated by the blue line in Figure 4-2 (a). STAR-CCM+® subsequently attempts to create a conformal mesh in both the surface and volume mesh generation stages. Interface conformity is achieved when both boundaries share exact vertex locations and face topologies (Siemens PLM Software, 2017).

The slave boundary corresponded to the centre x-line, whereas the master boundary was situated on the centre y-line. The boundaries were nonconformal since the slave and master boundaries respectively had areas of 7.8E-02 and 8.6E-02 m^2 available for fluid flow, owing to the different number of spheres with which each boundary plane had intersected. The slave boundary subsequently consisted of 33033 faces, while the master boundary was composed of 34237 faces. Nevertheless, the meshing procedure was successful, and convergence has been achieved. In addition, the mass flow-averaged (MFA) velocities in the vicinity of the periodic boundaries differed by less than 0.005 m/s.

4.3.2.3 Results and discussion

The resulting temperature profiles from both simulations were compared to the experimentally measured BETS temperatures. The results are displayed in Figure 4-3. The temperature profiles of both quarter models are in good agreement with the BETS experimental data in regions that are further away from the radial centre of the bed. In contrast, the temperatures near the radial centre display scattered behaviour and are overpredicted, presumably due to increased temperature gradients and asymmetrical, transient flow behaviour. Lastly, the quarter symmetry

model demonstrates improved simulation performance over that of the quarter periodic model in near centre region.

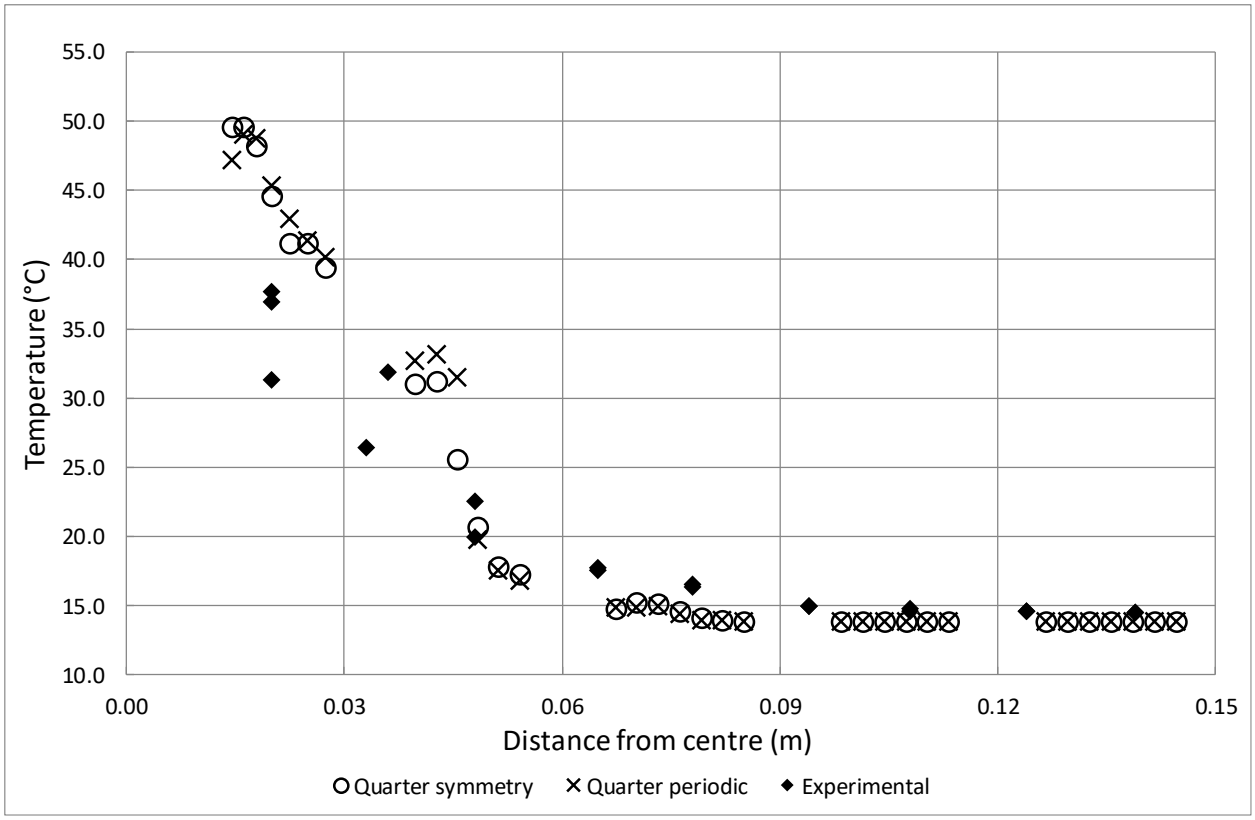

Figure 4-3: Quarter model evaluations

4.3.3 Half symmetry model

Following the successful simulation of the quarter symmetry and periodic models, a half symmetry model was set up to simulate 50% of the total cross-sectional area (Figure 4-2 (b)). This was done by utilising one symmetry plane that was situated on the centre x-line. In contrast to the quarter models and similar to the previous symmetry model used by Preller (2011), the half symmetry model allowed temperature extraction on both sides of the centre y-line. Therefore, two line probes were used in the extraction, one slightly below and the other slightly above the centre y-line. Furthermore, the half symmetry model was considered to be more valid than the previously simulated models since its reflection about the centre x-line covers the whole cross-sectional area, unlike the other symmetry models. However, the number of cells was increased from 8.8 million to approximately 18 million which resulted in flow field initialisation and development difficulties.

The simulated temperature profiles are compared with the normalised BETS temperature data in Figure 4-4. The resulting temperature profiles from the half symmetry model simulation display improved agreement with the experimental temperature data near the radial centre over that of the quarter models. The overprediction of the radial temperatures is reduced considerably. Nevertheless, an increased amount of data scattering is observed, although the half symmetry model simulation displays improved residual stability over that of the quarter models.

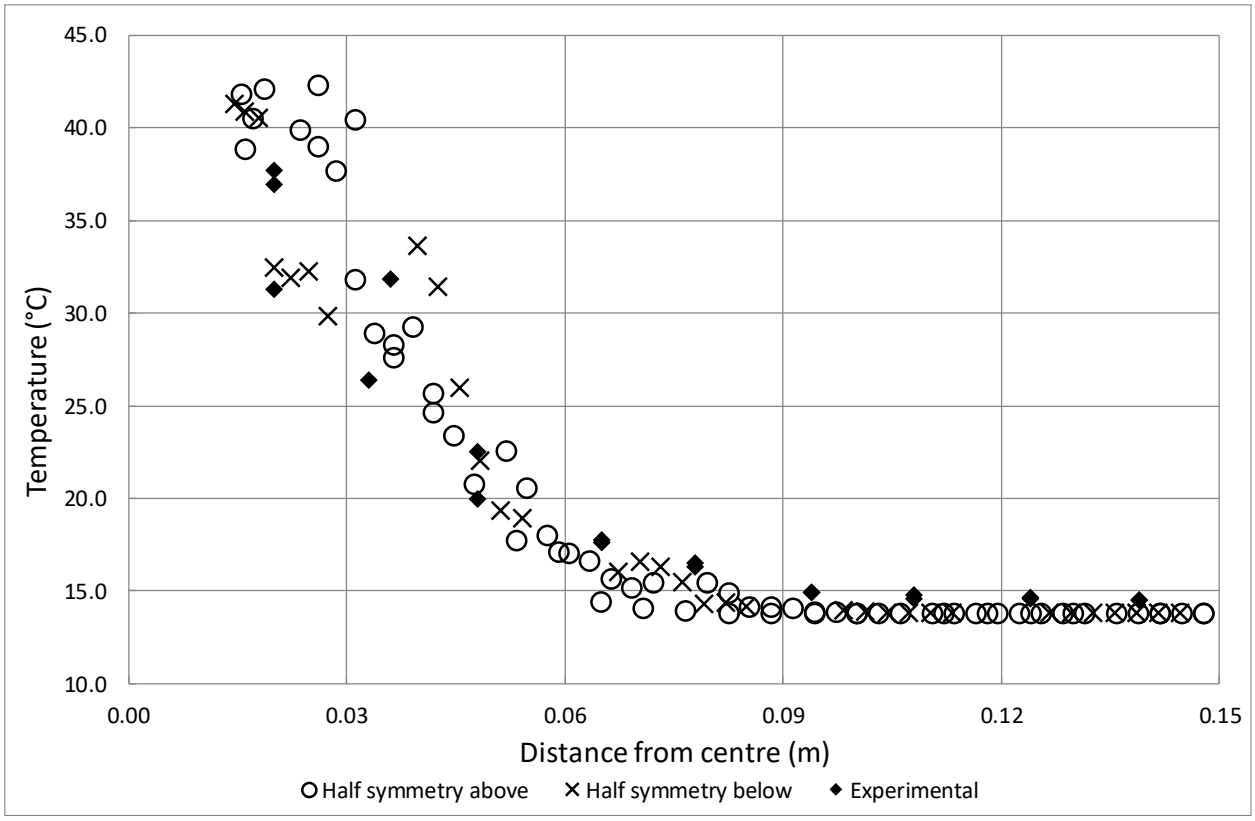

Figure 4-4: Half symmetry model evaluation

4.3.4 Full model

The final evaluation excluded symmetry or periodic boundary conditions by simulating the full cross-sectional area (Figure 4-2 (c)). Subsequently, the volume mesh contained 37 million cells, which significantly increased the amount of computational resources required to simulate the given problem. Similar to the half symmetry model, two line probes were used on both sides of the centre y-line with the difference that their lengths were subsequently extended to include all x-values within the domain.

The large number of cells increased the complexity of converging the simulation. In several cases, initialisation failed and in cases wherein it was successful, the flow field could not be fully developed, which ultimately led to divergence. Several attempts have been made to overcome these simulation difficulties by using both RANS and uRANS turbulence models. Unfortunately, these attempts were unsuccessful and consequently LES had to be used. The resulting radial temperature profiles from the LES simulation are displayed in Figure 4-5.

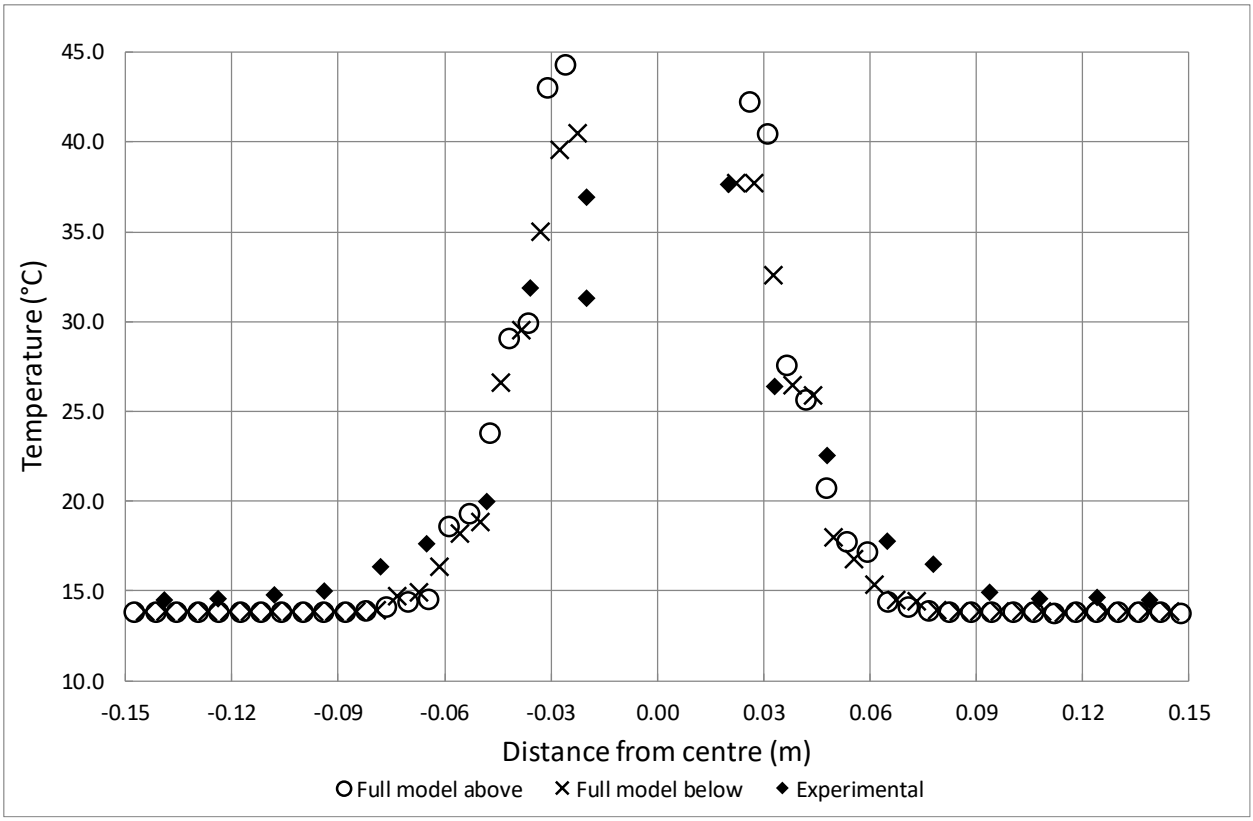

Figure 4-5: Full model evaluation

The negative radial coordinates correspond to temperatures that were extracted to the left of the centre x-line. The simulated temperature profiles of the full model are less scattered than that of the half symmetry model and display slightly improved agreement with the experimental temperatures data, despite the increased simulation complexity. Nonetheless, similar to the previous evaluations, heating delays were still observed at $x = \pm 0.09m$ and temperatures near the centre of the bed were still overpredicted.

4.3.5 Conclusions

The influence of symmetry and periodic boundary conditions on the simulated radial temperature profiles were investigated since the flow through the packed bed was not completely symmetrical. From the evaluations, it can be concluded that these boundary conditions do affect the simulated temperature profiles to a certain extent. These disturbances include heating delays, as well as scattered and overpredicted data. In addition, it is preferred that the largest amount of cross-sectional area should be retained in the analysis of radial thermal dispersion, which places additional constraints on symmetry assumptions. Consequently, symmetry and periodic boundary conditions were not further investigated. Attention was therefore restricted to the full model and the subsequent development of a suitable, efficient and universal simulation methodology, which could be applied to the entire validation study.

4.4 Methodology development

4.4.1 Introduction

Following the results from the previous sections, a suitable simulation methodology had to be developed for simulating the full cross-sectional model. It was mentioned earlier that the complexity of the simulation increases when excluding symmetry or periodic boundary conditions. An improved simulation methodology was therefore required to overcome simulation difficulties and to increase simulation stability, convergence and accuracy. In addition, the methodology had to be universal. Consequently, the entire methodology was solely based on a Re_{total} of 3000, with its corresponding agreement to the normalised experimental temperature profiles and developed in such a manner to be extended to and applicable for Reynolds numbers of up to 40000, while retaining the original framework.

Subsequently, several analyses had to be conducted to arrive at the preferred simulation methodology. These analyses included, among others, mesh quality analyses, a mesh independency study, integrated turbulence model and residual assessments, the evaluation of different temperature extraction methods, as well as wall treatment considerations. In addition, these aspects were to be accommodated with appropriate simulation stability conditions and convergence criteria.

4.4.2 Mesh quality analyses

Hitherto, the original mesh settings from Preller (2011) were used for all simulations. These settings are summarised in Table 4.2. It was previously stated that the application of these mesh settings to the full model resulted in a mesh with 37 million volumetric cells. It is important to note that no prismatic cell layers were used and that packed region of the bed contained a refined mesh. Prism layers are responsible for capturing viscous and thermal gradients along the wall. In addition, the volume mesh was composed of polyhedral-shaped cells. Polyhedral meshes are ideal for simulating heat transfer, complex flows, as well as flows that exhibit large amounts of swirling (Siemens PLM Software, 2017).

Table 4.2: Preller (2011) mesh settings

Region	Parameter	Value
Global	Surface curvature	63.0 points per circle
	Surface growth rate	1.5
	Minimum cell size	1.0 mm
	Target cell size	3.5 mm
	Polyhedral mesh density	1.0 mm (Default)
	Polyhedral mesh growth factor	1.0 mm (Default)
Spheres	Minimum cell size	0.6 mm
	Target cell size	0.8 mm

The quality of a volume mesh has an influence on simulation stability, convergence and accuracy (Siemens PLM Software, 2017). It was subsequently required to investigate the optimum mesh settings that would result in a high quality mesh without using an excessive number of cells and thereby sacrificing unnecessary computational resources. The aim of the mesh quality investigation was ultimately to isolate and fix essential mesh parameters (except the base cell size) to their optimal values and subsequently use the resulting mesh settings in the mesh independency study (Section 4.4.3).

A comprehensive set of mesh analyses was therefore conducted to investigate the effect of selected mesh parameters on the overall volume mesh quality, which can be evaluated by using mesh metrics. Seven different mesh metrics are incorporated into STAR-CCM+® and are available as field functions. The cell quality, volume change and cell skewness angle are

considered to be the most important mesh metrics and were therefore used in this investigation (Siemens PLM Software, 2017).

Firstly, cell quality is computed by means of cell gradient calculations methods and is a function of both the relative geometrical distribution of cell centroids of face-adjacent cells, as well as the orientation of the cell faces. Low cell qualities are generally associated with flat cells in which the faces are particularly non-orthogonal, as well as degenerate cells. High cell qualities, near or equal to one, are associated with perfectly formed cells such as cubic or well-shaped polyhedral cells. Cells with a quality less than 0.001% are considered to be invalid, nevertheless it is recommended for cell qualities to exceed 50%. Although valid solutions can be achieved with lower quality cells depending on the physics, these cells can affect both the robustness and accuracy of a simulation (Siemens PLM Software, 2017).

Secondly, in STAR-CCM+® the volume change metric ascribes to the volume ratio between a cell and its largest adjoining neighbour. For the sake of clarity, the volume change metric will henceforth be referred to as the volume ratio since the terms are synonymous in this case. Invalid cells have volume ratios of 0.01 or lower. In general, volume ratios should be greater than 0.5, or in other words, a cell's size may not be twice the size of its neighbours. This implies that the cell growth rates should not be too rapid, a phenomenon which typically occurs with flat cells. Cells with low volume ratios can contribute to decreased solver stability and loss of accuracy (Siemens PLM Software, 2017).

Lastly, the cell skewness angle (θ) is defined as the angle between the face area or face normal vector ($\boldsymbol{a}$) and the centroid connecting vector ($\boldsymbol{ds}$). This is illustrated in Figure 4-6. A completely orthogonal mesh will subsequently have a θ of 0°. The scalar field function only displays the largest calculated angle for a given cell. Cells that have a θ of 85° or larger are considered to be invalid. Large angles can affect the computational accuracy of diffusion terms, as well as the robustness of a simulation. The vector dot product of $\boldsymbol{a}$ and $\boldsymbol{ds}$ is found in the denominator of the diffusion term formulation. Consequently, angles of 90° or greater can also affect convergence and result in divergence due to division by zero (Siemens PLM Software, 2017).

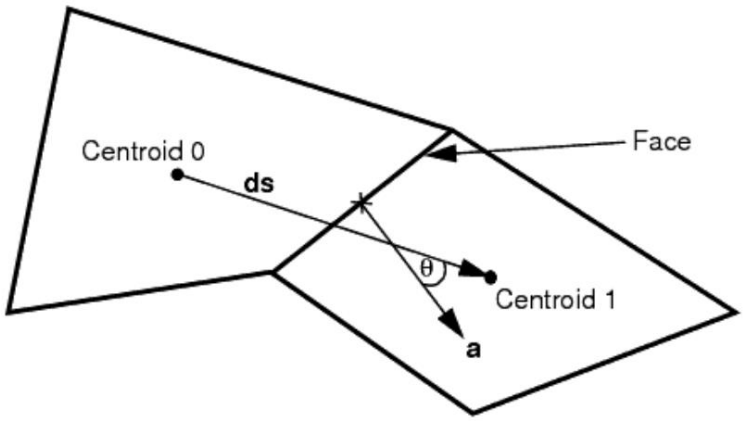

Figure 4-6: Cell skewness angle (Siemens PLM Software, 2017)

The three selected mesh metrics were subsequently used to conduct comprehensive mesh quality analyses. The length of the full model was decreased by reducing the model from 15 axial layers of spheres to only 5 layers to accelerate meshing procedures, while retaining the original inlet, outlet and radial dimensions. This is illustrated by the CAD models in Figure 4-7.

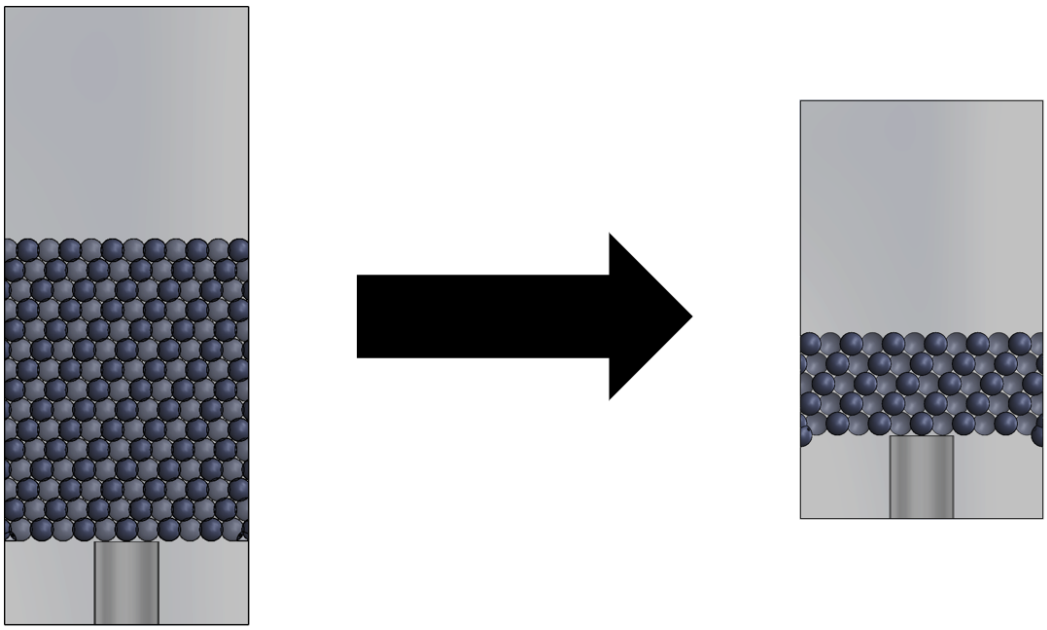

Figure 4-7: Reduced CAD model for mesh quality analyses

The model reduction resulted in a decrease from 38 to 15 million cells when using the same mesh settings as Preller (2011) (Table 4.2). In addition, the maximum mesh metric difference between the two models was associated with cell quality, wherein the number of cells with a quality lower

than 50% was decreased by 7%. Given the large reduction in the number of cells, the difference was considered to be insignificant. The reduced model was therefore believed to be a valid and an accurate representation of the full model and was subsequently used throughout the mesh quality analyses.

Several mesh sensitivity analyses were conducted in which selected custom mesh controls or mesh parameters were altered to investigate their effect on the number of cells and on the previously discussed mesh metrics. The former was therefore associated with the amount of computational resources required, while the latter corresponded to the overall mesh quality. A compromise between these parameters had to be found. All mesh metric data and scenes were generated in and extracted from STAR-CCM+® by using the meshing tutorial macro written by Michael Elmore (Siemens PLM Software, 2017). The principal results from the mesh sensitivity analyses, accompanied by that of a mesh quality comparison is given in Table 4.3.

In the first part of Table 4.3, the mesh sensitivity is summarised by relating parameter adjustments (in terms of constant increments) to the percentage by which the number of cells is increased. All mesh parameters, excluding the target cell size, displayed near linear relationships between their increments and the resulting number of cells. Furthermore, local mesh refinement around the spheres was excluded, contrary to the case of Preller (2011). A single set of mesh parameters was therefore used throughout the domain. This resulted in a further reduction in the number of cells, even with the addition of prism layers, when compared to the mesh settings used by Preller (2011). Subsequently, a constant global minimum cell size of 1.0 mm was used throughout the analyses.

The differences in the number of cells and mesh metrics were insignificant throughout the surface growth rate variations from 1.1 to 1.5. The parameter was subsequently left at a default value of 1.3. It was further found that the cell count was sensitive to both the polyhedral mesh density and growth factor. The former was adjusted from 0.9 to 1.3, whereas the latter was varied between 0.8 and 1.0, both with their corresponding increments. An increase in the mesh density and decrease in the growth factor resulted in moderate improvements in both the overall cell quality and volume ratio, while insignificant differences were observed in the cell skewness angles. These mesh quality improvements supported an increased mesh density of 1.2 and a decreased growth factor of 0.85, without resulting in an excessive number of cells.

Table 4.3: Mesh sensitivity and overall quality

Mesh parameter	Increment	Cell increase (%)	Preller (2011)	Final settings
Surface growth rate	0.1	0.45	1.5	1.3
Polyhedral mesh density	0.1	6.2	1.0	1.2
Polyhedral growth factor	0.05	-4.4	1.0	0.85
Total prism layer thickness	0.1 mm	-1.6	N/A	0.7 mm
Prism layers	1 layer	15.7	0	2
Global target cell size	0.5 mm	-20.6 to -4.6	3.5 mm	4.0 mm
Refined target cell size			0.8 mm	N/A
Number of cells			15.4 million	9.7 million
Cells with quality < 50%			52.2%	25.4%
Cells with volume ratios < 0.5			78.4%	39.2%
Cells with skewness angles > 50°			0.08%	0.48%
Maximum cell skewness angle			77.4°	86.7°

The first three analyses were followed by the addition of prism layers. Two prism layers were used to investigate the effect of the total prism layer thickness on both the number of cells and on the mesh quality. The thickness was varied from 0.07 to 1.4 mm. A constant increment was used for the greater part of the analysis. An average value is used to represent the corresponding increase in the number of cells to accommodate for the fluctuating nature of the data. The cell quality decreased insignificantly with increasing prism layer thickness. In contrast, the volume ratio improved moderately with increasing thickness up to 0.8 mm, which was followed by deterioration. In addition, the thinner layers displayed slightly improved cell skewness. However, the disadvantages of flat cells have already been discussed and thicker prismatic cell layers result in a reduced number of cells. Consequently, a total prism layer thickness of 0.7 mm was chosen and subsequently used to evaluate the effects of increasing the number of prism layers. The number of layers was only varied from 2 to 4. The cell quality and volume ratio improved with each added layer. Nevertheless, these improvements were not justified by the significant increase in the number of cells and the risk of cells becoming too flat. Consequently, the number of prism layers was left at the default value of 2.

Finally, the target cell size was varied from 2.0 to 4.0 mm. An increase in the target cell size resulted in a moderate decrease in cell quality, along with a considerable decrease in the number

of cells. Both decreases follow nonlinear behaviour wherein the initial response is significant contrary to the final response. This is clear from Table 4.3 where the initial increment decreases the number of cells by over 20%, whereas the final increment only results in a decrease of 4.6%. The volume ratio and cell skewness metrics were practically unaffected throughout the analysis. The target cell size was subsequently fixed to 4.0 mm since the minimum number of cells was preferred. This setting also corresponds to the default mesh settings of STAR-CCM+® wherein the target cell size is 4 times as large as the minimum cell size.

The resulting volume mesh is compared to that of Preller (2011) in Table 4.3. It should firstly be noted that the number of cells is decreased by 37%, even with the addition of 2 prism layers. Secondly, significant improvements have been made over both the overall cell quality and volume ratio. Finally, an increase in cell skewness is noted. Nevertheless, it is not of concern as it arises from the introduction of prism layers. This concludes the mesh quality analyses.

4.4.3 Mesh independency study

The final mesh settings, that are presented in Table 4.3, were subsequently used to conduct a mesh independency study to determine the maximum allowable base cell size that produces a mesh independent solution or, more specifically, temperature profile. The minimum and target cell sizes were set to 25% and 100% of the base cell size (B), respectively. The base cell size was subsequently the only adjustable mesh parameter following the optimisation of the other mesh parameters in the previous section.

4.4.3.1 Preliminary turbulence model assessments

The mesh quality optimisation was followed by turbulence model assessments. The use of Steady-state RANS turbulence models was preferred over LES to reduce simulation complexity and associated computational difficulties. The following RANS turbulence models were evaluated based on simulation stability and convergence: Standard k-ε, Realizable k-ε, Standard k-ω, SST Menter k-ω, as well as the RSM turbulence model.

The abovementioned turbulence models were evaluated by utilising the 5-layer model (Figure 4-7) with a 5-mm base cell size mesh. It was determined that the Standard k-ε turbulence model

was superior. The Standard k-ε simulation converged within 400 iterations and all the residuals were reduced by four orders in magnitude. This was followed by reducing the base cell size to 4 mm, which resulted in similar behaviour with convergence in 800 iterations. The Standard k-ε model was therefore used for further analyses on the full, 15-layer model.

4.4.3.2 Temperature extraction methods

Hitherto line probes have been used to extract temperature profiles from simulations, whereas Preller (2011) used plane sections. The latter requires a great deal of post-processing in spreadsheets as mentioned earlier. Both extraction methods have adjustable resolutions to determine the amount of data to be extracted, however this does not give the user complete control over the data extraction positions. Consequently, more refined extraction methods were preferred.

Refined extraction methods required the thermocouple coordinates to be known. The Cartesian coordinates of the thermocouples are unavailable in literature. Therefore, the radial coordinates that are presented in Kgame (2010) had to be converted to Cartesian coordinates. This was done by examining Figure 3-14 along with the radial coordinates and the BETS 0.36 centroid data. It was determined that the thermocouples were positioned at a near-constant distance of approximately 17.4 mm from both sides of the centre y-line. The y-coordinates were subsequently fixed which allowed the x-coordinates to be computed from the radial coordinate data.

The three refined extraction methods that were considered are point probes, cylindrical sections, as well as spherical sections. These methods give the user more control over data extraction positions and require the least amount of spreadsheet post-processing. Nevertheless, it is time consuming to create a probe or section for each thermocouple and therefore macros were used to enhance simulation efficiency. It was initially determined that the point probe and spherical section extraction methods were superior which consequently eliminated any further use of the cylindrical section method.

In a discussion with the BETS design engineer, Kgame (2010) noted that an axial tolerance of 5 mm in the thermocouple coordinates is reasonable. No remarks were given on the radial tolerance. Subsequently, the spherical sections were constructed in such a manner that their

centroids corresponded to the calculated Cartesian coordinates of the thermocouples. Furthermore, their radii were set to 5 mm, thereby accounting for both axial and radial deviations. The temperature profiles were compiled by extracting the minimum and maximum temperatures within each spherical section. Preller (2011) conducted a similar study in which only a radial deviation was accounted for. Large temperature gradients were observed in both studies. This was especially true for pockets near the radial centre of the bed wherein the tips of the thermocouples were located, which resulted in temperature differences of up to 10°C. The scattered data made the point probe extraction method more appealing to be used henceforth.

4.4.3.3 Results and discussion

Following the turbulence model assessments and evaluation of temperature extraction methods, the mesh independency study could finally be conducted. The temperature profile for each base cell size is plotted in Figure 4-8.

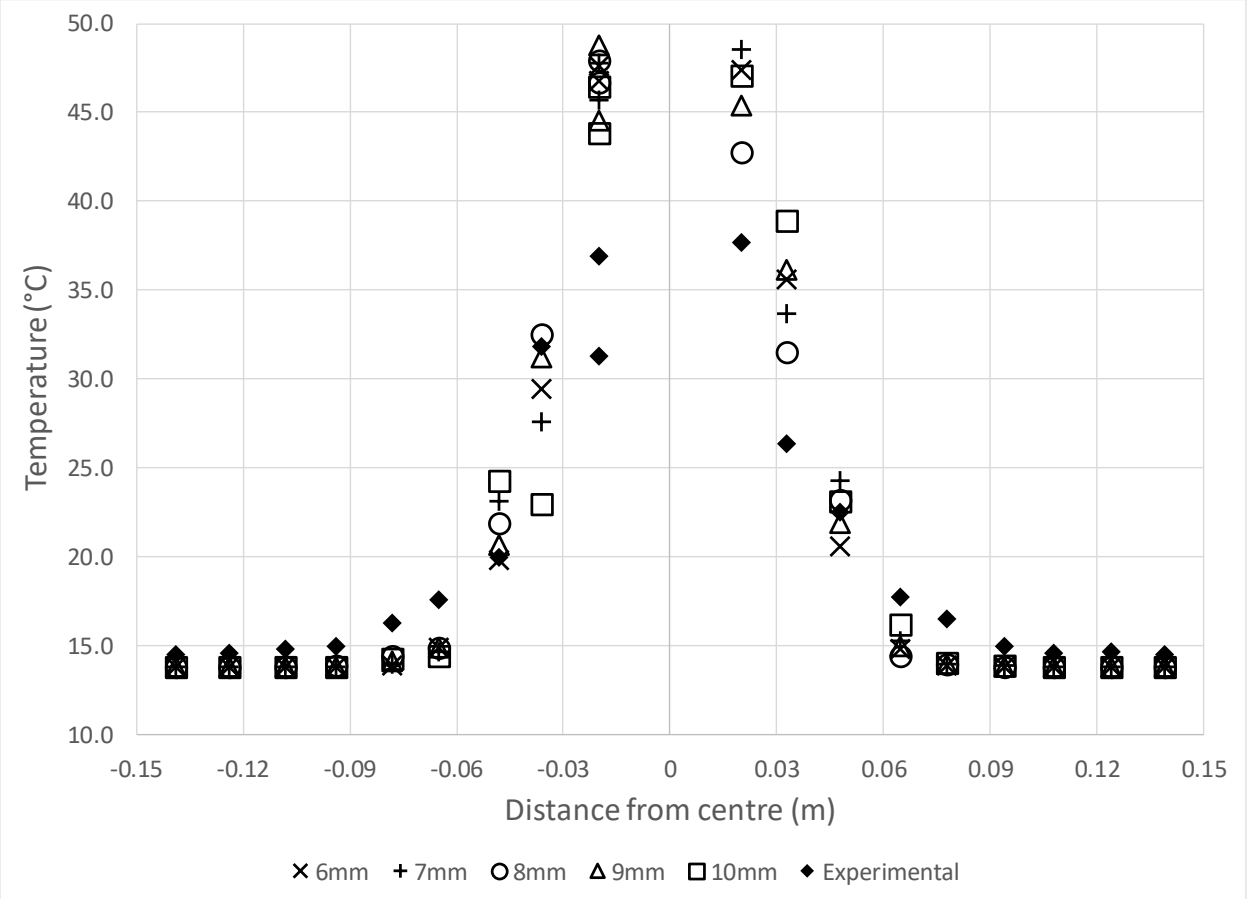

Figure 4-8: Mesh independency study temperature profiles

The mesh independency study was initiated with a base cell size of 10 mm. Afterwards, B was systematically decreased until a threshold value of 6 mm was reached. It was impossible to converge simulations with a B smaller than 6 mm. In addition, the large temperature gradients and rapidly oscillating flow field increased the difficulty of obtaining a mesh independent solution at each temperature point. Consequently, the temperatures at certain points failed to converge to a single value with decreasing B. Both Preller (2011) and Van der Merwe (2014) used the pressure drop over the packed bed as mesh independency metric. Pressure drop appears to be an improved measure of overall convergence. Therefore, it is recommended for subsequent mesh independency studies that the total pressure drop over the packed bed should be as an alternative to the radial temperature profile.

4.4.3.4 Methodology remediation

Following the difficulties in the mesh independency study, the methodology was adapted to firstly converge the simulation and secondly to yield improved results. The threshold B was overcome by using mesh refinement in the packed region of the bed. The cell growth rate and volume ratios in the refined region were indirectly reduced by using a reduced target cell size. This was done to improve both the stability and accuracy of the simulation. The minimum and target cell sizes were set to $0.20B$ and $0.25B$, respectively. In addition, it was preferred to use the previously considered total prism layer thickness of 0.7 mm. Hence, the relative prism layer thickness was set to $0.175B$ based on a B of 4 mm. Thicker prism layers with a total thickness of $0.7B$ were used in the non-refined or global region of the bed. These simulation settings resulted in a volume mesh with 29.1 million cells.

Additional turbulence model assessments followed the refined mesh settings. The test included the use of both steady and unsteady k-ε and k-ω models with their variants, along with DES coupled with the Elliptic Blending k-ε and SST Menter k-ω models, as well as LES. The Eddy viscosity models displayed apparent difficulty in resolving turbulence on the refined mesh, which made DES and LES more attractive for these meshes. Nevertheless, the radial temperature profiles produced by LES generally displayed improved agreement with the experimental temperature data, especially in the near radial centre region of the bed, where the temperatures were commonly overpredicted by other models. LES was therefore considered to be most suitable turbulence modelling approach and subsequently used henceforth.

Following the selection of LES over other turbulence modelling approaches, a brief subgrid scale (SGS) model study was conducted. Previously, Preller (2011) utilised the WALE SGS model. In this study, three SGS models have been considered. This includes the WALE, Smagorinsky and Dynamic Smagorinsky models. The Smagorinsky model yielded the most accurate radial temperature profile when comparing the results with that of the BETS experiments. This was achieved even though the Smagorinsky constant (C_s) was left unchanged at 0.1. Hassan (2008) determined C_s to be 0.18 for certain packed beds. The Dynamic Smagorinsky model appeared to be too aggressive in computing local time-varying values for C_s. Damping functions were not investigated.

The final aspect of the remediation investigated wall treatment since walls initiate vorticity, which require near-wall phenomena to be computed with reasonable accuracy (Section 2.3.4). The newly established mesh settings resulted in y^+ values that were situated in the buffer region. It was attempted to move these values into the log-law layer by increasing the prism layer thickness to the base cell size since wall effects and wake development are not of importance to this study. Nonetheless, it was impossible to increase y^+ values beyond 30. The prism layer thickness was therefore reduced to move the y^+ values into the viscous sublayer as a final remedy. This was done by decreasing the total prism layer thickness in the global and locally refined regions to $0.1B$ and $0.025B$, respectively. The decreased prism layer thickness increased the number of cells from 29.1 to 33.4 million, which was still lower than the original 37 million cell mesh that excluded prism layers.

The resulting polyhedral volume mesh with its prism layers is displayed in Figure 4-9, Figure 4-10 and Figure 4-11. The first figure represents an axial, y,z-plane section of the volume mesh, whereas the second figure displays a lateral, x,y-plane section thereof. The slow cell growth rates that result in a near-uniform mesh are clear from both images.

Figure 4-11 displays a zoomed-in image of the lateral plane section (Figure 4-10) in a region where the spheres are in close proximity. The volume ratio for both the polyhedral and prismatic layer cells has been affected slightly. Nevertheless, the number of polyhedral cells between the two sets of prism layers on each sphere surface has been increased from 3 to 5, which contributes to reduced scalar gradients between adjacent cells and consequently increased simulation accuracy.

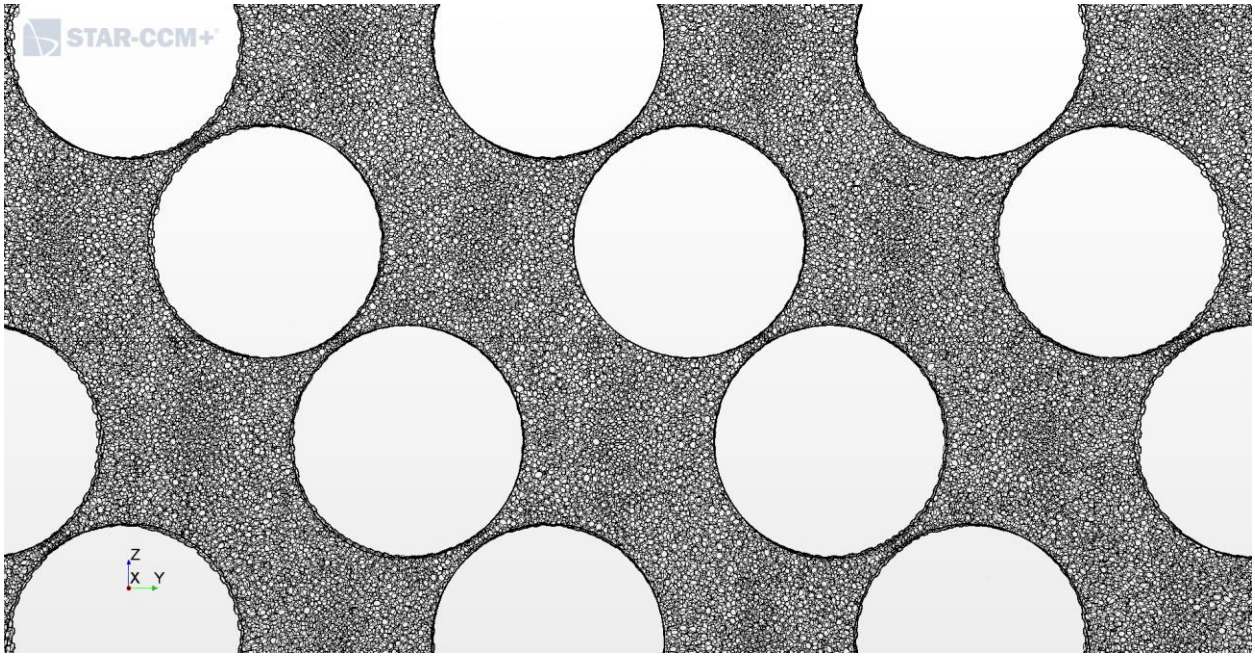

Figure 4-9: Axial plane section of volume mesh

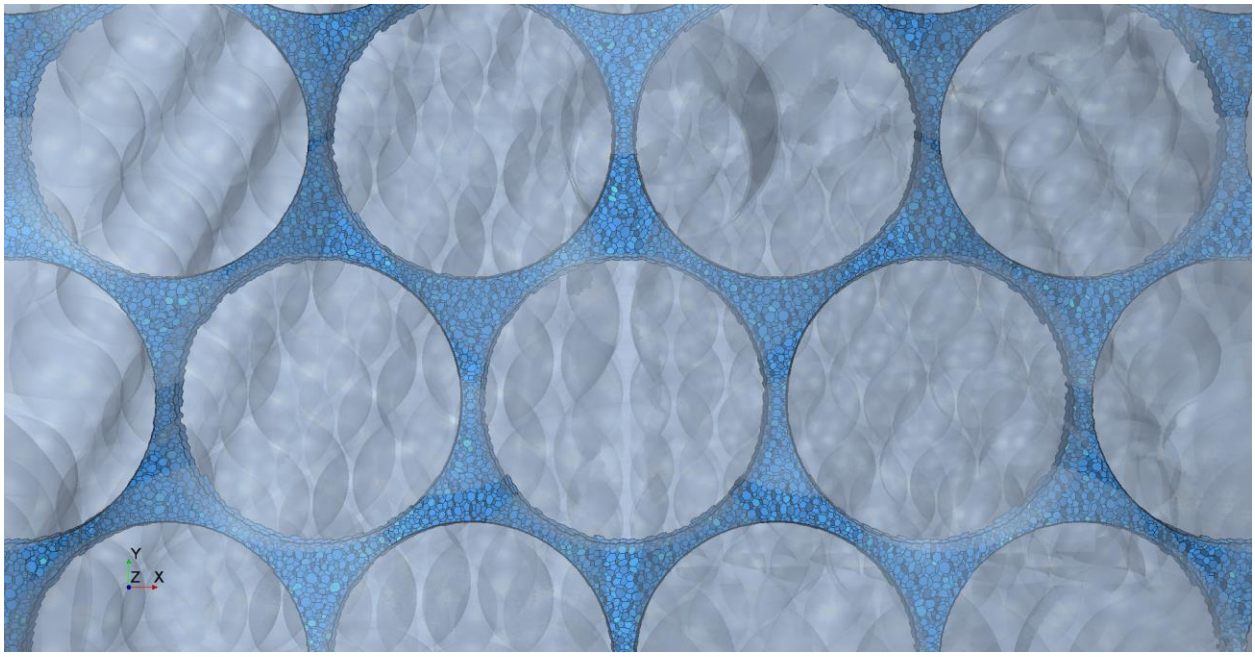

Figure 4-10: Lateral plane section of volume mesh

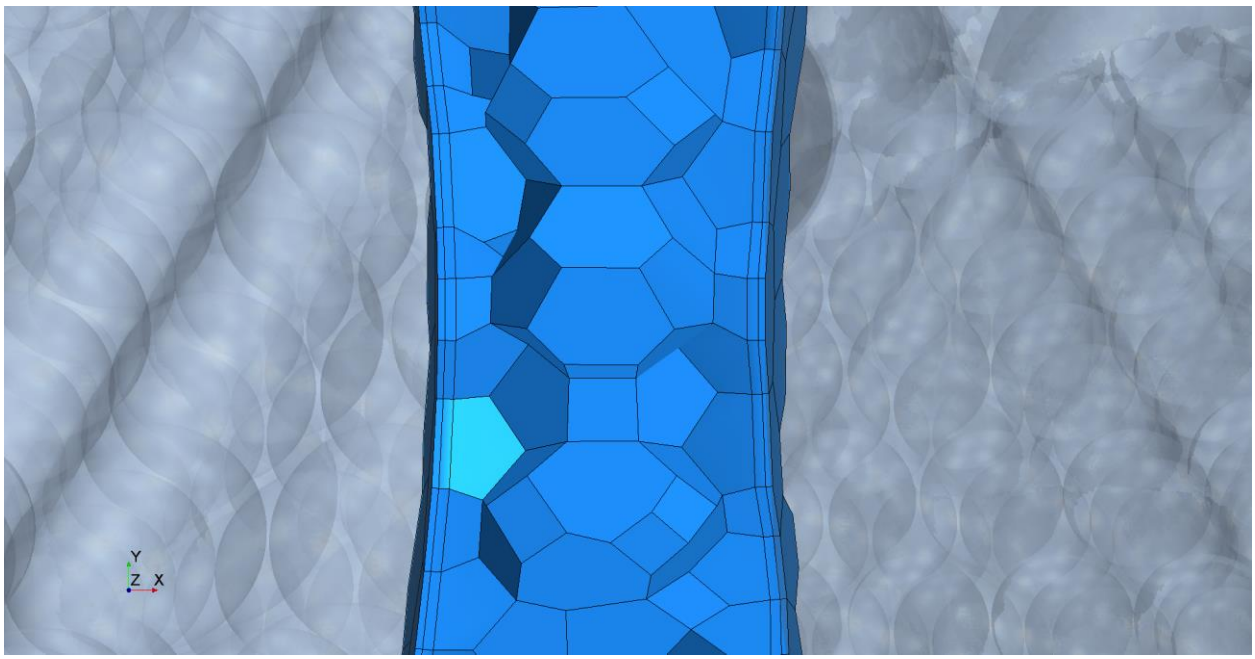

Figure 4-11: Horizontal plane section of volume mesh in close proximity region

The Low y^+ wall treatment model could subsequently be used, which decreased the mass flow-averaged (MFA) y^+ value in packed region to 0.79, with a maximum value of 2.18. Furthermore, the wall treatment model resulted in increased agreement between simulated and experimentally measured temperature profiles. Lastly, it was justified that the refined 4-mm base cell size mesh should produce a mesh independent solution given that it is similar to that of Preller (2011) in several aspects. This mesh was therefore used in subsequent parts of the methodology development. It should be noted that in general LES terms, the mesh has a low resolution, nevertheless this study did not investigate small-scale or microscopic thermal-hydraulic phenomena.

4.4.4 Simulation stability

The implicit unsteady solver was used since LES is an inherently transient technique. This solver requires the time step size, as well as the maximum allowable number of inner iterations for each time step to be specified. The number of inner iterations should be sufficient for all the residuals to smooth out during each time step. This is illustrated in Figure 4-12. From the figure it is evident that the continuity equation requires many inner iterations for each successive time step. The constant number of inner iterations was therefore set to 25 prior to initialisation.

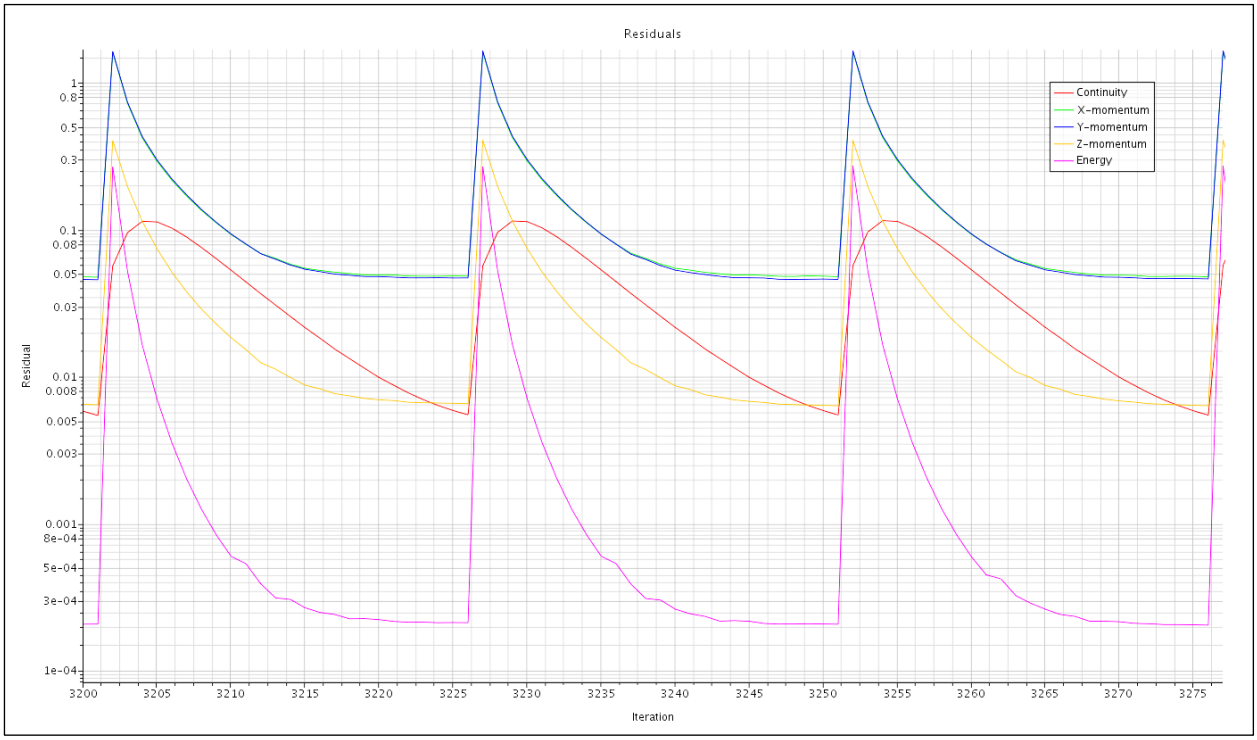

Figure 4-12: Residual plot illustrating inner iterations

It is good practice to reduce residuals by three orders in magnitude. However, this is not always possible, especially in the case of continuous and rapid lateral mixing. The resulting x, y-momentum residuals (lateral) are consequently considerably larger than that of z-momentum (axial). It was previously determined that a reduction in the velocity solver for segregated flow's URF significantly decreases the residuals. Nevertheless, the aim was to develop an efficient and universal methodology, therefore URFs were not considered in the methodology development. The residuals were indeed systematically reduced by decreasing the time step at certain numbers of iterations. A general outline of this manual reduction process is presented in Table 4.4.

The flow field was firstly allowed to develop by using a large time step for the first 1000 iterations or 40 time steps. Thereafter, the reduction process was initiated with large time step reductions, followed by smaller reductions with the approach of the millisecond range. The final time step size was equated to the largest time step that satisfied the Courant-Friedrichs-Lewy (CFL) stability condition, which is given by (Wilcox, 2006):

$$C = \frac{u\Delta t}{\Delta x} < 1 \tag{4.1}$$

where C is the dimensionless Courant number, u is the fluid velocity (m/s), Δt is the size of the time step (s) and Δx is the cell size (m). Both u and Δx are fixed in this case, making Δt the only user-controlled variable by which $C \leq 1$ can be achieved. A $C = 1$ ensures that the flow moves from one cell centroid to that of the next adjacent cell in one time step, which increases stability. The final time step was therefore chosen in such a manner that the resulting MFA convective Courant number in the packed region of the bed was as close as possible to one. Since a fixed mesh was used for all Re_{total}, the introduction of the CFL stability condition accounted for the resulting differences in u by determining the final corresponding Δt, which increased the universality of the methodology.

Table 4.4: General outline of the time step reduction process

Iteration		Time step size (s)
Initial	Final	
0	1000	1.000
1000	1100	0.500
1100	1200	0.100
1200	1300	0.070
1300	1400	0.040
1400	1500	0.010
1500	1600	0.008
1600	1700	0.006
1700	1800	0.004
1800	1900	0.002
1900	2000	0.001
2000	3000	CFL satisfying time step

4.4.5 Convergence criteria

In addition to ensuring stability, it was ensured that the simulations were converged by monitoring MFA temperatures over eight lateral plane sections at different axial positions as displayed in Figure 4-13. Centroid thresholds were used to display a quarter of the cross-sectional area. Furthermore, the plane sections were located at the inlet, at each 100 mm axial increment thereafter and finally at the outlet. The thermocouple coordinates are depicted as point probes. Successful convergence was achieved when the MFA temperatures on all the planes converged to the single MFA temperature calculated over both inlets. This was since constant inlet conditions

were used along with the specification of adiabatic walls. The methodology development is hereby concluded.

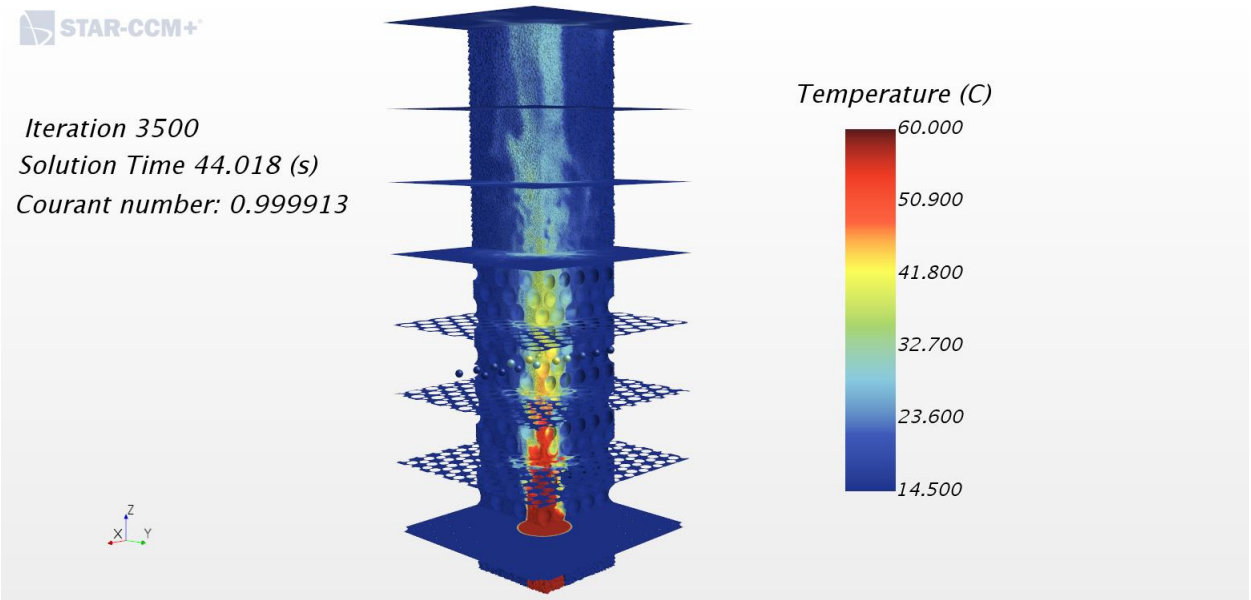

Figure 4-13: Plane section temperatures

4.4.6 Methodology verification

The methodology verification followed its successful development. A summary is firstly presented to clarify the resulting simulation setup that was formulated prior to the discussions on stability and convergence.

4.4.6.1 CAD model

The final CAD model with its corresponding dimensions is depicted in Figure 4-14 (a), whereas the cross-sectional view of the braiding gas inlet configuration is represented by Figure 4-14 (b). In the former figure, the inlet and outlet domain lengths, upstream and downstream of the bed, are $3.6d_p$ and $12.0d_p$, respectively. In the latter figure, both the inner and outer diameters of the braiding gas pipe are displayed. The blue region represents a segment of the cold gas inlet domain.

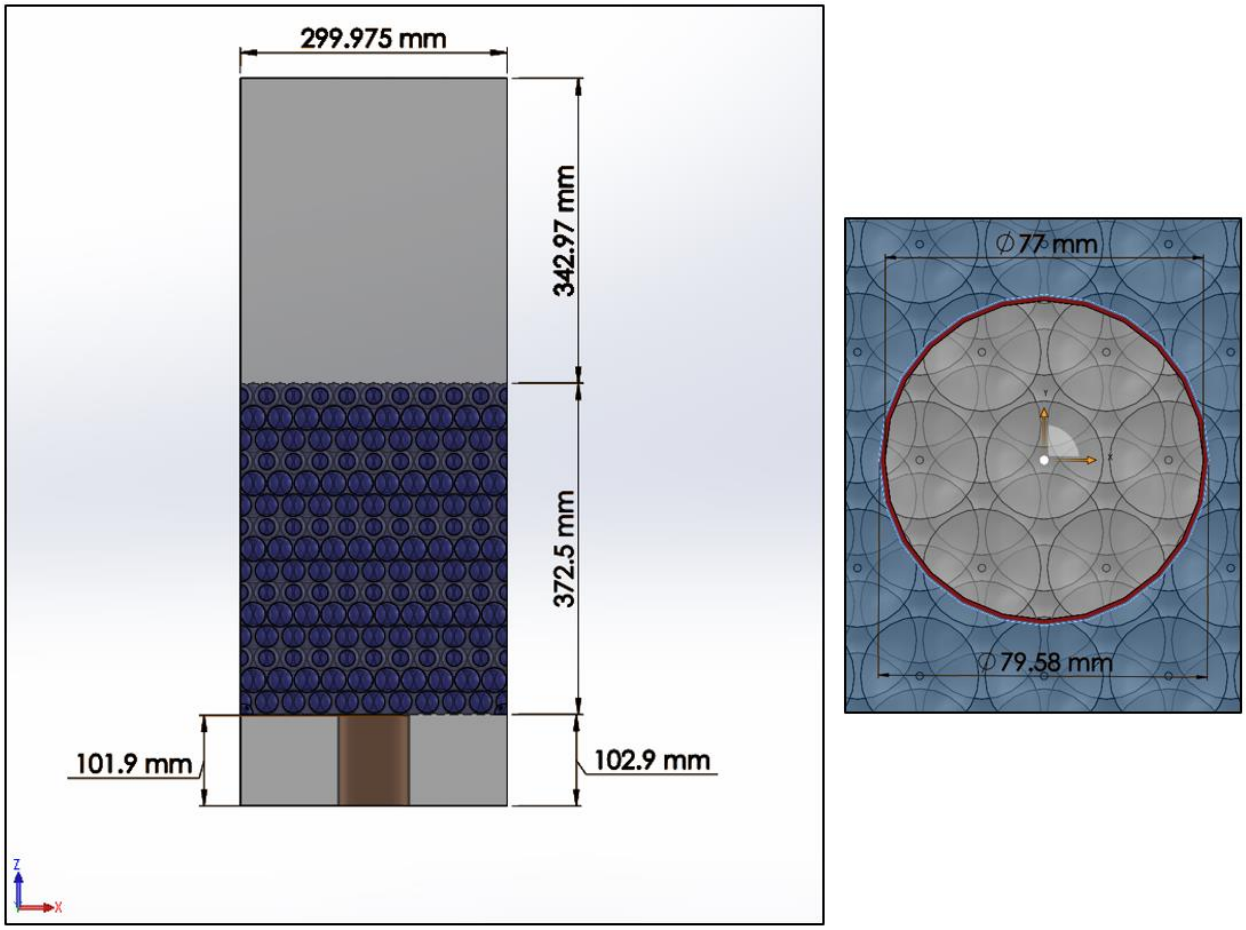

Figure 4-14: BETS CAD model configuration: (a) Axial perspective; (b) Braiding gas inlet

4.4.6.2 Mesh continua

Three meshing models were used, which included a surface remesher, polyhedral mesher and prism layer mesher. Furthermore, the surface remesher was not allowed to create aligned meshes and topological modification was prevented by setting the minimum face quality to zero. Additional mesh settings are summarised in Table 4.5. As discussed earlier, two mesh continua were set up. The first corresponded to the global region, while the second, refined mesh continuum was associated with the packed region of the bed. The sensitivity of the number of cells to the base cell size is indicated in the table. It is evident that the cell count increases exponentially when decreasing the base cell size. The previous justification that the 4-mm base cell size mesh should produce a mesh independent solution was investigated by also simulating the refined 3.5-mm base cell size mesh. Although the creation of the 180 million cell mesh, which is associated with a 2.0 mm base cell size, was successful, the simulation thereof seemed unreasonable.

Table 4.5: Summary of final mesh settings

Region	Parameter	Value		
Global	Tessellation density	Fine		
	Base cell size (B)	4.0 mm	3.5 mm	2.0 mm
	Number of cells (million)	33.4	57.8	180
	Total prism layer thickness	$0.10B$		
	Surface curvature	72 points per circle		
	Minimum cell size	$0.25B$		
	Target cell size	$1.00B$		
	Polyhedral mesh density	1.2		
	Polyhedral mesh growth factor	0.85		
Refined (packed)	Minimum cell size	$0.20B$		
	Target cell size	$0.25B$		
	Total prism layer thickness	$0.025B$		

4.4.6.3 Physics continuum

A single physics continuum was used for the entire simulation domain. The continuum attributes with their corresponding configurations are summarised in Table 4.6. Material properties that were held constant include dynamic viscosity, specific heat, as well as thermal conductivity.

Table 4.6: Physics continuum attributes

Attribute	Configuration
Space	Three dimensional
Time	Implicit unsteady
Material	Gas (N_2)
Flow	Segregated flow
Energy	Segregated fluid temperature
Gradient metrics	Gradients
Equation of state	Ideal Gas
Viscous regime	Turbulent
Turbulence	Large Eddy Simulation
Subgrid scale turbulence	Smagorinsky subgrid scale
LES wall treatment	Low-y^+ wall treatment
Wall distance	Exact wall distance

Wall shear stress specification	No-slip
Wall thermal specification	Adiabatic

Boundaries were created for the cold and hot inlets, the surface of the braiding gas pipe, the spheres (treated as walls), the four walls, as well as the outlet. Both inlets were specified to be velocity inlets by the method of magnitude and direction. The braiding gas pipe, spheres and walls were specified as walls with their corresponding attributes presented in Table 4.6. The outlet was specified to be a pressure outlet with a constant gauge pressure of zero, while the static temperature was set equal to the temperature field function should reverse flow occur on the outlet faces.

The simulation temperatures were bound between 11.0 and 60°C, which corresponded with that of Preller (2011). Furthermore, the initialisation temperature (T_0) and velocity vector ($\boldsymbol{u_0}$) were set to 15°C and $< 0, 0, 0 >$ m/s, respectively. Following the uncertainty analysis of Kgame (2010), as discussed in Section 3.3.1, the measured inlet conditions were averaged over the four experimental runs for each Re_{total} and used as CFD input. For the 3000 Re_{total} case, the absolute inlet pressure was 300.6 kPa, with cold and braiding gas inlet temperatures of 13.8 and 57.5 °C, respectively. The superficial velocity for each inlet was 0.52 m/s, as recalculated from the measured mass flow rates. This concludes the summary of the simulation setup.

4.4.6.4 Results and discussion

The resulting temperature profiles from both the 4-mm and 3.5-mm base cell size simulations are represented by Figure 4-15. Good agreement has been achieved between the simulated and experimentally measured temperature profiles. Although the meshes differ by over 24 million cells, the finer mesh results in slightly improved agreement with experimental data. This is clear when considering their mean squared errors (MSEs) of 10.05°C^2 and 9.23°C^2 for the 4-mm and 3.5-mm base cell size meshes, respectively. Furthermore, by considering the large difference in the number of cells, along with Equation 2.28 wherein the LES filter cut-off width (Δ) is dependent on the volume cell dimensions, as well as small difference in the resulting MSEs, the 4-mm base cell size mesh is reasoned to be mesh independent. The simulation methodology is hereby verified for a Re_{total} of 3000 and can subsequently be used to validate the remaining BETS experimental temperature data sets.

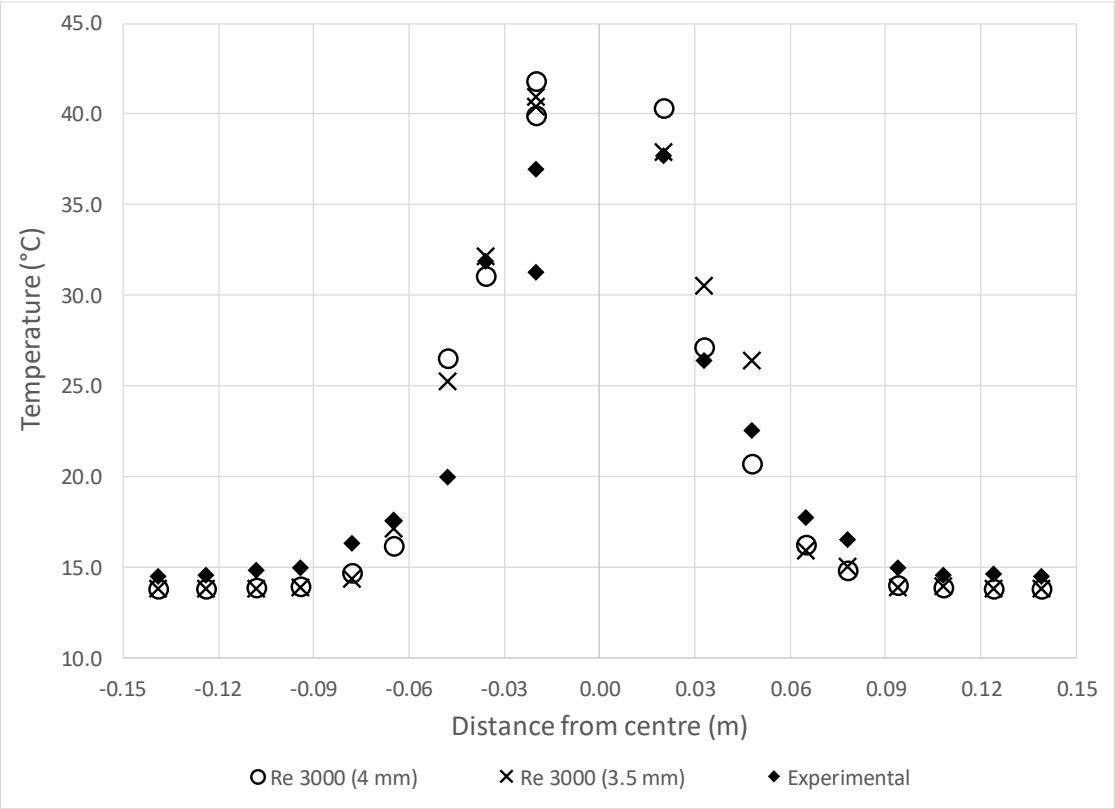

Figure 4-15: Methodology verification temperature profiles

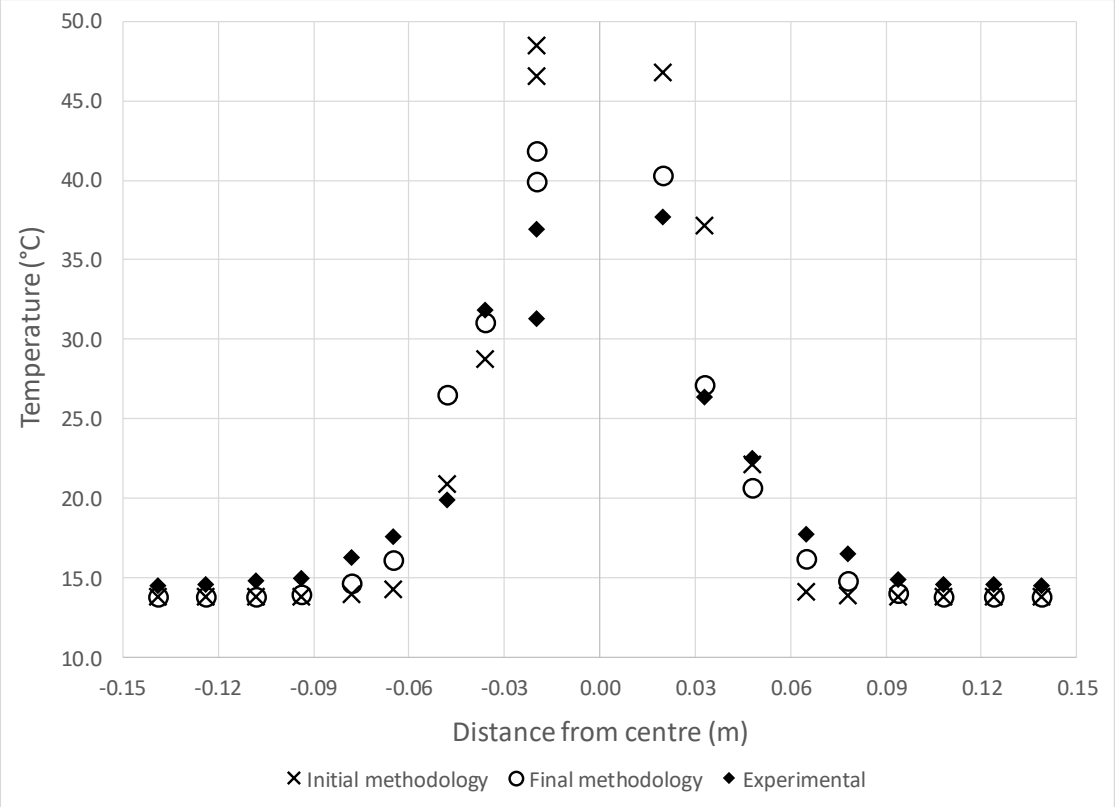

Figure 4-16: Methodology improvement evaluation

Lastly, the line probe results from the initial full model simulation are represented by Figure 4-5. These results have been converted to correspond to the point probe temperature extraction method for improvement evaluation purposes. The evaluation results are displayed in Figure 4-16. It is clear that the agreement between the simulated and experimentally measured temperatures has been improved significantly. This is also certain when comparing the MSEs. The initial methodology had a MSE of 33.6°C^2, whereas the final methodology had a MSE of 10.1°C^2. This also proves that the point probe extraction method is extremely sensitive in comparison to the line probe extraction method.

4.5 Summary

This chapter verified the BETS simulation conducted by Preller (2011), where after different approaches of symmetrical and periodic boundary conditions were evaluated. A detailed simulation methodology has been developed by conducting a comprehensive set of CFD analyses. In addition, appropriate stability conditions and convergence criteria have been developed and integrated into the methodology. The methodology has subsequently been verified and proven to be superior over previous methodologies. The final simulation methodology is therefore considered to be suitable for validating other selected sets of BETS experimental temperature data.

CHAPTER 5: CFD VALIDATION OF SELECTED BETS EXPERIMENTS

5.1 Introduction

In the previous chapter, a detailed simulation methodology has been developed, which was based upon a Re_{total} of 3 000. This methodology was assumed to be directly applicable for simulating larger Re_{total} BETS 0.36 experiments and was therefore used to validate a selected set of experimental temperature data.

5.2 Simulation setup

This section will briefly discuss the simulation setup that corresponded to each Re_{total}. Henceforth, all Reynolds numbers in this chapter will refer to Re_{total} as defined in Equation 3.8. The CAD model from Figure 4-14, as well as the mesh continua settings from Section 4.4.6.2, were identical for each simulation. Unless specified otherwise and excluding the inlet conditions, the physics continuum was assembled exactly as discussed in Section 4.4.6.3. The experimental inlet conditions that were averaged over the four experimental runs for each Re_{total} by Kgame (2010) are summarised in Table 5.1. These conditions were used as simulation inputs in the physics continuum, as well as at the corresponding velocity inlets.

Table 5.1: CFD inlet conditions (Kgame, 2010)

Reynolds number	Absolute pressure (kPa)	Temperature (°C)		Superficial velocity (m/s)	
		Cold gas	Hot gas	Cold gas	Hot gas
3 000	300.9	13.8	57.5	0.52	0.52
10 000	1000	13.8	56.8	0.53	0.53
20 000	2001	14.6	57.7	0.53	0.54
30 000	3000	14.9	57.5	0.54	0.54
40 000	3799	15.7	56.6	0.57	0.57

Two simulations slightly deviated from the universal methodology. This includes the use of the WALE SGS model at a Re_{total} of 10 000, as well as the utilisation of the modified Soave-Redlich-Kwong (mSRK) equation of state (EOS) at a Re_{total} of 40 000. The former investigated competitive SGS models at increased turbulence, whereas the latter attempted to quantify any deviation from ideal gas behaviour that might occur due to using a moderately high pressure of

38 bar. According to Carlson's (1996) decision tree for property packages, both the Peng-Robinson (PR) and Soave-Redlich-Kwong (SRK) or mSRK EOS are applicable for modelling the real gas behaviour of nitrogen. Nevertheless, the mSRK EOS proved to be superior in a preliminary study and was therefore used in subsequent analyses.

5.3 Results and discussion

Following the simulation setup, the results from the different simulations can subsequently be discussed. This section will firstly review the results from the stability and convergence criteria, which corresponded to Sections 4.4.4 and 4.4.5, thereafter wall treatment will be considered and finally a discussion on the simulated temperature profiles will follow.

5.3.1 Stability and convergence criteria

The residuals were monitored for stability purposes. The final residuals obtained from the different simulations are given in Table 5.2. The residuals share comparable values for similar equations. In addition, the x, y-momentum residuals display increased values which agree with the results from the previous chapter.

Table 5.2: Final CFD residuals

Reynolds number	Iterations	Residuals				
		Continuity	Momentum			Energy
			X	Y	Z	
3 000	3,001	0.014	0.050	0.047	0.008	0.0004
10 000 (WALE)	3,001	0.009	0.057	0.054	0.008	0.0003
10 000 (Smagorinsky)	3,001	0.008	0.054	0.051	0.006	0.0002
20 000	3,500	0.006	0.048	0.048	0.006	0.0002
30 000	3,501	0.005	0.054	0.052	0.007	0.0002
40 000 (Ideal Gas)	3,001	0.005	0.041	0.039	0.006	0.0002
40 000 (mSRK)	3,552	0.004	0.048	0.048	0.007	0.0002

The increased number of iterations in certain simulations result from using additional time step increments to satisfy the CFL stability condition (Equation 4.1). The final time steps with their corresponding MFA Courant numbers for the refined mesh regions are presented in Table 5.3.

Table 5.3: Courant numbers

Reynolds number	Time step (ms)	Courant number
3 000	2.0	1.07
10 000 (WALE)	1.0	1.04
10 000 (Smagorinsky)	1.0	1.03
20 000	0.7	1.00
30 000	0.7	1.15
40 000 (Ideal Gas)	0.5	0.96
40 000 (mSRK)	0.5	0.94

It is evident from the table that the CFL satisfying time step decreases with increasing turbulence when using identical meshes for each simulation. The simulations are considered to be stable based on the Courant numbers. Excluding general LES applications, the mesh resolution is sufficient for predicting macroscale phenomena judging from the time step sizes. Lastly, for efficiency purposes, it is recommended to compile algorithms for automatic time step control in future simulations.

Simulation stability was simultaneously monitored with convergence. Successful convergence was achieved when the MFA plane section temperatures on all planes converged to the constant MFA temperature taken over both inlets ($\bar{T}_i$). The temperatures were recorded at each consecutive time step. The time step reductions commenced at 41.0 s for all simulations. Nevertheless, the pseudo-steady, sinusoidal behaviour of the monitored temperatures were observed well in advance. Therefore, it can be asserted that the flow fields of all simulations were sufficiently developed prior to the time step reduction process. Since the MFA temperatures displayed sinusoidal or asymptotic behaviour, it was justified that the time-averaged values would give a better representation of convergence or more specifically, the deviation from the corresponding $\bar{T}_i$. The MFA plane section temperatures were subsequently time-averaged over the final 1000 iterations of each simulation. The resulting time-averaged, MFA plane section temperatures are displayed in Table 5.4, with their associated MSEs (based on $\bar{T}_i$) depicted by

Figure 5-1. It is worth noting that the first plane section is located at $z = 0\ mm$, which is situated directly below the first layer of spheres and not at the inlets ($z = -102.9\ mm$) as discussed earlier.

Table 5.4: Time-averaged mass flow-averaged plane section temperatures

Reynolds number	$\bar{T}_i$ (°C)	Time-averaged mass flow-averaged temperatures (°C)							
		0	100	200	300	400	500	600	Outlet
3 000	15.80	15.80	15.77	15.80	15.81	15.64	15.64	15.77	15.80
10 000 (WALE)	15.73	15.73	15.72	15.72	15.68	15.54	15.69	15.83	15.93
10 000 (Smagorinsky)	15.73	15.73	15.73	15.66	15.70	15.53	15.72	15.69	15.86
20 000	16.59	16.59	16.60	16.61	16.67	16.61	16.47	16.61	16.58
30 000	16.86	16.87	16.84	16.80	16.78	16.88	16.90	16.87	16.85
40 000 (Ideal Gas)	17.55	17.55	17.53	17.51	17.53	17.57	17.47	17.41	17.73
40 000 (mSRK)	17.53	17.53	17.49	17.59	17.53	17.38	17.14	17.51	17.50

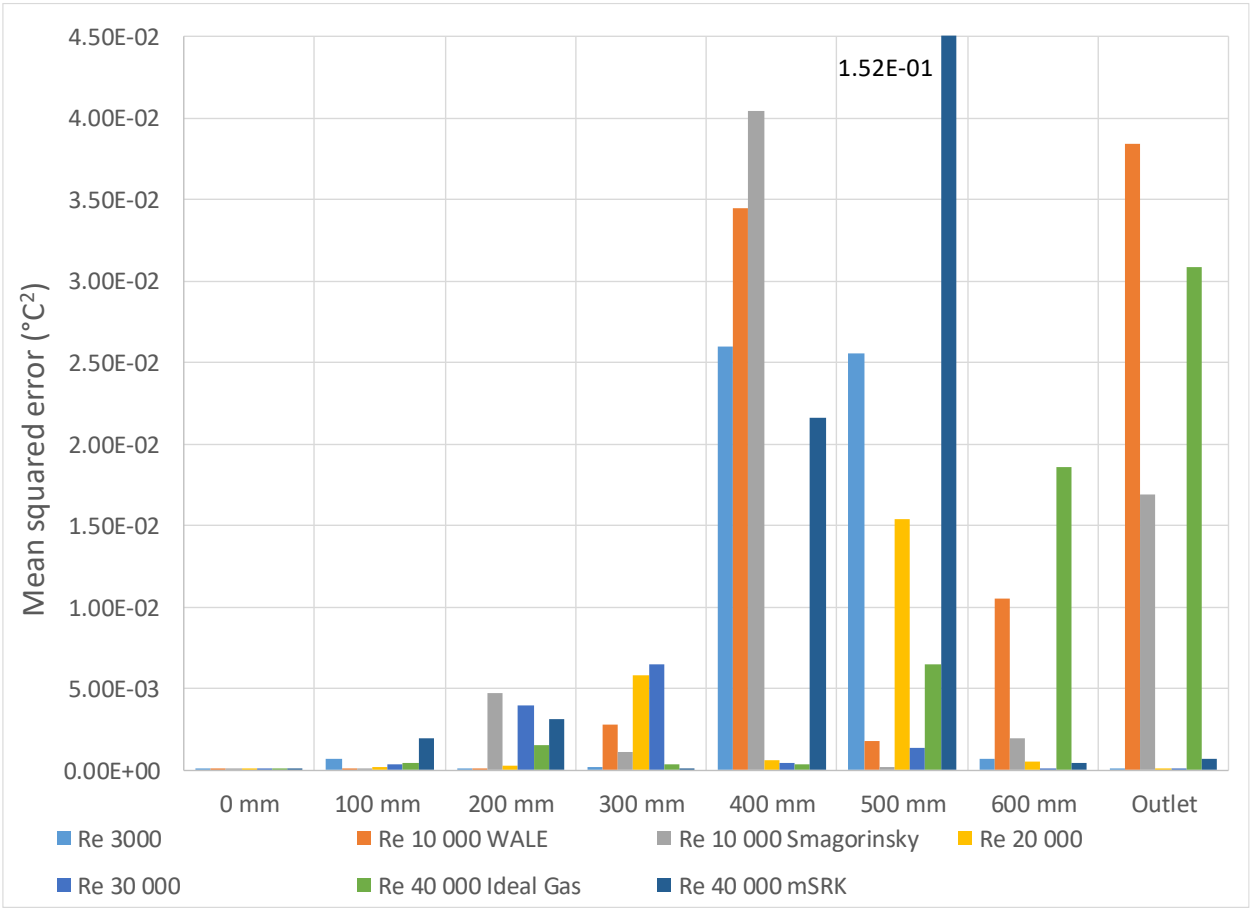

Figure 5-1: Mean squared errors of time-averaged mass flow-averaged plane section temperatures

It is evident from the Table 5.4 and Figure 5-1 that all simulations have been converged successfully, especially in the region where the thermocouples were positioned, which was located between the planes at $z = 200\,mm$ and $z = 300\,mm$. Furthermore, the first temperatures downstream of the packing were measured at $z = 400\,mm$. From this location onward, the reduced flow resistance results in a region with larger eddies and increased turbulence dissipation, which produce larger temperature deviations from $\bar{T}_i$. These phenomena are illustrated by the instantaneous velocity contour plot in Figure 5-3. This concludes the discussion on simulation stability and convergence criteria.

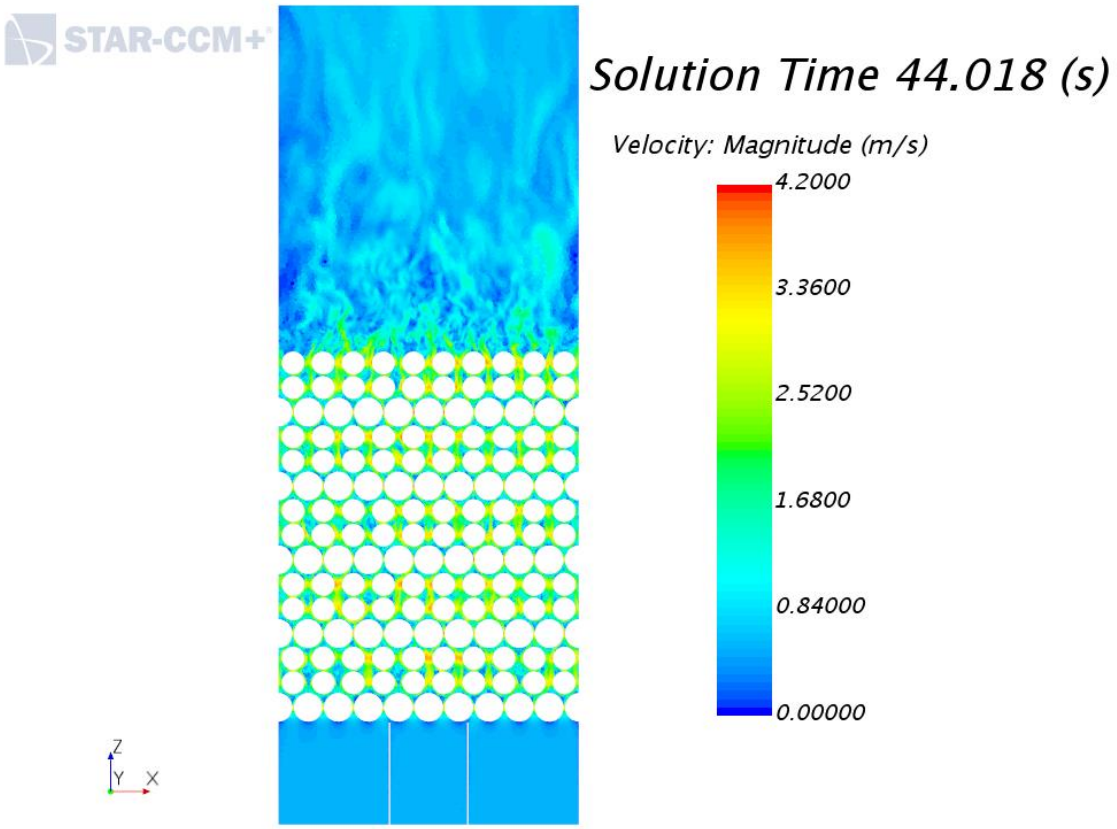

Figure 5-2: Velocity contour illustration (Re 20 000)

5.3.2 Wall treatment

Wall treatment is important in accurately predicting thermohydraulic behaviour in near-wall regions. The aspects of turbulent boundary layers and wall treatment considerations have been discussed in Sections 2.2.4, 2.3.4 and 4.4.3.4. The resulting MFA dimensionless wall distances

along with their maximum values in the packed or refined mesh regions are presented in Table 5.5.

Table 5.5: Dimensionless wall distances

Reynolds number	Dimensionless wall distance		ν (μm²/s)
	MFA	Maximum	
3 000	0.79	2.18	5.10
10 000 (WALE)	2.11	5.24	1.53
10 000 (Smagorinsky)	2.16	5.24	1.53
20 000	3.76	8.05	0.77
30 000	5.03	10.53	0.51
40 000 (Ideal Gas)	6.20	12.07	0.41
40 000 (mSRK)	6.13	12.26	0.41

The dimensionless wall distance increases with turbulence when identical meshes are used. Furthermore, it is known that increasing turbulence results in a reduced turbulent boundary layer thickness. This can also be understood from a mathematical perspective by comparing Equation 2.15 with Equation 2.18. These effects have not been accounted for since the methodology development was exclusively based on a Re_{total} of 3 000, which resulted in a constant MFA normal wall distance of 20 μm for all simulations. In addition, the linear relationship between the dimensionless wall distance (y^+) and velocity (u^+) in Figure 2-2 can be considered to apply for values of up to $y^+ = 11$. Simulations with a Re_{total} of 40 000 exceeded this limit. Nevertheless, in the case of the Ideal Gas simulation for example, this occurred in only 0.007% of the cells and therefore these incidents are considered to be insignificant. It can be concluded that the mesh was reasonable and meets the requirements for resolving the viscous sublayer with low-y⁺ wall treatment.

It is also evident from Table 5.5 the MFA kinematic viscosity (ν) varies sharply over the given range of Reynolds numbers. Equation 2.18 shows an indirect proportional relationship between y^+ and ν, which is also clear from the table above. Therefore, the universality of the simulation methodology can be improved by accounting for the increase in y^+ through correlating the prism layer thickness to ν. However, a compromise between sufficient detail and computational resources should also be taken into consideration.

5.3.3 Simulated temperature profiles

The aim of this study was to replicate the BETS experimental setup by means of an explicit numerical evaluation of the thermal dispersion with limited information on the actual flow field. Thermal dispersion was quantified or reflected by the measured radial temperature profiles of the packed bed. The normalised temperature profiles from the BETS experiments required validation. It was therefore required to simulate several temperature profiles that corresponded to the selected Reynolds numbers. The results are displayed in Figure 5-3 to Figure 5-7, with the actual validation being applicable to the ranges of $Re_{total} \geq 10\,000$. The temperature profiles are accommodated with their respective MSEs in Table 5.6. Furthermore, the simulated temperature profile in Figure 5-3 has already been discussed in the previous chapter and is therefore redisplayed (without the 3.5-mm base cell size simulation) for subsequent comparison.

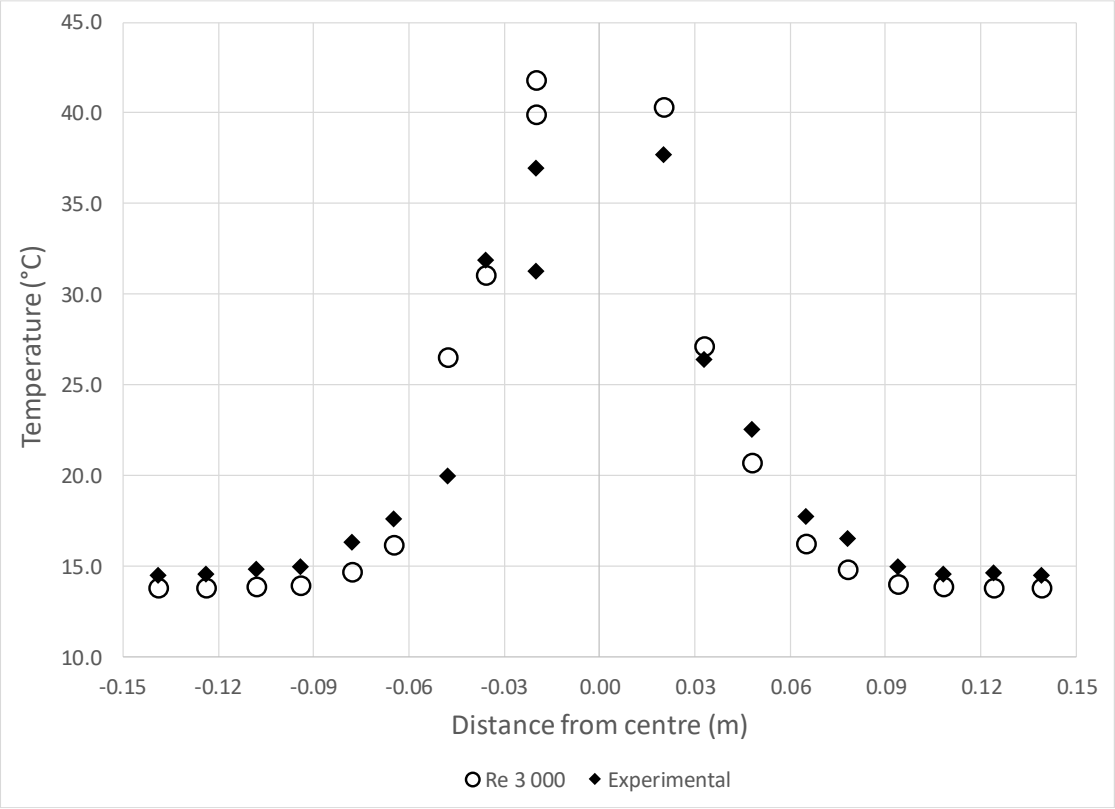

Figure 5-3: Re 3 000 simulated temperature profile

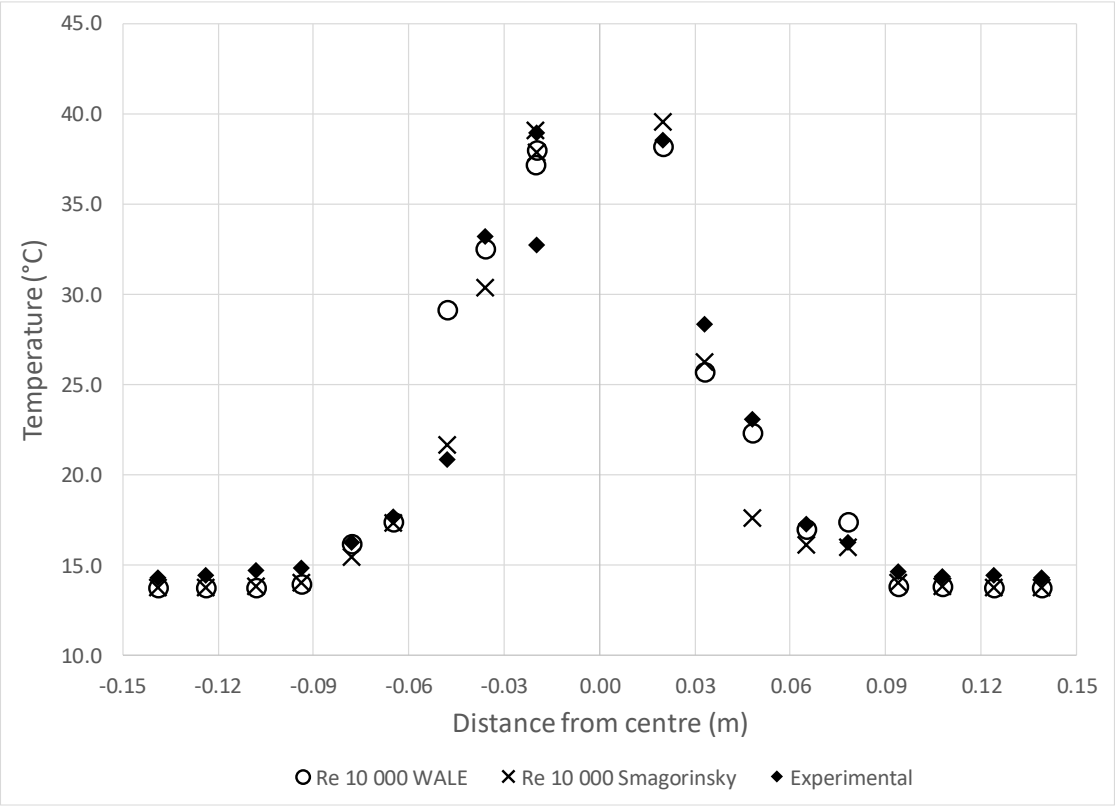

Figure 5-4: Re 10 000 simulated temperature profiles

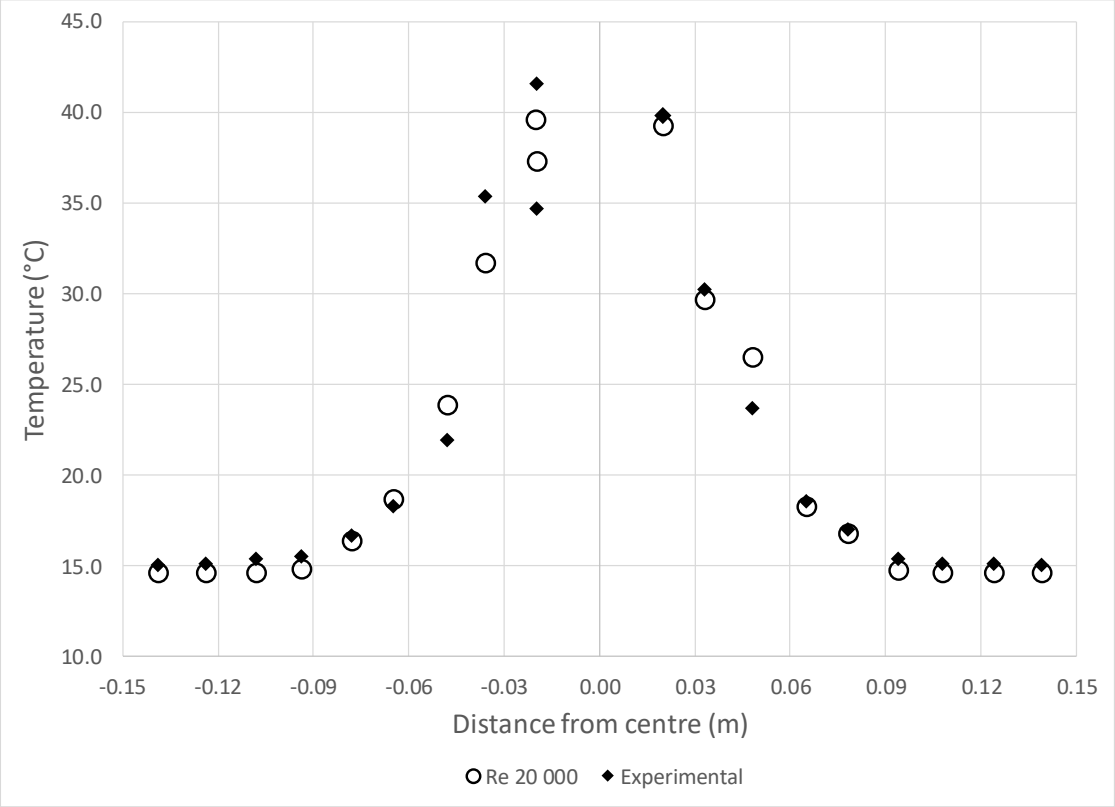

Figure 5-5: Re 20 000 simulated temperature profile

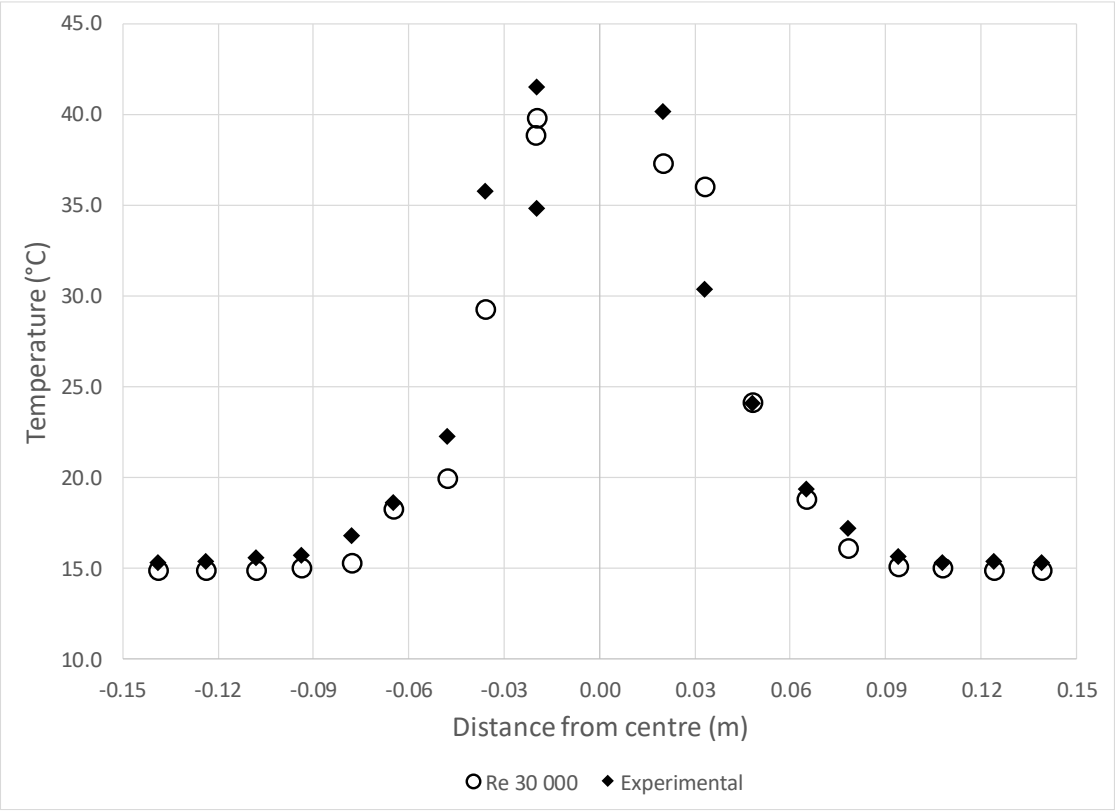

Figure 5-6: Re 30 000 simulated temperature profile

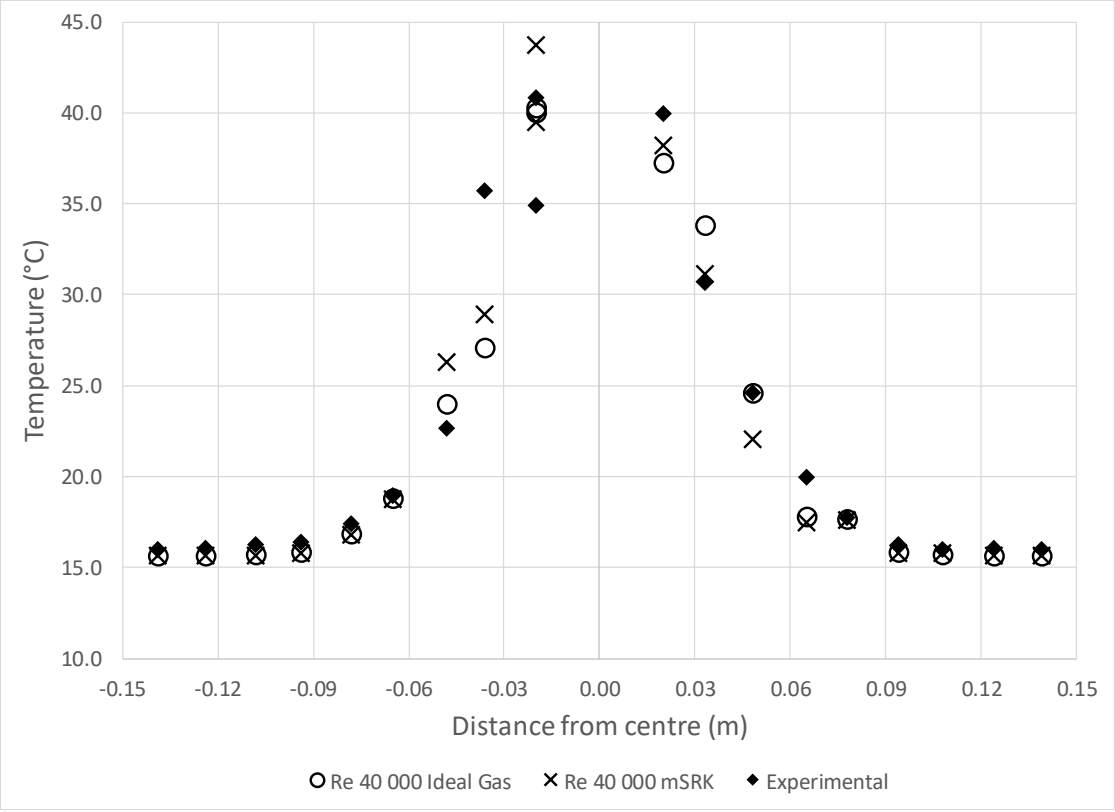

Figure 5-7: Re 40 000 simulated temperature profiles

Table 5.6: Mean squared errors on temperature profiles

Reynolds number	Mean squared error (°C²)
3 000	10.05
10 000 (WALE)	5.93
10 000 (Smagorinsky)	3.96
20 000	2.08
30 000	6.58
40 000 (Ideal Gas)	6.81
40 000 (mSRK)	8.24

It is evident that all the results are in good agreement with the normalised temperature profiles of the BETS experiments. It is hereby simultaneously proven that the STAR-CCM+® simulation methodology is capable of accurately predicting the radial temperature profiles of the BETS 0.36 experiments with $Re_{total} \geq 10\,000$ and that the BETS experimental temperature data for the selected cases are valid.

Following the extended methodology verification and data validation, it is noted although the methodology was based on a Re_{total} of 3 000, that this simulation had the largest deviation from experimental data according to the MSEs presented in Table 5.6. Nevertheless, exact conclusions cannot be drawn. Furthermore, the performance of different SGS models at higher turbulence is comparable. The Smagorinsky model displayed slightly improved agreement with experimental data over the WALE model and was consequently used in subsequent simulations. In addition, the 20 000 Re_{total} simulation demonstrated the best agreement with experimental data and had the highest stability according to the Courant numbers (Table 5.3) among the other simulations. The 30 000 Re_{total} and 40 000 Re_{total} simulations exhibit increased MSEs that are equivalent. This suggests that the methodology provides exceptional performance for the Re_{total} range between 10 000 and 20 000. Lastly, the 40 000 Re_{total} simulations display comparable results. Nevertheless, the results reflect a preference towards ideal gas behaviour. Accommodating for real gas behaviour greatly increases the complexity of a simulation. According to the VDI Heat Atlas (Verein Deutscher Ingenieure, 2010), the compressibility factor (Z) for nitrogen at the corresponding temperatures and pressures is approximately one, which eliminates the necessity for using more sophisticated equations of state.

The abovementioned results correspond to instantaneous temperatures that were extracted at small time steps, which followed an excessive number of turnovers after satisfying the CFL condition. Nevertheless, it is recommended for future simulations to use time-averaged results instead of instantaneous results.

5.4 Summary

It was required to validate a selected set of BETS experiments by using the previously developed simulation methodology. The resulting residuals, Courant numbers and plane section temperatures of the different simulations have been discussed. This was followed by a discussion on and comparison between the simulated temperature profiles. It was verified that the simulation methodology is capable of accurately simulating the radial temperatures in a packed bed, along with the simultaneous validation of a selected set of BETS 0.36 experimental temperature data.

CHAPTER 6: CONCLUSIONS AND RECOMMENDATIONS

6.1 Research aim and objectives

The aim of this research was to evaluate the thermal dispersion results of the BETS experiments numerically. This was to be done by firstly constructing structured pebble beds that are representative of the experimental setup, followed by the verification of Preller's (2011) work with an accompanying residual analysis. A symmetry evaluation study was subsequently required. Thereafter, it was essential to develop a suitable and universal simulation methodology along with stability conditions and convergence criteria. Finally, the methodology was to be used to evaluate the BETS experimental normalised temperature profiles to accomplish the aim of this study.

6.2 Conclusions

The construction of several structured packed beds, that are representative of the BETS experimental setup, has been successful. The simulation setup, general simulation procedure and simulated temperature profiles of Preller (2011) has been verified. Furthermore, a successful, preliminary simulation methodology has been developed through residual analyses, which resulted in residuals with decreased magnitude and increased stability. The results from the symmetry evaluations led to the conclusion that both symmetry and periodic boundary conditions affect the simulated temperature profiles and that is its necessary to simulate the full cross-sectional area in the evaluation of increased thermal dispersion.

The optimised results from the mesh quality analyses displayed significant improvements in the number of cells, the overall cell quality and the volume ratio when compared to previous work. From the results of the mesh independency study, it can be concluded that mesh refinement is essential for simulating packed beds with a large number of spheres due to simulation difficulties that arise from using meshes with an excessive number of volumetric cells. It was further concluded that the point probe temperature extraction method was superior to previous methods. It was additionally determined that large eddy simulation with the Smagorinsky SGS model and low y^+ wall treatment was the most suitable turbulence modelling approach. It can subsequently be concluded that sufficient inner iterations, systematic time step reduction and satisfaction of the CFL condition result in increased simulation stability. It can also be concluded that by monitoring MFA temperatures over several lateral plane sections is effective in determining convergence. Lastly, it was concluded that the final simulation methodology displayed substantially improved

agreement with the normalised 3000 Re_{total} experimental temperature data over previous simulation approaches.

In the validation study, it was concluded that the improved simulation methodology can be used to accurately predict the radial temperature profiles over the complete set of BETS 0.36 experiments. In addition, it was also confirmed that the assumption of ideal gas behaviour is appropriate, as well as preferable. Finally, the BETS 0.36 experimental temperature data has been successfully validated by means of CFD analysis.

It can therefore be concluded that the research aim has been accomplished through successfully completing each research objective, which is listed in Section 1.4 and mentioned in the previous subchapter. It can also be concluded that STAR-CCM+® is capable of providing an accurate CFD analysis of thermal dispersion in a structured pebble bed.

6.3 Recommendations

The mesh independency study was affected by the presence of large temperature gradients and rapidly oscillating flow fields. This motivates the use of total pressure drop as alternative to radial temperature profiles in subsequent packed bed mesh independency studies. Nevertheless, care should be taken when resolving the turbulence in mesh independency studies with LES since the filter cut-off width is dependent on the volume cell dimensions. It is further recommended to investigate the use of larger Smagorinsky constants in future studies. For efficiency purposes, it is suggested to use the CFL condition as criterion in automatic time step control. Following the validation study, it is proposed to account for the variation in boundary layer thickness, which is associated with the different Reynolds numbers, by correlating the prism layer thickness to the kinematic viscosity. Lastly, it is recommended to use time-averaged results instead instantaneous results when conducting unsteady simulations.

BIBLIOGRAPHY

Achenbach, E. 1995. Heat and flow characteristics of packed beds. *Experimental Thermal and Fluid Science*, 10:17-27.

Askeland, D.R. & Fulay, P.P. 2009. Essentials of materials science and engineering. 2nd ed. Toronto, Cengage Learning.

Bauer, R. & Schlünder, E.U. 1978a. Effective radial thermal conductivity of packings in gas flow. Part I. Convective transport coefficient. *International Chemical Engineering*, 18(2):181-188.

Bauer, R. & Schlünder, E.U. 1978b. Effective radial thermal conductivity of packings in gas flow. Part II. Thermal conductivity of the packing fraction without gas flow. *International Chemical Engineering*, 18(2):189-204.

Carlson, E.C. 1996. Don't gamble with physical properties for simulations. *Chemical Engineering Progress*, 92(10):35-46.

Caulkin, R., Ahmad, A., Fairweather, M., Jia, X. & Williams, R.A. 2007. An investigation of sphere packed shell-side columns using a digital packing algorithm. *Computers and Chemical Engineering*, 31:1715-1724.

Cheng, G.J., Yu, A.B. & Zulli, P. 1999. Evaluation of effective thermal conductivity from the structure of a packed bed. *Chemical Engineering Science*, 54:4199-4209.

Cheng, R., Xing-Tuan, Y. & Yan Fei, S. 2013. Porous structure analysis of the packed beds in a high-temperature reactor pebble bed modules heat transfer test facility. *Chinese Physics Letters*, 30(2):022801.

Chung, T.J. 2002. Computational fluid dynamics. Cambridge: Cambridge University Press.

Davidson, P.A. 2004. Turbulence. Oxford: Oxford University Press.

Delgado, J.M.P.Q. 2006. A critical review of dispersion in packed beds. *Heat Mass Transfer*, 42:279-310.

Demirel, Y., Sharma, R.N. & Al-Ali, H.H. 2000. On the effective heat transfer parameters in a packed bed. *International Journal of Heat and Mass Transfer*, 43:327-332.

Dixon, A.G. & Nijemeisland, M. 2001. CFD as a design tool for fixed-bed reactors. *Industrial & Engineering Chemistry Research*, 40:5246-5254.

Duan, Y., Xu, M., Zhou, X. & Huai, X. 2014. A structured packed-bed reactor designed for exothermic hydrogenation of acetone. *Particuology*, 17:125-130.

Du Toit, C.G., Van Antwerpen, W. & Rousseau, P.G. 2009. Analysis of the porous structure of an annular pebble bed reactor. (*In*: Proceedings of the International Congress on Advances in Nuclear Power Plants 2009 (ICAPP 2009) held in Tokyo, Japan on 10 – 14 May. Paper: 9123).

Du Toit, C.G., Rousseau, P.G. & Kgame, T.L. 2012a. Separate effect tests to determine the thermal dispersion in structured pebble beds using the PBMR HPTU test facility. (*In*: Proceedings of the 6th International Topical Meeting on High Temperature Reactor Technology (HTR-2012) held in Tokyo, Japan on 28 October – 1 November. Paper: HTR2012-6-021).

Du Toit, C.G., Rousseau, P.G., Kgame, T.L. & Preller, A.C.N. 2012b. Experimental and numerical modelling of enhanced thermal diffusion in a structured packed bed. (*In*: De Vahl Davis ed. CHT-12: Proceedings of the 5th International Symposium on Advances in Computational Heat Transfer held in Bath, UK on 1-6 July. Redding: Begell House. [CD-ROM], Paper VV-02.

Du Toit, C.G. & Rousseau, P.G. 2014. Separate effects tests to determine the pressure drop over packed beds in the PBMR HPTU test facility. (*In*: Proceedings of the 7th International Topical Meeting on High Temperature Reactor Technology (HTR 2014) held in Weihai, China on 27 – 31 October. Paper: HTR2014-61107).

Du Toit, C.G., Rousseau, P.G. & Kgame, T.L. 2014. Separate effects tests to determine thermal dispersion in structured pebble beds in the PBMR HPTU test facility. *Nuclear Engineering and Design*, 271:437-443.

Eisfeld, B. & Schnitzlein, K. 2001. The influence of confining walls on the pressure drop in packed beds. *Chemical Engineering Science*, 56:4321:4329.

Eppinger, T., Seidler, K. & Kraume, M. 2011. DEM-CFD simulations of fixed bed reactors with small tube to particle diameter ratios. *Chemical Engineering Journal*, 166:321-331.

Ferziger, J.H. & Perić, M. 2002. Computational methods for fluid dynamics. 3rd ed. Berlin: Springer.

Fogler, H.S. 2014. Elements of chemical reaction engineering. 4th ed. Harlow: Pearson.

Hassan, Y.A. 2008. Large eddy simulation in pebble bed gas cooled core reactors. *Nuclear Engineering and Design*, 238:530-537.

Hlushkou, D. & Tallarek, U. 2006. Transition from creeping via viscous-inertial to turbulent flow in fixed beds. *Journal of Chromatography A*, 1126:70-85.

Holgate, J., Skillen, A., Craft, T. & Revell, A. 2018. A review of embedded large eddy simulation for internal flows. *Archives of Computational Methods in Engineering*: 1-18.

Incropera, F.P., Dewitt, D.P., Bergman, T.L. & Lavine, A.S. 2013. Principles of heat and mass transfer. 7th ed. Singapore: Wiley.

Kang, C. 2010. Pressure drop in a pebble bed reactor. Texas: Texas A&M University. (Thesis – M.Sc.).

Kgame, T.L. 2008. HPTU BETS 0.36 test report. Revision 2. M-Tech Industrial (Pty.) Ltd. (Document number: HPTU002-BETS036).

Kgame, T.L. 2010. Evaluation of the enhanced thermal fluid conductivity for gas flow through structured packed pebble beds. Potchefstroom: NWU. (Dissertation – M.Eng.).

Latifi, M.S., Setayeshi, S., Starace, G. & Fiorentino, M. 2016. A numerical investigation on the influence of porosity on the steady-state and transient thermal-hydraulic behavior of the PBMR. *Journal of Heat Transfer*, 138(10):102003-102003-9.

Li, H., Qiu, S., Zhang, Y., Su, G. & Tian, W. 2012. Thermal hydraulic investigations with different fuel diameters of pebble bed water cooled reactor in CFD simulation. *Annals of Nuclear Energy*, 42:135-147.

Li, L., Yan, X., Yang, J. & Wang, Q. 2017. Numerical investigation on the band-broadening characteristics of an ordered packed bed with novel particles. *Applied Energy*, 185:2168-2180.

Logtenberg, S.A. & Dixon, A.G. 1998. Computational fluid dynamics studies of fixed bed heat transfer. *Chemical Engineering and Processing*, 37:7-21.

Munson, B.R., Young, D.F., Okiishi, T.H. & Huebsch, W.W. 2009. Fundamentals of fluid mechanics. 6th ed. Hoboken, NJ: Wiley.

Nijemeisland, M. & Dixon, A.G. 2004. CFD study of fluid flow and wall heat transfer in a fixed bed of spheres. *American Institute of Chemical Engineers Journal*, 50(5):906-921.

Pozrikidis, C. 2011. Introduction to theoretical and computational fluid dynamics. 2nd ed. New York, NY: Oxford University Press.

Preller, A.C.N. 2011. Numerical modelling of flow through packed beds of uniform spheres. Potchefstroom: NWU. (Dissertation – M.Eng.).

Reyneke, H.J. 2009. Investigation into the velocity distribution through an annular packed bed. Potchefstroom: NWU. (Dissertation – M.Eng.).

Rhodes, M. 2008. Introduction to particle technology. 2nd ed. Chichester: Wiley.

Rousseau, P.G. & Van Staden, M. 2008. Introduction to the PBMR heat transfer test facility. *Nuclear Engineering and Design*, 238:3060-3072.

Sagaut, P. & Deck, S. 2009. Large eddy simulation for aerodynamics: status and perspectives. *Philosophical Transactions of the Royal Society A*, 367:2849-2860.

Schlichting, H. & Gersten, K. 2017. Boundary-layer theory. 9th ed. Berlin: Springer.

Siemens Product Lifecycle Management (PLM) Software Inc. 2017. STAR-CCM+® Documentation. Version 12.02. Plano, TX.

Shams, A., Roelofs, F. & Komen, E.M.J. 2012. Numerical simulations of a nuclear pebble bed configuration: a journey from DNS to RANS. (*In*: Proceedings of the 6th International Topical Meeting on High Temperature Reactor Technology (HTR-2012) held in Tokyo, Japan on 28 October – 1 November. Paper: HTR2012-6-005).

Shams, A., Roelofs, F., Komen, E.M.J. & Baglietto, E. 2014. Large eddy simulation of a randomly stacked nuclear pebble bed. *Computers & Fluids*, 96:302-321.

Theron, W.G.J. 2011. Numerical analysis of the flow distribution within packed columns using an explicit approach. Potchefstroom: NWU. (Dissertation – M.Eng.).

Van Antwerpen, W. 2009. Modelling the effective thermal conductivity in the near-wall region of a packed pebble bed. Potchefstroom: NWU. (Thesis – Ph.D.).

Van der Merwe, W.J.S. 2014. Analysis of flow through cylindrical packed beds with small cylinder diameter to particle diameter ratios. Potchefstroom: NWU. (Dissertation – M.Eng.).

Verein Deutscher Ingenieure. 2010. VDI heat atlas. 2nd ed. Berlin: Springer.

Versteeg, H.K. & Malalasekera, W. 2007. An introduction to computational fluid dynamics. 2nd ed. Harlow: Pearson.

Welty, J.R., Wicks, C.E., Wilson, R.E. & Rorrer, G.L. 2008. Fundamentals of momentum, heat and mass transfer. 5th ed. Hoboken, NJ: Wiley.

Wen, D. & Ding, Y.D. 2006. Heat transfer of gas flow through a packed bed. *Chemical Engineering Science*, 61:3532-3542.

Wilcox, D.C. 2006. Turbulence modelling for CFD. 3rd ed. La Cañada, CA: DCW Industries.

Wu, H., Gui, N., Yang, X., Tu, J. & Jiang, S. 2017. Numerical simulation of heat transfer in packed pebble beds: CFD-DEM coupled with particle thermal radiation. *International Journal of Heat and Mass Transfer*, 2017:393-405.

Wu, Z., Wu, Y., Tang, S., Liu, D., Qui, S., Su, G.H. & Tian, W. 2018. DEM-CFD simulations of helium flow characteristics in randomly packed bed for fusion reactors. *Progress in Nuclear Energy*, 109:29-37.

Yang, J., Wang, Q., Zeng, M. & Nakayama, A. 2010. Computational study of forced convective heat transfer in structured packed beds with spherical and ellipsoidal particles. *Chemical Engineering Science*, 65:726-738.